UILU-ENG 84-3609

Report No. 109

FATIGUE DAMAGE AND SMALL CRACK GROWTH DURING BIAXIAL LOADING

by

Chang-Tsan Hua
Department of Mechanical and Industrial Engineering, UIUC

A Report of the
MATERIALS ENGINEERING - MECHANICAL BEHAVIOR
College of Engineering, University of Illinois at Urbana-Champaign
July 1984

ABSTRACT

The progressive nature of fatigue damage under biaxial loading has been investigated. Experiments were performed on thin-wall tubular specimens of 1045 steel in tension, torsion, and combined tension-torsion loading. Two equivalent strain amplitudes, one in the high cycle fatigue (HCF) region and one in the low cycle fatigue (LCF) region were employed in this study for all loading patterns. The test program included constant amplitude loading and variable amplitude loading. Two types of variable loading patterns, step loading and block loading, were selected.

Different types of crack systems were formed in the HCF and LCF regions. In the HCF region, cracks nucleated on a few planes. Usually one of them grew into a dominant crack and led to failure. This type of cracking is called Typed-S (side) crack system. In the LCF region, equally developed microcracks are observed over the entire gage section. The failure is due to a linking process in which the microcracks join up during the last few cycles of the fatigue life. This type of cracking is called Type-R (ring) crack system.

Two approaches, the damage curve approach and the fracture mechanics approach, were selected to analyze the test results. The two crack systems can be analyzed by the damage curve approach. The results showed that the damage curve for pure tension can be used to evaluate damage behavior under combined tension-torsion within the tested strain ratios. Fatigue lives under variable amplitude loading can be predicted from constant amplitude damage curves if a single type of crack system dominates the fatigue process. During block loading, two competitive

crack systems can be developed in a single specimen. This results in conservative prediction of the fatigue life.

The fracture mechanics approach is only applicable for Type-S crack. The mixed mode small crack growth rate can be correlated with the strain based intensity factor and total energy release rate. The agreement with the long crack data justified the approach.

ACKNOWLEDGMENT

This investigation was supported by NSF grants MEA-81-11282 and MEA-82-10620. Tests were conducted in the Materials Engineering Research Laboratory.

The author wishes to express his sincere gratitude to Dr. D. F. Socie, his advisor, for the valuable advice and encouragement offered him during the preparation of this thesis, and for the general guidance throughout his graduate study.

Thanks are due to Doctoral Candidate J. W. Fash and Dr. D. L. McDowell for their helpful suggestions and assistance. The effort of Mr. J. L. Koch in the testing operation is greatly appreciated. The staff of the Department Publication Office is thanked for their assistance in preparing this thesis.

Best thanks are extended to his wife Jen for her love and encouragement during his graduate study in the University of Illinois.

TABLE OF CONTENTS

NOMENCLATURE

a	crack depth
a_f	reference value to normalize crack depth
B	number of blocks at specific block loading
B_f	number of blocks to failure at specific block loading
C	weighted crack density
C_f	reference value to normalize weighted crack density
c	half surface crack length
D	damage parameter
E	Young's modulus
$E(k)$	complete elliptic integral of the second kind
$F(k)$	complete elliptic integral of the first kind
G	shear modulus
G_t	total energy release rate
K_i	mode I, II, or III stress intensity factor (i=I, II, or III)
$K_{eq}(\sigma)$	equivalent stress intensity factor
$K_{eq}(\varepsilon)$	equivalent strain based intensity factor
k	aspect ratio (= a/c)
L	surface crack length (= 2c)
L_f	reference value to normalize surface crack length
ℓ	half surface crack length or crack depth
N, N_f	number of cycles to failure at specific loading level
n	number of cycles at specific loading level
n'	number of cycles for initiation phase
R_ε	strain ratio in strain controlled test ($\overline{\varepsilon}_{min}/\overline{\varepsilon}_{max}$)
r	number of cracks per unit area
t	specimen thickness
u	step function
x	cycle ratio (= n/N)
x'	cycle ratio (= n'/N)
Y_i	mode I, II, or III geometry factor (i=1, 2, or 3)
Σ_{exp}	experimental sum of cycle ratios
Σ_{pre}	predicted sum of cycle ratios
λ	strain ratio (shear strain/axial strain)

ξ	relative cycle ratio within a block
β_i	cycle ratio at specific loading level
$\overline{\Delta\varepsilon_i}$	Von Mises type equivalent strain range [$= (\Delta\varepsilon^2+\Delta\gamma^2/3)^{1/2}$]
σ	nominal tensile stress normal to the crack plane
τ	nominal shear stress along the crack plane
ψ	parametric angle of the ellipse
ν	Poisson ratio
ε_t	total tensile strain amplitude normal to the maximum shear strain plane
γ_t	total maximum shear strain amplitude
θ	directional angle of surface crack

1. INTRODUCTION

1.1 Description of the Problem

One of the unresolved problems in fatigue under variable amplitude loading appears to be fatigue damage. Any attempt to evaluate cumulative damage in terms of basic fatigue behavior is hampered by a lack of detailed understanding of mechanisms in simple fatigue tests. A number of analytic approaches have been developed and are illustrated in Fig. 1. A review paper by Kaechele [1] pointed out that in order to use basic fatigue data in designing structures to withstand loading cycles of many different levels, it is necessary to determine (1) how damage progresses at one loading level and (2) how to properly add together the damage produced by each loading cycle when different cycles are mixed together.

At least three characteristics are involved in the fatigue damage process; they are:

(1) Double phases in fatigue life, i.e. an initiation phase consisting of crack nucleation and microcrack growth and a propagation phase of macroscopic crack growth [2,3].

(2) Nonlinearity of damage accumulation. In other words, damage is stress or strain amplitude dependent [4,5].

(3) Interaction effect between different stress or strain amplitudes [6,7].

Most of the damage theories do not account for the above three characteristics simultaneously. Understanding the interaction effect is the key to solving fatigue damage problems. In general, the interaction

effects under variable amplitude loading could be related to cracking, residual stress, crack closure, crack blunting and cyclic strain-hardening. In the case of a sharply notched member, the crack growth behavior will be strongly related to plastic deformation around the crack tip. For a small crack (between 20 microns and 1 mm) in a smooth specimen, the bulk plastic strains are important. For small crack problem the interaction effect by different crack systems, if present, will be crucial to understanding fatigue damage problems.

One of the early cumulative damage studies by Marco and Starkey [5] divided the fatigue life into the regions. They tested an aluminum alloy and 4340 steel with the results shown in Fig. 2. Two types of crack systems were classified on the basis of crack development and the fracture surface appearance. In the high cycle fatigue (HCF) region, a crack usually started at only one point on the side of the specimen and propagated across the specimen to final failure. The failure crack grew into the specimen from one side and was called Type-S (side) failure. In the low cycle fatigue (LCF) region, microcracks started at a large number of points around the circumference and propagated independently and uniformly toward the center where final rupture occurred. The appearance of fatigue surface was a thin ring and was called Type-R (ring) failure. The transition from Type-R to Type-S crack systems occurred between 10^4 and 10^5 cycles for 4340 steel. Wood [8] studied copper and brass and also observed the existence of two different damage regions in the S-N curve. The high stress damage region is associated with massive dislocation movements and a "static" type of fracture. The low stress damage region is characterized by fine slip concentrated on a

few planes. Damage caused in these two regions do not differ in degree, but differ in kind. Under high stress amplitude loading, the failure crack results from a linking process; a process similar to the tearing of perforated material [9]. Later Porter and Levy [10] and Benham and Ford [11] also confirmed two different fatigue mechanisms. Freudenthal [12] suggested that the mechanism of cumulative damage under a combination of high and low strain amplitudes is quite different from the damage mechanisms in either the high strain or the low strain alone and more damaging than would be the sum of the two.

In the last twenty years, few papers reported the different crack systems. Since Paris and Erdogen [13] proposed propagation law for a single dominant crack (Type-S crack) and Elber [14] suggested the importance of crack closure behavior for the long Type-S crack, the fracture mechanics approach for propagation has been employed by many researchers [15]. Many engineering components involve thermal and/or mechanical cycling in LCF region. Before applying fracture mechanics, a serious limitation should be considered. Under complex loading is stressed body going to develop a Type-S crack? If the answer is uncertain, then the applicability of this approach in design process becomes questionable. Fracture mechanics cannot deal with the continuum damage nature of the Type-R crack system.

In many practical situations the loading conditions of structural members and machine components are complex. For example, in the automotive industry, parts such as crank shafts are subjected to simultaneous bending and torsion; in the power plant industry, pipes are subjected to biaxial or triaxial stresses. Life prediction of parts

subjected to multiaxial fatigue is of prime importance for reliability and safety. Many studies have been conducted with variable amplitude cyclic loading. Most of these investigations have resulted in theories to predict fatigue life under uniaxial variable loading. However, much of the damage occurs in biaxial or triaxial stress/strain states. Few papers have studied fatigue damage under multiaxial stress states. Blatherwick and Viste [16] investigated two-level step loading under biaxial stress condition. McDiarmid [17] studied the effect of principal stress ratio under biaxial loading.

1.2 Approaches to the Problem

For a Type-S crack under biaxial stress/strain state, fracture mechanics may be used to analyze crack growth behavior. For the problem of different crack systems involved, other approaches must be considered (see Fig. 1). In this study, the damage curve approach is employed to analyze two different crack systems.

The damage curve approach is developed in Chapter 3. Half of the chapter is given to describe the fatigue damage behavior under constant amplitude loading. Two different crack systems are confirmed and the process of fatigue damage is described by phenomenological observations. The damage curve approach is then used to generate damage curves for the two crack systems. The fatigue damage behavior under different loading modes is compared. Recent damage theories are examined and compared with experimental observations. The later half of the chapter is given to describe fatigue damage under variable loading. Fatigue damage caused by the interaction of two different

crack systems is examined in detail. The fatigue lives of variable loading test are predicted from constant amplitude damage curves.

The Type-S crack growth under biaxial loading is analyzed by the fracture mechanics approach in Chapter 4. The applicability of the approach for mixed mode small crack growth is investigated. Results for small cracks are compared with long crack data.

2. EXPERIMENTAL PROGRAM

2.1 Material and Specimens

Hot-rolled 1045 steel (63.5 mm diameter) in the normalized condition was used in this investigation. The investigation is part of Society of Automotive Engineers Fatigue Design and Evaluations Committee biaxial test program. Related studies can be found in Refs. [18,19]. The unetched microstructure is shown in Fig. 3. Note the sulfide inclusions in the direction of rolling. They are approximately 0.1 mm long. Mechanical properties are given in Table 1. Tests were conducted using thin-wall tubular specimen shown in Fig. 4. Finite element analysis showed that the axial strain gradient along the gage length was less than 2 percent. The torsional strain gradient along the surface was nearly zero and the torsional gradient between the inner and outer surfaces was 15 percent.

2.2 Test Procedure

Standard machine collets are used to grip the ends of the specimens. An internal extensometer, shown in Fig. 5, was designed so that the outside surface of the specimen could be easily replicated with acetyl cellulose film to monitor crack formation and growth. Axial displacements were measured and controlled with an LVDT located on the centerline of the specimen and rotations with an RVDT. Coupling between the two measurements was less than 1 percent. Test were conducted on an MTS Model 809 tension-torsion machine that was modified to increase the torsional stiffness. An MTS Model 463 processor/interface was used for computer control and data reduction of the tests.

Specimens were polished to eliminate scratches that might be interpreted as small cracks. Final polishing was done with 0.5 micron alumina. Standard metallographic acetyl cellulose film was used to record the surface of the specimens during fatigue. Methyl acetone was applied to the surface with a syringe and the film placed around the gage length of the specimen. Considerable improvement in the quality of the replica can be obtained by using high grade methyl acetate rather than distilled acetone. After removing the replica from the specimen, it was placed between glass slides. Several techniques were attempted to observe the details of the replicas including SEM observation incorporated with evaporation or sputtering of conductive films. The easiest and most reliable method for observation of the replicas is using an optical microscope and illuminating through the replica.

2.3 Constant Amplitude Loading

Four Von Mises equivalent strain amplitudes were selected for these tests; 1.0, 0.43, 0.22, and 0.15 percent. Failure was defined as 10 percent axial load drop in all of the tests except pure torsion loading. In the pure torsion tests, 10 percent torsional load drop was used. Five strain ratios (λ = shear strain/axial strain) were employed in this study. The case of $\lambda = 0$ is pure tension, and $\lambda = \infty$ is pure torsion. Ratios of 0.5, 1 and 2 are combined tension-torsion loading. All tests were conducted under completely reversed strain-controlled conditions at room temperature.

2.4 Variable Loading

Two types of variable loadings were selected to study the interaction of two different crack systems. The loading patterns are shown in Fig. 6.

2.4.1 Step Loading

Von Mises type equivalent strain amplitude of 1.0 percent and 0.22 percent were selected for the two-level step loading. The first is in the LCF region and the other is in the HCF region. Three different strain ratios, λ = 0, 1, and ∞ were employed in this series of tests. High-low and low-high loading sequences were included in the test program to examine sequence effect. The test was run approximately for half of the constant amplitude life at the first level then changed to second level until failure occurred. To isolate the mean stress effect, the second level of low strain amplitude was run with mean strain so that the mean stress was zero.

2.4.2 Block Loading

Five loading parameters are needed to specify a two-level block loading,. (1) For loading levels, values of equivalent strain amplitudes of 1.0 and 0.22 percent were employed. (2) For loading mode, one strain ratio λ = 1 was tested. (3) High-low and low-high loading sequences were included to examine the effect of the first sub-block. (4) Number of cycles within a block were selected so that each block would contribute 10 percent of the fatigue damage as determined by Miner's linear damage rule [20]. (5) The relative cycle ratio is

defined as the low strain cycle ratio divided by the high strain cycle ratio in the loading block. Five relative cycle ratios were tested for each loading sequence: 0.05, 1, 1.8, 4, and 19. For example, if the relative cycle ratio equals 1, the high and low strain amplitude cycles contribute equally to the damage when the damage is accessed by Miner's linear rule.

3. DAMAGE CURVE APPROACH

3.1 Introduction

Since the linear damage rule [20] was proposed, a number of investigators have proposed theories to account for the nonlinearity of damage accumulation. In some of the proposed theories, an attempt has been made to relate concept of damage to the life of a material subjected to a complex stress loading.

3.1.1 Early Studies

Richard and Newmark [4] introduce the concept of nonlinear damage curves as Fig. 7 shown. Various curves on a damage-cycle ratio diagram were assumed to represent the process of failure at different loading levels. The functional relation is given by:

$$D = x^p \tag{3.1}$$

where

$x = n/N$

and

p = a constant which depends on loading amplitude.

Note the special case of $p = 1$ corresponds to Miner's linear damage rule. Later Marco and Starkey [5] deduced the value of p should be larger than 1 based on results of their sequential-load tests. Hence the damage curve should be concave and upward. Grover [2] suggested the double linear damage rule in which Miner's rule was applied to initiation and propagation phases separately.

3.1.2 Recent Studies

Four damage models that have been proposed within the last ten years will be evaluated and are briefly described below.

3.1.2.1 Chaboche Model

This model is based on the physical idea that a crack is preceded by a progressive internal deterioration of the material. Under a completely reversed strain-controlled test, an effective stress concept [21] is used to measure the decrease in tensile load-carrying capability. Chaboche [22] used this concept and proposed the following form for fatigue damage:

$$D = 1 - [1 - x^{1/1-\alpha}]^{1/1+\beta} \qquad (3.2)$$

where α is an exponent that depends on the applied loading amplitude and β is a material constant.

3.1.2.2 Lemaitre-Plumtree Model

Similar to the form of Chaboche, this model [23] includes only one material parameter which is dependent on the applied loading amplitude. The differential form of the damage equation was that of Kachanov's work [24] and modified to take into account the nonlinear damage accumulation. Fatigue damage is given by:

$$D = 1 - (1 - x)^{1/b+1} \qquad (3.3)$$

where b is the material parameter that depends on the loading amplitude and describes the rate of damage accumulation.

3.1.2.3 Manson model

Manson and his associates first employed the double linear damage rule in 1967 [25]. Later Manson and Halford [26] modified the method to obtain a governing equation for the rule. The derived equation is based on the damage curve concept in which a crack growth model is involved. The form of the model is given by:

$$D = x^{fN^g} \tag{3.4}$$

where f and g are material constants which are independent of the applied loading amplitude.

3.1.2.4 Fong Model

A conceptual definition of fatigue damage was proposed by Fong in 1982 [27]. Damage rate was assumed to vary linearly with damage itself. By integration, the final form of the damage equation is expressed as

$$D = \frac{\exp(hx) - 1}{\exp(h) - 1} \tag{3.5}$$

where h is a material constant which is dependent of the applied loading amplitude.

3.2 Test Results and Discussion

3.2.1 Constant Loading

The summary of constant loading results is shown in Table 2 and Fig. 8. The transition from Type-R to Type-S crack systems occurred between 10^4 and 10^5 cycles. One of the low strain levels, 0.22 percent, was selected to study damage growth behavior of Type-S crack. One of the high strain levels, 1.0 percent, was selected to study damage growth behavior of Type-R crack. Then the damage curves for these two strain amplitudes are compared.

3.2.1.1 Type-S crack system

Test results. Figure 9 shows the cracking behavior of pure tension ($\lambda = 0$) in the HCF region. At early stage of the life, microcrack grew to a size of 10-20 μm. In the middle of its life, the crack grew to 0.1 mm in length. At the end of the life, a 2-3 mm visible crack developed. The crack tip grows alternately between two maximum shear planes even near final failure. Forsyth [28] suggested that a two stage classification of crack growth can be made. Stage I involves the growth of crack on planes of maximum shear stress. Stage II involves the growth of crack in a direction normal to the maximum tensile stress. He observed that low stresses result in slow growth that favors Stage I behavior.

Figure 10 shows combined tension-torsion results for $\lambda = 1$. The results are similar to those of pure tension. At early stages of the life, cracks grew along one of the maximum shear strain amplitude planes

where d, e and p are material constants, D' is the damage caused by the crack nucleation and microcrack growth phase, n' is the number of cycles for this phase, x=n/N, x'=n'/N, u(o), u(x') are the step function.

The model proposed by Miller and Ibrahim [30] predicts a similar life fraction for the transition from initiation to propagation as the experimental results in this paper. Transition crack lengths from initiation to propagation are an order of magnitude smaller than those found in this investigation. In both cases, the material is 0.4% carbon steel. Miller and Ibrahim tests were performed on solid bars in torsion only compared to the three loading modes used here. The smaller initiation size for torsion is consistent with the observation of this work. It appears that the normal strain on the plane of maximum shear strain influences the transition from initiation to propagation.

Damage curves under different loading modes. Most of the research in multiaxial fatigue of ductile materials has shown that cracks initiate and propagate on or near the planes of maximum shear. For practical design purposes, a unique damage curve that represents all loading modes is desirable. In this case, surface crack length cannot be used as a damage parameter. The test results show that about ten times the surface crack length was developed in pure torsion than in other loading modes. Miller [31] suggests that the cracks propagated into the specimen will usually be the most dangerous. Crack depth could be considered a better damage parameter when damage curves of different loading modes are involved.

A number of specimens were sectioned and polished to determine aspect ratio between surface crack length and crack depth. Figures 17,

18, and 19 show three of the sectioned samples with different loading modes. Table 3 shows the summary of measured values of the aspect ratio. Three samples were sectioned for each pure torsion and combined tension-torsion ($\lambda = 1$) loading. Only one sample in pure tension was sectioned to compare the results with other references [32].

Surface crack lengths were converted into crack depth using the aspect ratio shown in Table 3. The aspect ratios were assumed constant throughout the fatigue life. Results in terms of crack depth are shown in Fig. 20. Damage curves of tension and combined tension-torsion are again merged into one line similar to Fig. 12. The damage curve for torsion shows different damage patterns even when expressed in terms of crack depth. Possible reasons for such deviation are (1) anisotropy of the material, i.e. inclusions on one of the maximum shear planes and (2) lack of a normal stress acting on the maximum shear planes which can change the fatigue process [33].

3.2.1.2 Type-R Crack System

Test Results. Figure 21 shows the failure process of a Type-R crack system under pure tension. Microcracks developed over the entire gage section during the fatigue life, but until 1100 cycles no visible crack could be seen. At cycle 1132, the microcracks begin to join up at potential crack front. After three cycles the crack front has been formed. The specimen failed at cycle 1137. The linking process only occurred during the last few cycles. The failure crack is not a useful measure of the damage growth for this crack system. The change of crack density during fatigue process should be considered.

Figures 22 to 24 show crack growth that represents different loading modes. Damage development was the same in all three cases. The photographs for each loading mode present the early stage, the middle stage, and the final stage of the life. Damage patterns were established at very early stages of the life.

Two common features were observed in all three loading modes. First, the number of microcracks increased with the number of loading cycles. Second, the surface length of microcracks which appeared in the early stages remained nearly constant during the fatigue life. For example, the development of the same crack at various stages in the life is indicated by the arrows. Darkness and clarity of the microcracks substantially increased with progress of fatigue cycles. These observations indicate that the crack opening and hence crack depth have increased. Cracks initiated on the surface and propagate into the surface as reported by Marco and Starkey [5]. Also, crack orientations are developed equally on both planes of maximum shear. These multi-microcracks are nearly uniformly distributed over the entire gage length. In torsion, both uniform distribution of microcracks and long cracks along the inclusion were observed.

Damage measurement for Type-R crack system. Neither a single surface crack length nor a single crack depth can be applied as damage parameters for the LCF results. Crack density [34] was used as a measure of damage for these tests. The number of cracks per unit area alone is not a suitable damage parameter, because a number of microcracks form early in the life and then grow into the depth. This

will result in an unrealistic damage curve such that most of the fatigue damage seems to occur during the early stages of the life and growth into the specimen is not taken into account. Once a crack appears, it is assumed to contribute to damage continuously until final failure. This behavior can be accommodated by using a weighted crack density. The method taken to measure damage was as follows:

(1) The cracks were examined from a photo near final failure and the number of cracks per unit area were identified and counted to establish the final crack density.

(2) The number of cracks at each replicating interval could be identified by tracing backward from the replicas taken at successively earlier periods in the life. Depending on the fraction of the life when they first appear, the cracks are given weighting factors in terms of the cycle ratio. Since cracks forming late in the life should not be as damaging as cracks that form earlier.

(3) The following relationship was employed to determine the weighted crack density

$$C_i = \sum_{k=0}^{i-1} \frac{n_i - n_k}{N_f} (r_{k+1} - r_k) \qquad (3.7)$$

where i = positive integer

n_i = current cycle number

n_k = kth previous cycle number; $n_0 = 0$

N_f = cycle to failure

r_k = number of cracks per unit area observed at

$$n_k;\ r_o = 0$$

C_i = damage accumulated up to n_i

In Eq. (3.7), $(n_i - n_k/N_f)$ is the weighting factor. The reference value C_f is the weighted crack density at failure.

Comparison of damage models with experimental results. A few cycles of high strain amplitude can eliminate the entire initiation period of fatigue life. The damage models in Section 3.1.2 were also employed to analyze one of the LCF results. Figure 25 shows the result in which most of the models fit all the data points. Unlike the HCF region, a single damage parameter can be used to describe the growth over the entire life range.

Damage curve under different loading modes. The comparison of damage curves under different loading modes are shown in Fig. 26. Again, damage curves for pure tension and combined loading are merged into a single line. The damage curve for pure torsion deviates from the above two loading modes by a much smaller amount than in the HCF region (compare with Fig. 20). This deviation could be within the data scatter or related to the dominant crack that forms along the inclusions.

3.2.1.3 Comparison of Damage Curves Under Different Crack Systems

One of the damage curves ($\lambda = 1$) in Fig. 12 and one of the damage curves ($\lambda = 1$) in Fig. 26 were replotted in Fig. 27 for comparison under combined tension-torsion loading. The damage curve in Fig. 13 and one of the damage curves ($\lambda = \infty$) in Fig. 26 were replotted in Fig. 28 for comparison under torsion loading.

Damage curves obtained for combined loading show the same behavior that is commonly observed in tensile loading. Crack observations also suggest that interaction effects will be important in accessing fatigue damage under variable amplitude loading. the damage curves and physical observations suggest that interaction effects in torsional loading will be smaller than other two loading modes. The damage curves in Figs. 27 and 28 were employed to predict the fatigue life of variable amplitude loading.

3.2.2 Variable Loading

Figure 29 shows one set of hysteresis loops for variable loading for $\lambda = 1$. After the loading amplitude was changed from a high strain level to a low strain level, a small compressive mean stress was formed. The compressive mean stress relaxed to zero during the following cycles. No significant mean stress effect was involved in the results for variable loading.

3.2.2.1 Step Loading

Test results. The results of the step loading tests are summarized in Table 4. The constant amplitude damage curves in Figs. 27 and 28 were used to predict the remaining fatigue life for the second level. The results of Lo-Hi sequence are shown in Figs. 30, 31, and 32. The results of these three tests followed similar crack growth behavior and developed Type-S failure crack. One of the tests is described in detail. Figure 31 shows the results for $\lambda = 1$. The test was cycled for half of the fatigue life, 56,000 cycles, at a low strain

level before changing to a high strain level and cycling until failure occurred. A Type-S crack was developed during the low strain level cycling. The crack developed from about 20 micron and grew to 0.1 mm at the end of low strain level. The size of this crack is greater than the crack length in initiation phase (below 80 micron, refer to Fig. 16). After changing to the high strain level, this single dominant crack continuously grew until Type-S failure occurred. This indicates that if the application of the initial cycles results in a crack length greater than the initiation phase crack size, then this crack will continuously grow to failure even if a high strain level is applied. No change to Type-R failure will occur. As an example, the knife edges of an extensometer can sometimes cause a small notch whose length is over the initiation phase and the specimen always fails with a Type-S crack. Results of the Hi-Lo sequence are shown in Figs. 33, 34, and 35. The results of these three tests followed similar crack growth behavior and developed Type-R failure crack. The Type-R crack system developed continuously even when the amplitude was changed to a low strain level. Similar results for step loading have also been reported by Riemann and Wood [35].

Damage development and life prediction. The prediction of damage growth behavior under step loading is shown in Figs. 36 through 41. The two curves with solid and dashed lines are damage curves from constant loading (see Figs. 27 and 28). The predicted loading path is indicated by the solid line. The experimental results are plotted for the two loading levels. The first level was plotted from the origin of

zero cycles and damage. The second level was plotted from a reference damage and cycle ratio of 1.0. The comparison shows that the crack growth behavior of step loading can be reasonably described by damage curves of constant loading. Some deviations occur because of the scatter in fatigue life.

Predicted lives based on constant amplitude damage curves are compared with experimental results and shown in Fig. 42. The sum of cycle ratio is smaller than one and about 0.7 to 0.8 for the Hi-Lo sequence and is larger than one and about 1.1 to 1.3 for the Lo-Hi sequence. Results are consistent with the studies of step loading on smooth axial specimens [36]. Deviation from actual lives was only about 10 percent and can be interpreted by the scatter in fatigue life for this type of specimen. For the Hi-Lo sequence, all of the specimens failed with Type-R crack systems. For the Lo-Hi sequence, all of the specimens failed with a Type-S crack system. Predictions for pure torsion are better than other two loading modes. Damage curves for torsion show less of an interaction effect between the two different strain levels.

3.2.2.2 Block Loading

Prediction model. To predict the fatigue life for block loading, a mathematical model is employed to simulate block loading tests. The experimental data points for constant amplitude damage curves shown in Fig. 27 are curve fit with the double power function (Eq. 3.6). For the constant low strain amplitude damage curve, two functions are needed for the initiation and propagation phases. For the

constant high strain damage curves, a single power function can fit all of the data points because of the negligible initiation phase. For the case in Fig. 27, the following results are obtained.

For low strain level: $D = 0.053x^{0.44}(u(0) - u(0.6)) + x^{6.1}(u(0.6))$

For high strain level: $D = x^{1.9}$

A computer program was generated to simulate block loading and predict fatigue life. Figure 43 demonstrates the process of simulation. The only assumption involved in this prediction scheme was that damage remains constant during changing the load levels. The loading path alternated between these two loading levels until boundary condition (1,1) was satisfied.

Test results. The results of the block loading are summarized in Table 5. Cracking patterns from one of the Lo-Hi sequence block loading tests is shown in Fig. 44. The relative cycle ratio is equal to 19 which approaches constant amplitude low strain cycles. The cycle number at failure is 8-2-7 for this specimen; 8 is the number of blocks, 2 is the second level, and 7 is the number of cycles for this level. The specimen failed from a Type-S crack and the crack growth behavior was similar to constant low strain loading except that microcracks appeared around the failure crack. For the same relative cycle ratio with Hi-Lo sequence, the results are shown in Fig. 45 and crack growth behavior was nearly identical with the one shown in Fig.

44. The fatigue life of this specimen was about nine blocks. Results for relative cycle ratio equal to 1 for the Hi-Lo sequence is shown in Fig. 46. A Type-R crack system developed into a failure crack. The failure occurred at block 7. Results for the same relative cycle ratio but with a reversed loading sequence is shown in Fig. 47. The crack growth behavior seems similar to the one in Fig. 46, but failure occurs at over ten blocks. Thus the fatigue life (sum of cycle ratios) for this specimen is greater than one.

Damage development and life prediction. Figures 48 to 51 show predicted damage curves compared with experimental results. Block ratio was used instead of cycle ratio where B_f is defined as the actual block number at failure. In Fig. 48 the prediction curve is within 10 percent of the experiments. For the reverse loading sequence where the initial sub-block starts with high amplitude cycles, Fig. 49, the prediction curve is very consistent with the experimental results. For the data in Fig. 50, the relative cycle is equal to 1 and a Type-R crack system was developed. The predicted curve is in good agreement with the test results. However, for the Lo-Hi sequence with the same relative cycle ratio of 1 in Fig. 51, the predicted life was almost 30 percent shorter than actual life. Such deviation also occurred in a few other tests.

All test results for the Hi-Lo sequence are plotted in Fig. 52. The left end of the abscissa is approaching constant amplitude high strain loading, thus the life will approach to one. Similarly, the right end of the abscissa is approaching constant low strain amplitude

loading for which the life also approaches one. The scatter in the fatigue life during constant amplitude loading is shown by the bars in the figure. The predicted lives were in agreement with experimental results except for one of the data points in this sequence. The deviation is about 26 percent above the predicted value. For the Lo-Hi sequence, as shown in Fig. 53, the prediction are only good at the two ends of the relative cycle ratios. All three central data points are above the prediction curve by about 30 to 40 percent. Such deviations occurred in the particular region of relative cycle ratios of 1 to 4. The occurrence of this systematic deviation can be explained by investigating the crack growth behavior in these specimens.

The effect of dual crack systems. The cracking behavior of one of these specimens is shown in Fig. 54. The failure crack developed by a Type-R crack system and is shown on the top two photographs. The unique behavior of this type of crack system is a joining up process which occurs so late in the life that no visible crack can be seen in the previous block. In the same specimen, a few Type-S cracks were also detected. The longest one is shown on the bottom two photographs. This size of crack (about 0.6 mm) would be found at approximately 85 percent of the life during constant amplitude low strain loading. The crack growth of one of the Type-S cracks in this specimen is shown in Fig. 55. In Fig. 56, the damage development for the longest Type-S crack in this specimen is compared with the damage curves in Fig. 51. These two crack systems have similar damage rate during the most of the fatigue process. The existence of two competitive crack systems in a single specimen is responsible for the systematic deviations.

To further understand this phenomenon, the ordinate is plotted with the difference between experimental life and predicted life as Figs. 57 and 58 show. This quantity is related to the effect of dual crack systems. At the two ends, the prediction agreed well with the experimental results. On the left end, the region is dominated by the Type-R crack system. On the right end, the region is dominated by the Type-S crack system. Between these two regions is the competitive region for two crack systems. In this region, the actual life is longer than predicted life up to 40 percent.

As far as LCF involved, this kind of the curve for particular block loading will be useful for design purposes. First, Type-R crack dominant region should be avoided. The failure by Type-R crack is extremely undesirable. By its unique failure process, the crack growth is almost impossible to detect by nondestructive method. Second, the designer should be aware of the fact that the application of fracture mechanics is only suitable for Type-S crack dominant region.

3.2.2.3 General Discussion

Sequence Effect. The sequence effect is noticeable in the results of step loading and in some of the results of block loading. Consider the cases of specimens 4561 and 4564 (see Table 5), both have same relative cycle ratio but with reversed sequence order. Thus, the only difference between these two cases is the first sub-block which determined the pattern of crack system developed. For the case of 4564, the high level was run first and the 70 cycles of high strain amplitude firmly established the Type-R crack system in the specimen.

The following cycles (either high level or low level) continuously produced damage for this crack system until failure. The cracked surface of this specimen was examined carefully and no significant Type-S cracks could be found. The prediction for this case agreed well with the experimental results. For the case of 4561, as discussed in Figs. 54 to 56, two competitive crack systems were developed and the predicted life was shorter than the actual life. Conceivably, the first sub-block of low strain amplitude (5,600 cycles) initiated a few Type-S cracks which continuously grew and competed with the Type-R crack system during the whole fatigue process. Thus, the sequence effect is important when the number of cycles for a specific level is enough to establish its own crack system. However, the sequence effect will decrease by decreasing the damage per block. Such situation can be understood by examining the cases of 4560 and 4562 in Table 5. The seven cycles of high strain amplitude are not enough to set up its own crack system. Consequently, both cases are developed into Type-S failure with similar crack growth behavior (see Figs. 44 and 45).

Sum of Cycle Ratios. Although most of the engineers and researchers realize the limitations of Miner's rule, the rule is still extensively employed in engineering applications. The reason for its long standing is not only because of its simplicity. Jacoby [37] in a survey of 400 values for sum of cycle ratios $\Sigma(n/N)$, including many types of material, structures, types of tests, and types of stressing, shows that the density distribution histogram is centered on the value $\Sigma(n/N) = 1$. The reason for this tendency is more clear from the

results of this study. Even the block tests in this study only with two levels, the experimental results tended to flatten out the prediction curve to the value of 1 (refer to Figs. 52 and 53). Re-examining Table 5 reveals that most of the values are close to 1 and average value of the tests is 0.94. Undoubtedly the study of the interaction of different crack systems holds one of the keys to understanding fatigue damage problems in complex loading histories that do not involve repeating blocks.

3.3 Conclusions

(1) Different types of crack systems were formed in the HCF and LCF regions under constant amplitude loading. A single dominant crack leads to failure in the HCF region. Equally developed microcracks are observed over the entire gage section in the LCF region. The failure of latter crack system is due to a linking process in which the microcracks join up during the last few cycles of the fatigue life.

(2) In the range of biaxial strain ratio tested, damage processes in pure tension and combined tension-torsion under constant amplitude loading are almost identical. The damage curve for pure tension can be used to evaluate damage behavior under combined tension-torsion with same equivalent strain amplitudes.

(3) Fatigue damage accumulates nonlinearly with applied cycles. Both initiation and propagation phases should be considered in

modeling damage curves even for single level loading. A single damage model could not be used to correlate both initiation and propagation phases of the life in the HCF region under constant amplitude loading.

(4) Similar behavior is observed in pure torsion for both HCF and LCF under constant amplitude loading. A single damage parameter can be used because the initiation phase was negligible in both regions for the strain amplitudes considered in this investigation.

(5) Fatigue lives under variable amplitude loading can be predicted from constant amplitude damage curves if a single type of crack system dominates the fatigue process.

(6) Two competitive crack systems can be developed in a single specimen during block loading. This results in conservative prediction of fatigue life.

4. FRACTURE MECHANICS APPROACH

4.1 Introduction

Three elements of fracture mechanics must be considered when the growth of Type-S cracks in this study are analyzed. These are crack shape, stress intensity factor (SIF) and the growth of small cracks.

Part-through cracks are among the most common flaws in many practical structures. Many researchers experimentally examined the crack shape during fatigue. Iida, et al [38] investigated the crack shape under tension and bending. Sommer, et al [39] studied part-through cracks in thick-walled plates and tubes. The shape of a part-through crack has been successfully modeled as semi-elliptical shape by many researchers [32]. Recent experimental results [40] for Inconel 718 with same specimen configuration used for this investigation has shown that the shape of the small part-through crack is prevalently semi-elliptical shape. Good solutions can be expected with the assumption of a semi-elliptical shape.

Stress intensity factor has been extensively used for the crack propagation under mode I loading. Few criteria have been proposed for the propagation of cracks during mixed mode loading. Most of them originate from the solutions of static fracture. Griffith's energy release rate has been long recognized to be a driving force for crack propagation. Erdogen and Sih [41] proposed the maximum principal stress criterion to predict possible direction of the crack extension. Later Sih [42] also proposed strain energy density criterion for the same purpose. Until now the latter two criteria has been applied to plane loading only. Tanaka [43] suggested a propagation law based on

dislocation models due to Weertman [44] and Lardner [45]. Although a tearing mode SIF was included in Tanaka's paper, only opening mode and sliding mode SIFs were employed in his analysis for the experiments of in-plane loading. Miller [46] suggested that a two-parameter description for fatigue fracture under complex stress. The two parameters are the bulk maximum shear stress and the normal stress on the plane of maximum shear.

Anomalous behavior of small crack growth was first shown by Pearson [47]. A complete review will not be given here since it is the subject of considerable research for mode I loading. The difference between small cracks and long cracks can be summarized as follows. First, the continuum mechanics concept is no longer applicable when the crack size is only few grain sizes. Second, Irwin [48] has shown that the SIF can sufficiently accurately describe the crack tip stress-strain state only if the plastic zone size is small compared to the intensified stress field. Third, the effect of crack closure is likely different in small crack growth [49,50]. Based on the above considerations, linear elastic fracture mechanics is invalid to describe the small crack growth behavior. Elastic-plastic fracture mechanics is necessary for this case.

This chapter presents an elastic-plastic fracture mechanics solution for small crack growth under biaxial fatigue loading. Theoretical development for the SIF is treated briefly. Strain based intensity factors and the total energy release rate are employed. The maximum shear strain and the normal strain on the plane of maximum shear strain were used to calculate the strain based intensity factors. With

this background, the experimental data are generated and the results discussed. The discussion focuses on the aspects of applicability of energy release rate criterion and strain based intensity factor for different loading modes. These small crack results are then compared with long crack data to examine the validity of the approach in this study.

4.2 Theoretical Formulation

Note that crack growth into the specimen thickness was assumed to grow perpendicular to the surface.

Before beginning with the formulation of stress intensity factors, several assumptions need to be examined. Consider a small stressed element containing a part-through crack cut from the thin-wall tubular specimen as the top of Fig. 59 shows. First, plane stress condition is assumed for the stress state of a thin wall tube. The development of the crack is assumed self-similar and semi-elliptical shape. The aspect ratio is assumed to remain constant. Since the surface crack length of 1 mm is less than 1 percent of circumferential length and the crack region is within 20 percent of thickness, the curvature effect and back face correction are negligible. Variation in shear stress due to torsional loading is only 1 percent from the mean value over the crack surface and a uniform distribution of shear stress is assumed in the region.

Consider a flat elliptical crack in the body with major and minor semiaxes c and a shown in the bottom of Fig. 59 with the thickness of the plate given as t. Irwin [51] first derived an expression for an embedded elliptical crack under uniform tension on the basis of the stress field around an ellipsoidal cavity derived by Green and Sneddon [52]. The results of Irwin's analysis is given by:

$$K_I = \frac{\sigma(\pi a)^{1/2}}{E(k)} \Psi\ (k,\psi) \qquad (4.1)$$

where

$k = a/c$

$\Psi(k,\psi) = (\sin^2\psi + k^2\cos^2\psi)^{1/4}$

$E(k) = \int_0^{\pi/2} (1-k^*\sin^2\psi)^{1/2} d\psi$

$k^* = 1-k^2$

Later Kassir and Sih [53] also obtained SIF solutions for the case of uniform shear applied to the surface of an infinite solid containing an embedded elliptical crack. If the line of action of applied shear is directed along the major axis of the ellipse, the results are given by

$$K_{II} = \frac{\tau(\pi a)^{1/2} k^*\ k\cos\psi}{\Psi(k,\psi)\ B(k,\nu)} \qquad (4.2)$$

$$K_{III} = \frac{\tau(\pi a)^{1/2}(1-\nu)k^*\ \sin\psi}{\Psi(k,\psi)\ B(k,\nu)} \qquad (4.3)$$

where

$$B(k,\nu) = (k^*-\nu)E(k) + \nu k^2 F(k)$$

$$F(k) = \int_0^{\pi/2} (1-k^*\ \sin^2\psi)^{-1/2} d\psi$$

For a circular shape, k=1 in the above three equations and they reduce to the solution for an embedded penny shaped crack under uniform tensile and shear stresses as follows:

$$K_I = \frac{2}{\pi}\sigma(\pi a)^{1/2} \qquad (4.1)'$$

$$K_{II} = \frac{4}{(2-\nu)} \tau(\pi a)^{1/2} \cos\psi \qquad (4.2)'$$

$$K_{III} = \frac{4(1-\nu)}{(2-\nu)\pi} \tau(\pi a)^{1/2} \sin\psi \qquad (4.3)'$$

A surface crack is comparable to an edge crack and requires a correction for K_I and K_{II}. Thus Eqs. (4.1) and (4.2) should be multiplied by 1.12 for the surface crack problem. The total energy release rate for mixed mode loading under plane stress conditions is given by:

$$G_t = \frac{K_I^2}{E} + \frac{K_{II}^2}{E} + \frac{1+\nu}{E} K_{III}^2 \qquad (4.4)$$

From Eq. (4.4), the equivalent SIF can be expressed as:

$$K_{eq}(\sigma) = (G_t E)^{1/2} = [K_I^2 + K_{II}^2 + (1 + \nu) K_{III}^2]^{1/2} \qquad (4.5)$$

For fatigue situations, the stresses are replaced by the stress ranges. Dowling [54] has pointed out that the small cracks may be open even during compressive portions of loading cycles so that the entire stress or strain range should be used in the calculation. The Paris law for crack propagation may be written in the following form for mixed mode growth.

not clearly evidenced in Ref 54.

$$\frac{d\ell}{dN} = A[\Delta K_{eq}(\sigma)]^m \qquad (4.6)$$

The above solutions only apply to linear elastic fracture mechanics. For the small crack problem, elastic-plastic fracture mechanics should be considered since net section plastic strains cannot be neglected. The J integral method is a prospective analytical approach and has been successfully applied in mode I loading [55,56]. For mode II and mode III, no J integral solutions are available at the present. Alternative methods are needed for combined tensile and shear loading. Several investigators [57,58] have used correlations between fatigue crack growth rate and parameters expressed in terms of strain and crack length. A strain based intensity factor for mode I, $\Delta K_I(\varepsilon)$, has been defined as follows

$$\Delta K_I(\varepsilon) = Y E \Delta\varepsilon_t \sqrt{\pi a} \qquad (4.7)$$

where Y is geometry factor and E is Young's Modulus. Recently, Imai and Matake [59] also showed that the value of $\Delta K_I^2(\varepsilon)$ is almost equal to the value of $E\Delta J$ for strain less than 0.5 percent total strain range as shown in Fig. 60. One of the materials (S 40 C) is close to the material investigated in this paper. The strain based intensity factor was employed to account for the anomalous behavior of small cracks. In this case, $\Delta\sigma$ was replaced by $E\Delta\varepsilon_t$ and $\Delta\tau$ was replaced by $G\Delta\gamma_t$. The shear and tensile strains are measured on the plane of maximum shear strain. To examine the crack growth along the surface and along the trace of the deepest point, the following two equations are employed:

$$\frac{da}{dN} = A[\Delta K_{eq}(\varepsilon)|\psi = \pi/2]^m \qquad (4.8)$$

$$\frac{dc}{dN} = A^*[\Delta K_{eq}(\varepsilon)|\psi = 0]^{m^*} \qquad (4.9)$$

4.3 Test Results and Discussion

The important feature shown previously in Figs. 9 and 10 is that the crack tip grows alternately between two maximum shear strain planes even near final failure. The driving force for these small cracks is maximum shear strain amplitude and normal strain amplitude acting on the planes of maximum shear strain amplitude. For pure torsion loading, as Fig. 11 shows, the crack grew exclusively on one of the planes of maximum shear strain amplitude. Cracks grow on this weak plane by propagating and coalescing cracks rather than propagating by a single dominant crack.

Figures 61 and 62 show the crack growth curves for different loading modes investigated. In Fig. 61 all three biaxial strain ratio tests with the same equivalent strain amplitude have similar crack growth behavior. The dimension of the growing crack for torsional loading cannot be compared with other loading modes. Full scale of 10 mm was employed in Fig. 62. The crack growth rates on the surface for torsional loading are much faster than other loading modes, but produce a similar depth because of the lower aspect ratio (refer to Table 3).

In Fig. 63, the elastic strain energy was first attempted to correlate crack growth rate into the surface. Crack growth rate was evaluated by three points incremental polynomial method which is recommended by ASTM Standard E647. The crack growth rate for the two equivalent strain amplitude employed in this study cannot be correlated by an equivalent stress intensity factor. By employing a strain based

intensity factor to account for plasticity effects, better correlation was obtained as Fig. 64 shows. Using strain based intensity factor for the crack growth along the surface is also shown in Fig. 65. The result shows that the crack growth rate in these two directions is similar. This correlation should occur because the aspect ratio is assumed constant. Crack growth in these two directions is proportional to the aspect ratio. The energy available on the surface is a little higher than at the deepest point.

The correlation of crack growth rate with strain based intensity factor for torsional loading is plotted in Fig. 66. Similar results have been appeared in another steel [60] which also contained one weak plane due to inclusions effect. Possible reasons for such results are that (1) different propagation law is needed for pure torsion or (2) a propagation law with the consideration of crack coalescence should be employed.

Pearson [61] examined the initiation and crack growth of small cracks in aluminum alloys. He concluded that microcrack growth kinetics are faster than macrocrack growth kinetics. To understand this phenomenon, the results of small cracks in this study were compared with long crack data in Fig. 67. Three series of the tests were performed with same material. The solid line is the small crack growth results from Fig. 64. The dashed line is the long crack results which were obtained from other independent study [62] with compact tension (CT) specimen. The dots-and-dashed line is another set of the long crack results which was obtained with a center cracked tension (CCT) plate specimens. The initial crack length (2a) of CCT specimens was 3.2 mm.

The test results of CCT specimens were shown in Fig. 68. Both long crack results are tested under uniaxial tensile loading. The following observations can be made from the comparison of these three series of tests: (1) By employing strain based intensity factor, the small crack growth rate is almost identical with the long crack growth rate of region II (region of steady crack growth). (2) From CCT specimen results, the threshold stress intensity factor (ΔK_{th}) is 6 MPa $\sqrt{m}$. Compare the results of CCT specimen with the small crack growth shows that small cracks can continuously grow even below the value of ΔK_{th}. This confirmed that the microcrack growth kinetics is faster than macrocrack growth kinetics below the threshold region of long crack.

One of the difficulties involved in this research is in determining the aspect ratio. Since crack depth cannot be measured during the test. The effect of aspect ratio on the crack growth results is examined. Eqs. (4.1) through (4.3) can be rewritten with a single geometry factor.

$$K_I = Y_1 \sigma(\pi a)^{1/2} \qquad (4.1)''$$

$$K_{II} = Y_2 \tau(\pi a)^{1/2} \qquad (4.2)''$$

$$K_{III} = Y_3 \tau(\pi a)^{1/2} \qquad (4.3)''$$

where

$$Y_1 = \frac{1.12\ \Psi(k,\psi)}{E(k)}$$

$$Y_2 = \frac{1.12\ k^*\ k\cos\psi}{\Psi(k,\psi)\ B(k,\nu)}$$

$$Y_3 = \frac{(1-\nu)\ k^*\sin\psi}{\Psi(k,\psi)\ B(k,\nu)}$$

Geometry factors Y_1, Y_2, and Y_3 depend on aspect ratio, poisson ratio, parametric angle, and loading condition. The variation of geometry factors as a function of aspect ratio are plotted in Figs. 69 and 70.

As shown in Fig. 69, within an aspect ratio range of 0.5 to 1.0, the geometry factors are almost constant for the crack growth along the surface. For the same range of aspect ratios, Fig. 70, the variation of geometry factors for the crack growth into the surface along the trace of the deepest point deviate about 10 percent from average value. The above results show that if the average aspect ratio is known, the assumption of fixed aspect ratio only induces a 10 percent error in the calculation. The approach employed in this study could be an important step to the engineering application. If the measurement of total tensile and shear strain amplitudes on the maximum shear strain plane and long crack growth data are available, the fatigue life of small cracks subjected to the combined stress/strain state can be predicted.

Since the energy release rate has been considered to be a driving force for crack growth, some of the researchers [63,64] suggested that for an existing crack, the crack will propagate in the direction of maximum energy release rate. The direction is also the principal direction in which the shear stress vanishes. In this study, the maximum shear strain and the normal strain acting on the plane of maximum shear strain are used to generate equivalent strain based intensity factor. The square of the equivalent strain based intensity factor corresponds to the total energy release rate multiplied by Young's modulus as shown in Eq. (4.5). The comparison of total energy release rate and total shear strain range with respect to the surface

crack direction is shown in Figs. 71 and 72. Energy release rate is expressed as the strain based intensity factor normalized by crack depth. For the case of pure tension loading in Fig. 71, the maximum energy release rate occurred where total shear strain vanishes. Previous studies [63,64] have shown this for the long crack growth under mode I loading. However, as observed from the photographs in Fig. 9 and the results of Fig. 71, the maximum energy release rate is not a necessary condition to cause crack extension for small cracks under fatigue loading.

The early stages of crack nucleation and growth are controlled by the cyclic shear strain. In tension loading, the cracks start on planes of maximum shear strain and then turn to planes of maximum energy release rate as they become long cracks. Figure 71 shows that this behavior can be expected. For pure torsion, Fig. 72 shows that the total shear strain and maximum energy release rate both occur on the same plane. This implies that the cracks nucleate and continue to grow on planes of maximum shear strain even for long cracks. The transition behavior of the crack direction should not occur.

4.4 Conclusions

1. With the Strain based intensity factor and the total energy release rate criterion, the extended Paris law is applicable to the combined tension-torsion loading within the tested strain ratios in the high cycle fatigue region.
2. The crack growth rate of small cracks under combined tension-torsion loading could be predicted by long crack data under uniaxial loading.

3. Different propagation law for torsional loading is needed for the materials containing inclusions on one of the maximum shear strain planes.

5. RECOMMENDATIONS

In this investigation, the applicability of life prediction by the damage curve approach has been confirmed with two-level block loading. As being pointed out by Marco and Starkey [5], the damage curves of different crack systems have their own unique shapes. The damage by Type-S crack system accumulated very slowly during the early cycles of life (initiation phase), but the rate of damage was very high during the latter stage of the life (propagation phase). On the contrary, Type-R crack system follows a different shaped damage curve. During the early cycles, many cracks were accumulating damage simultaneously. Thus, damage progressed more rapidly during the early stage than in the corresponding period of Type-S crack system. However, the increase in damage rate at later stages was not as large as the increase for the Type-S crack system. The shape difference between these two damage curves implies that the life prediction in complex loading might be analyzed by only two damage curves (hereafter called dual damage curve method). One is for Type-R crack system, the other is for Type-S crack system. At different loading levels, the damage curves are not identical. However, this difference is overwhelmed by the difference in crack systems.

To achieve the goal of life prediction for complex loading, the following future studies are recommended:

(1) The effect of mean stress on the transition life of Type-R crack systems to Type-S crack system should be investigated.

(2) The life prediction of random loading might be analyzed by the dual damage curve method. Once the effect of mean stress is

understood, the fatigue life of complex loading can be predicted by classifying all loading cycles into two different crack systems. Thus the prediction could be made by two damage curves only.

(3) Many engineering components are subjected to out of phase loading. The study of non-proportional loading to crack systems are needed for engineering applications.

Table 1 Mechanical Properties of 1045 Steel

Axial monotonic properties	
Yield Stress (0.2 percent)	380 MPa
Fracture Stress	985 MPa
Fracture Strain	0.71
Percent Reduction in Area	50
Strain Hardening Exponent	0.23
Strength Coefficient	1185 MPa
Modulus of Elasticity	205 GPa
Axial cyclic poperties	
Fatigue Ductility Coefficient	0.20
Fatigue Ductility Exponent	-0.43
Fatigue Strength Coefficient	980 MPa
Fatigue Strength Exponent	-0.11

Table 2 Constant Amplitude Loading Results

I. $\Delta\bar{\varepsilon}/2 = 0.01$

ID	λ	$\frac{\Delta\varepsilon}{2}$	$\frac{\Delta\gamma}{2}$	$\frac{\Delta\sigma}{2}$(MPa)	$\frac{\Delta\tau}{2}$(MPa)	N_f
4527	0	0.01	-	450	-	1137
4553	0	0.01	-	450	-	1107
4524	0.5	0.0096	0.0048	427	79	1258
4525	1	0.00866	0.00866	381	131	1616
4533	1	0.00866	0.00866	381	131	1229
4526	2	0.00655	0.0131	288	195	1758
4549	∞	-	0.0173	-	251	890
4537	∞	-	0.0173	-	251	889

II. $\Delta\bar{\varepsilon}/2 = 0.0043$

ID	λ	$\frac{\Delta\varepsilon}{2}$	$\frac{\Delta\gamma}{2}$	$\frac{\Delta\sigma}{2}$(MPa)	$\frac{\Delta\tau}{2}$(MPa)	N_f
4545	0	0.0043	-	352	-	7839
4523	0.5	0.00413	0.00206	338	55	11777
4515	1	0.00372	0.00372	305	107	11611
4520	1	0.00372	0.00372	305	107	10377
4501	2	0.0026	0.0052	234	153	20031
4503	2	0.0026	0.0052	234	153	16887
4506	∞	-	0.0072	-	197	8710

Table 2 Constant Amplitude Loading Results (continued)

III. $\Delta\bar{\varepsilon}/2 = 0.0022$

ID	λ	$\frac{\Delta\varepsilon}{2}$	$\frac{\Delta\gamma}{2}$	$\frac{\Delta\sigma}{2}$(MPa)	$\frac{\Delta\tau}{2}$(MPa)	N_f
4511	0	0.0022	-	273	-	142541
4552	0	0.0022	-	273	-	78271
4529	0	0.0022	-	273	-	94525
4516	0.5	0.0021	0.00106	266	52	115462
4528	0.5	0.0021	0.00106	266	52	80000*
4514	1	0.0019	0.0019	238	88	123544
4550	1	0.0019	0.0019	238	88	90000*
4522	2	0.00144	0.00288	179	126	98778
4548	2	0.00144	0.00288	179	126	87500*
4512	∞	-	0.00381	-	168	102083
4551	∞	-	0.00381	-	168	57369
4531	∞	-	0.00381	-	168	93052

IV. $\Delta\bar{\varepsilon}/2 = 0.0015$

ID	λ	$\frac{\Delta\varepsilon}{2}$	$\frac{\Delta\gamma}{2}$	$\frac{\Delta\sigma}{2}$(MPa)	$\frac{\Delta\tau}{2}$(MPa)	N_f
4519	0.5	0.00144	0.00072	224	43	611780
4517	1	0.0013	0.0013	212	80	595613
4554	1	0.0013	0.0013	212	80	393633
4521	2	0.00098	0.00196	147	111	545840
4518	∞	-	0.0026	-	147	1010210

*Test stopped after a visible crack (1 to 3 mm) was detected.

Table 3 Summary of Crack Aspect Ratio (a/2c)

	$\lambda = 0$	$\lambda = 1$	$\lambda = \infty$
	0.43^{+}	0.36^{+}	0.05^{+}
	---	0.39^{+}	0.066^{+}
	---	0.45^{+}	0.084^{+}
Samples			
Average	0.43	0.4	0.067

Note: (+) These are average values of measured points of an individual sample.

Table 4 Summary of Step Loading Results

ID	λ	Sequence	n_1	β_1*	n_2	β_2^*	β_{2p}^*	$\beta_1 + \beta_2$	$\beta_1 + \beta_{2p}$
4542	0	Lo-Hi	43000	0.41	1122	1.0	0.85	1.41	1.26
4539	1	Lo-Hi	56000	0.49	885	0.62	0.75	1.11	1.24
4536	∞	Lo-Hi	42000	0.5	572	0.64	0.7	1.14	1.2
4535	0	Hi-Lo	550	0.49	33055	0.3	0.2	0.79	0.69
4538	1	Hi-Lo	700	0.48	39690	0.35	0.21	0.83	0.69
4544	∞	Hi-Lo	450	0.5	18641	0.22	0.28	0.72	0.78

* $\beta_1 = n_1/\hat{N}_1$ = experimental cycle ratio of first level
* $\beta_2 = n_2/\hat{N}_2$ = experimental cycle ratio of second level
* β_{2p} = predicted cycle ratio of second level
* $\hat{N}_i$ = constant mean fatigue life

Table 5 Summary of Block Loading Results ($\lambda = 1$)

ID	Sequence	n_1	β_1	n_2	β_2	ξ	Σ_{exp}	Σ_{pre}
4560	Lo-Hi	10640	0.095	7	0.005	19	0.8	0.87
4570	Lo-Hi	8960	0.08	28	0.02	4	1.08	0.73
4566	Lo-Hi	7280	0.065	49	0.035	1.8	1.1	0.65
4561	Lo-Hi	5600	0.05	70	0.05	1	1.03	0.72
4565	Lo-Hi	560	0.005	133	0.095	0.05	0.97	0.9
4562	Hi-Lo	7	0.005	10640	0.095	19	0.9	0.92
4568	Hi-Lo	28	0.02	8960	0.08	4	0.85	0.78
4567	Hi-Lo	49	0.035	7280	0.065	1.8	0.96	0.7
4564	Hi-Lo	70	0.05	5600	0.05	1	0.7	0.76
4571	Hi-Lo	133	0.095	560	0.005	0.05	1.0	0.96

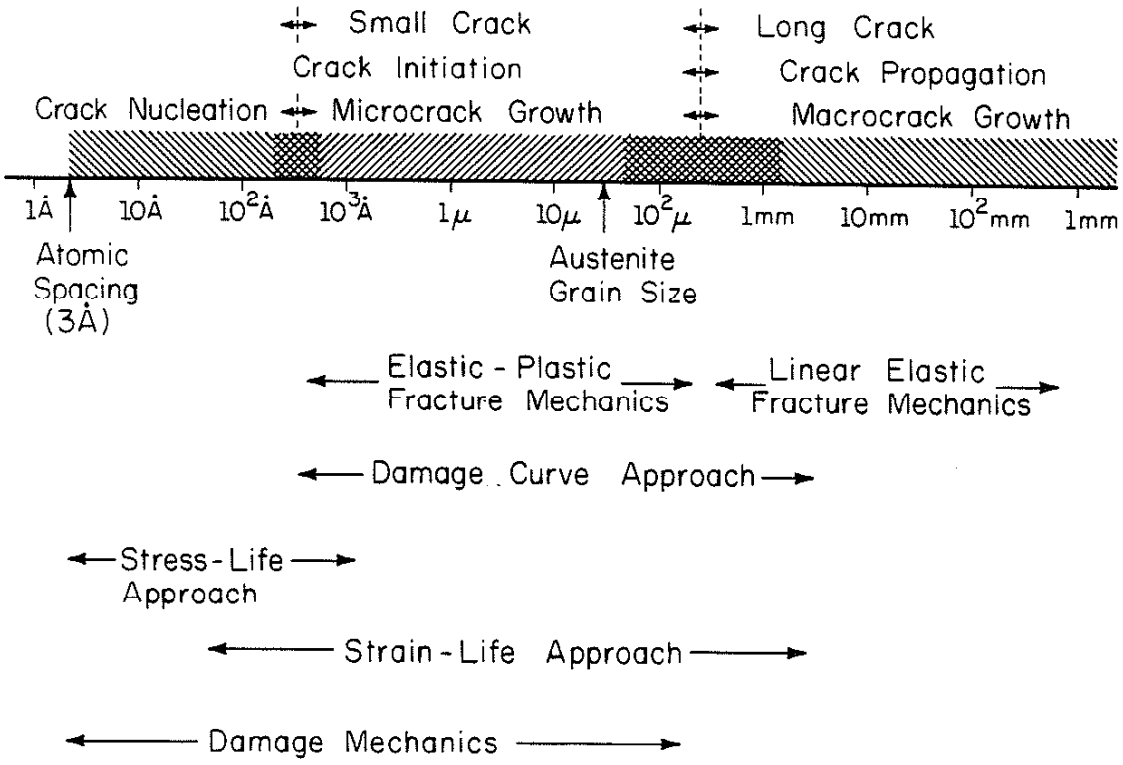

Figure 1 Approaches for fatigue analysis

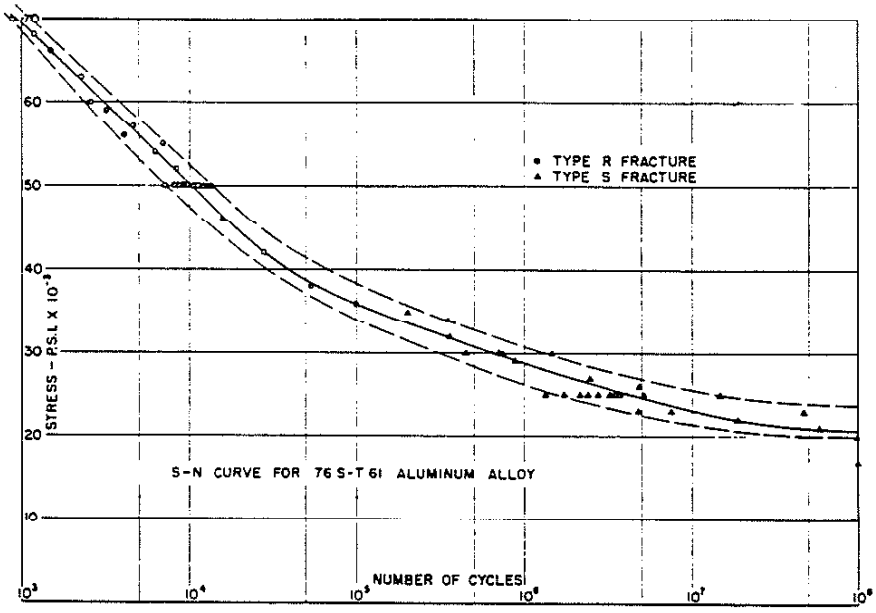

(*left*) *S-N* Curve for 76S-T61 Aluminum Alloy

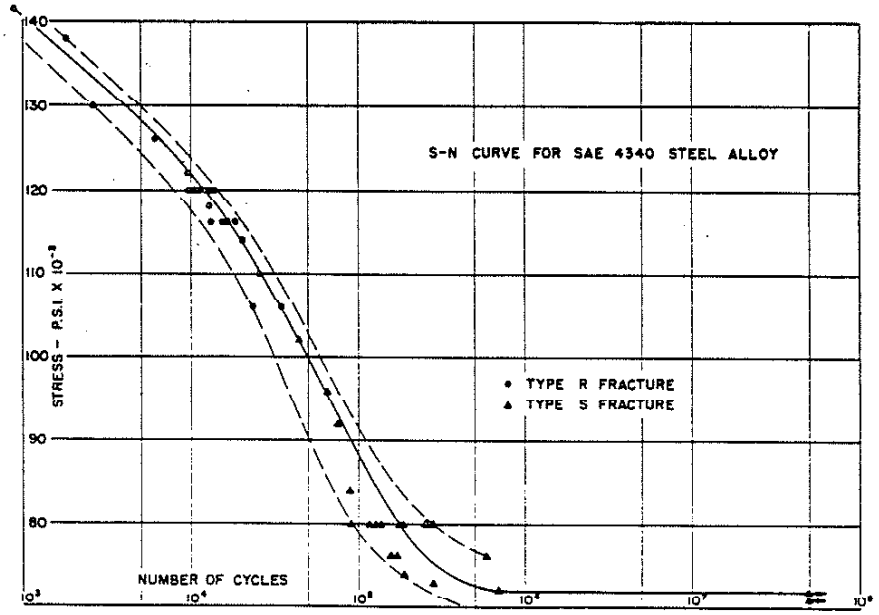

(*right*) *S-N* Curve for SAE 4340 Steel Alloy

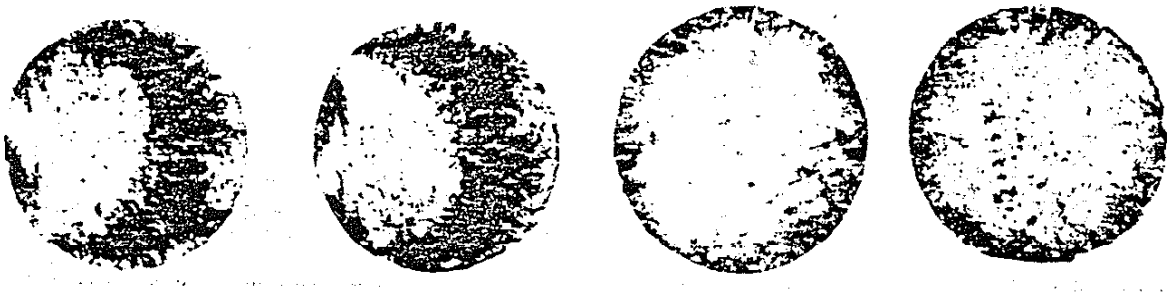

Type-S Fatigue Fracture of 76S-T61 Aluminum Alloy

Type-R Fatigue Fracture of 76S-T61 Aluminum Alloy

Figure 2 Observations of different crack systems [5].

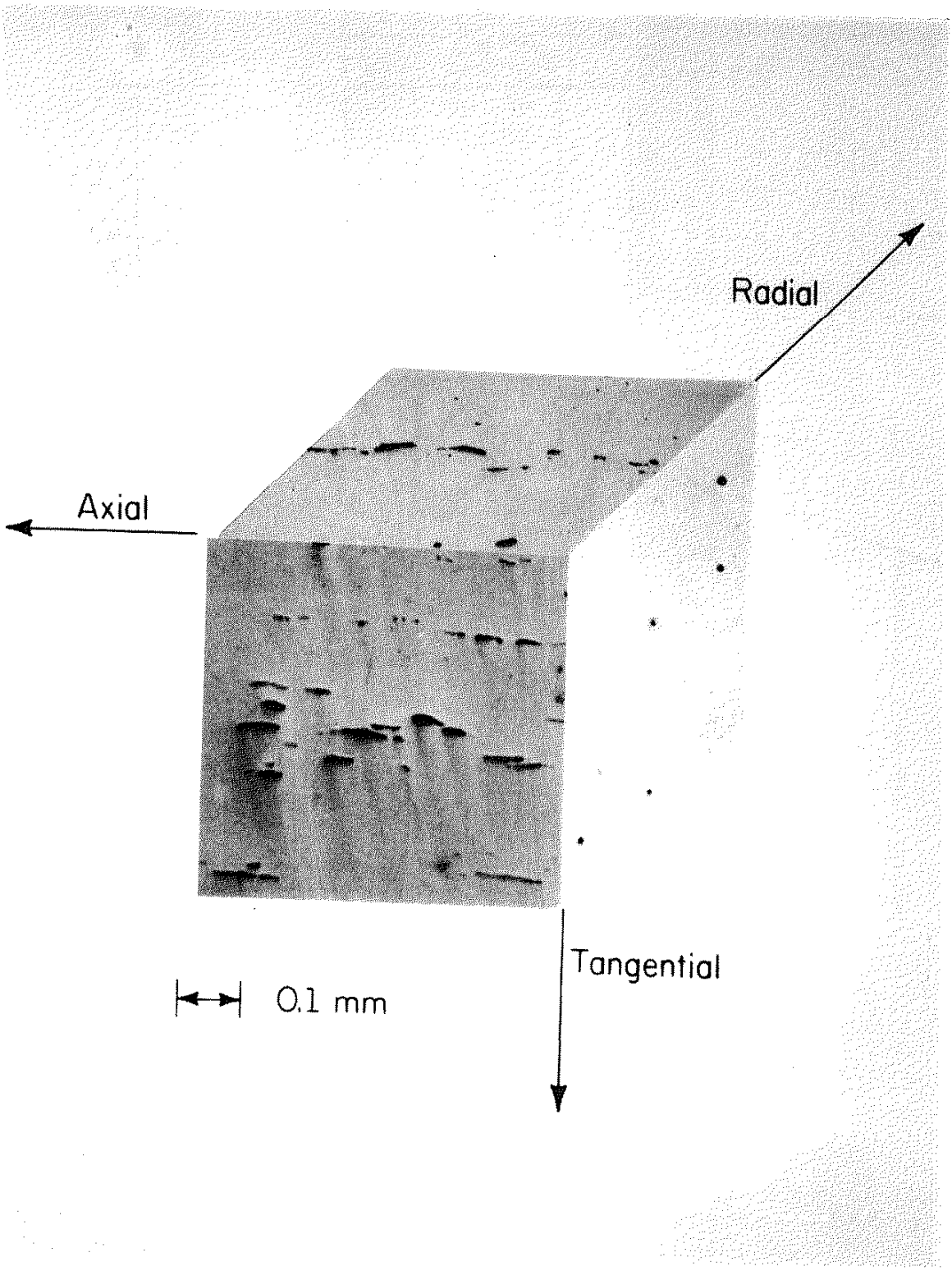

Figure 3 Unetched microstructure showing sulfide inclusions.

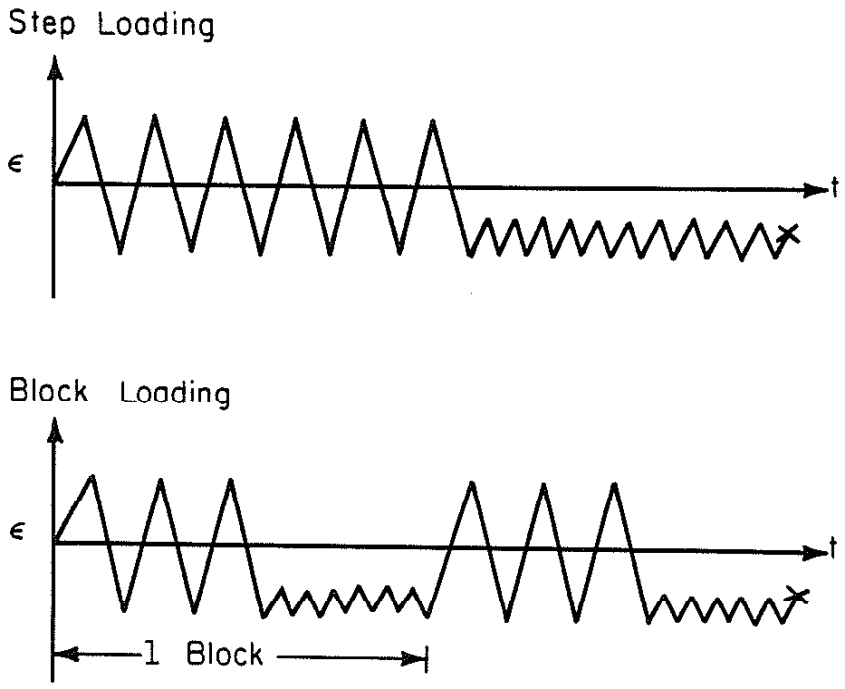

Figure 6 Variable loading patterns.

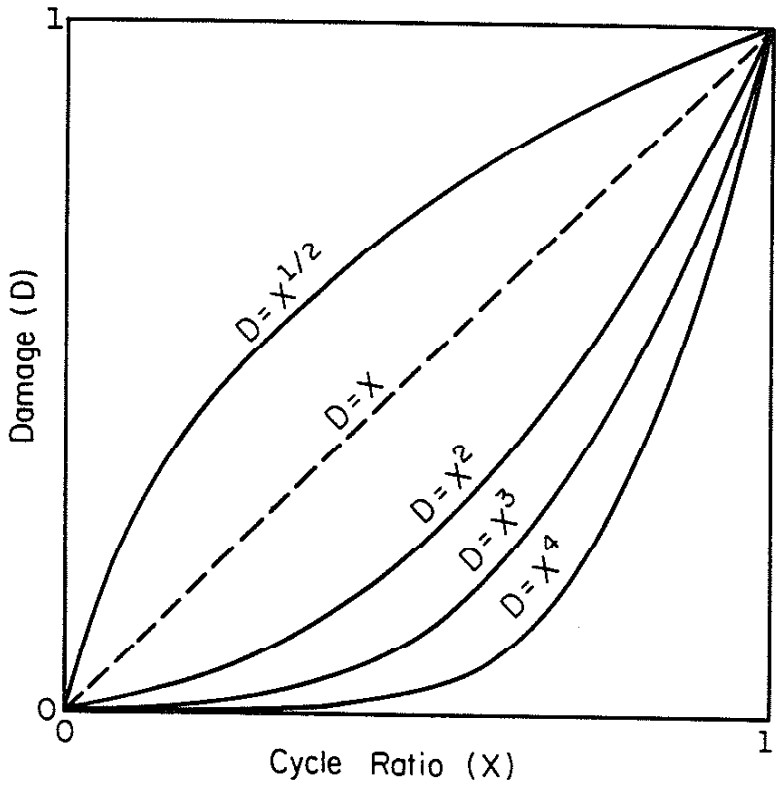

Figure 7 Damage curve concept

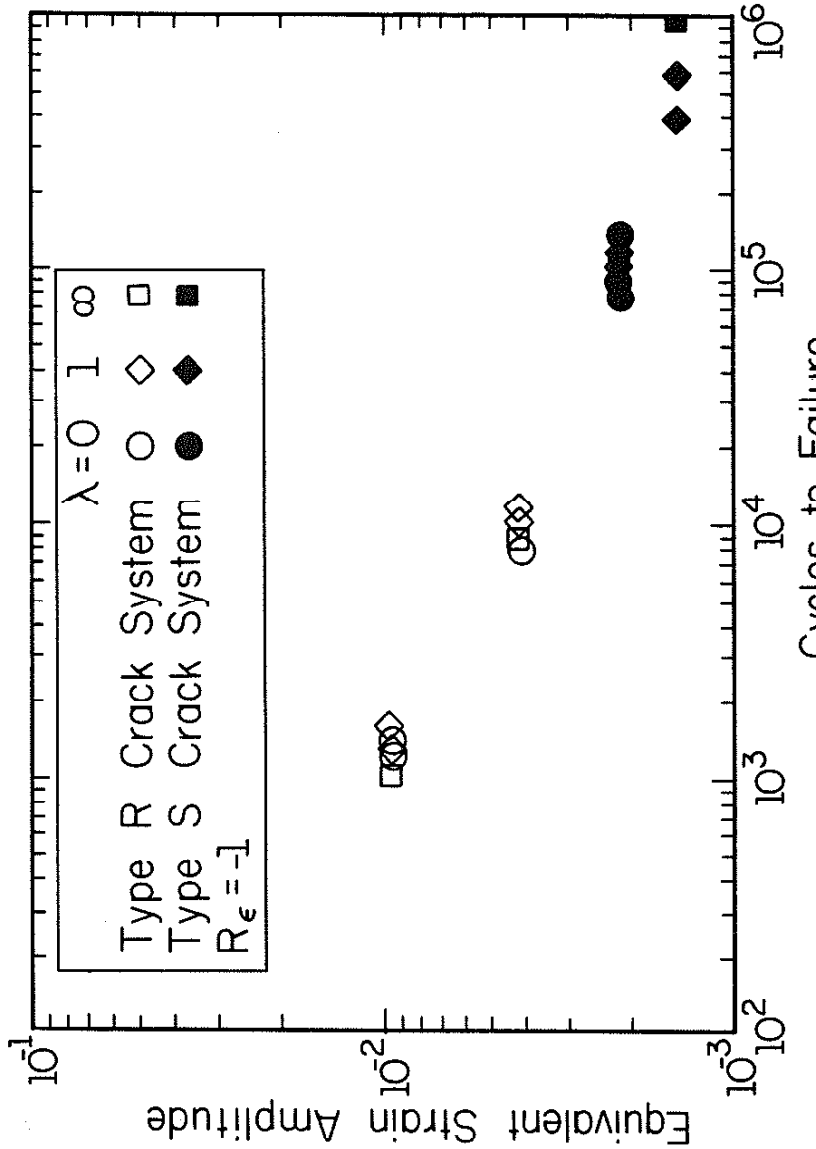

Figure 8 Strain-life curve under biaxial loading.

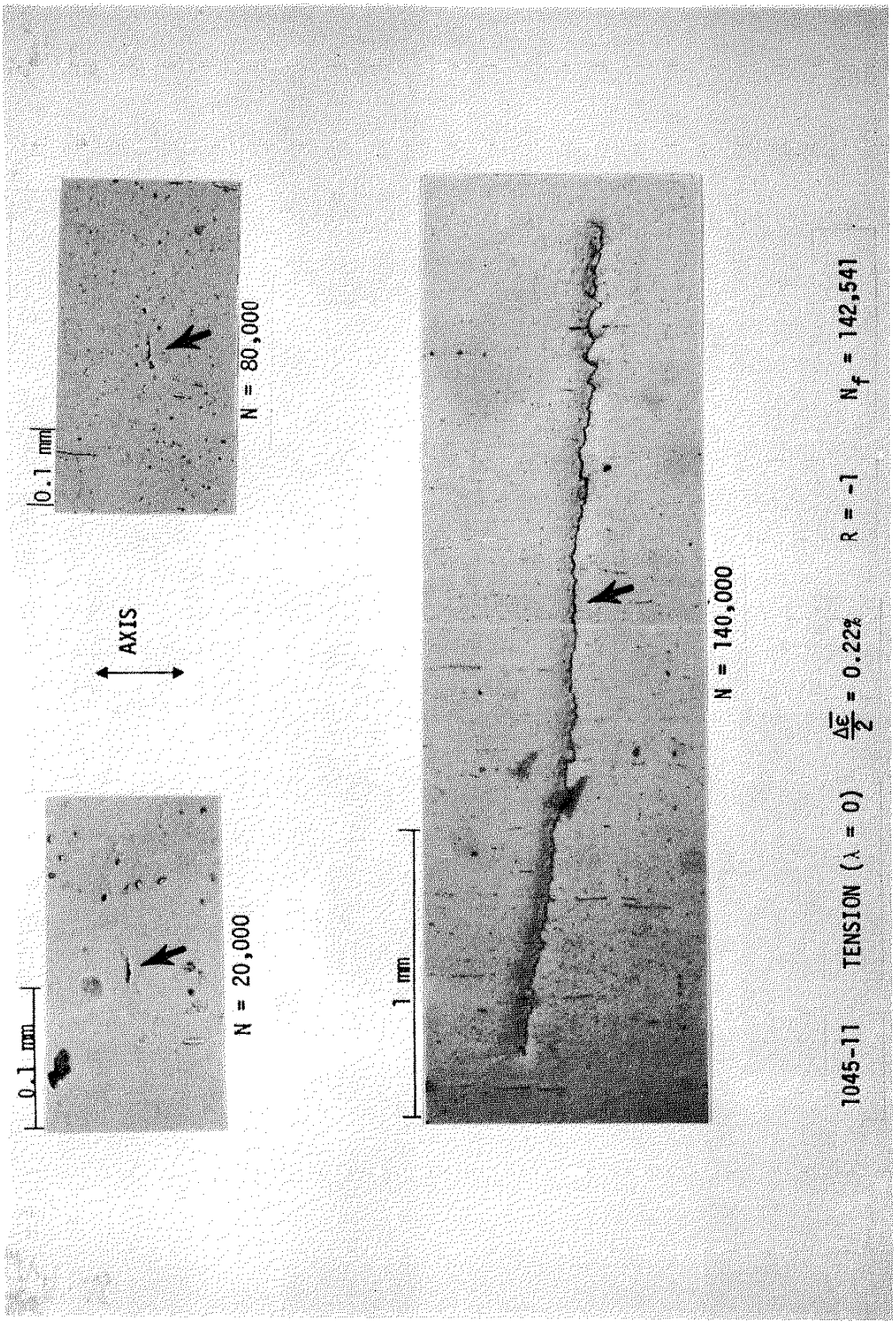

Figure 9 Type-S crack growth under constant loading, $\lambda = 0$.

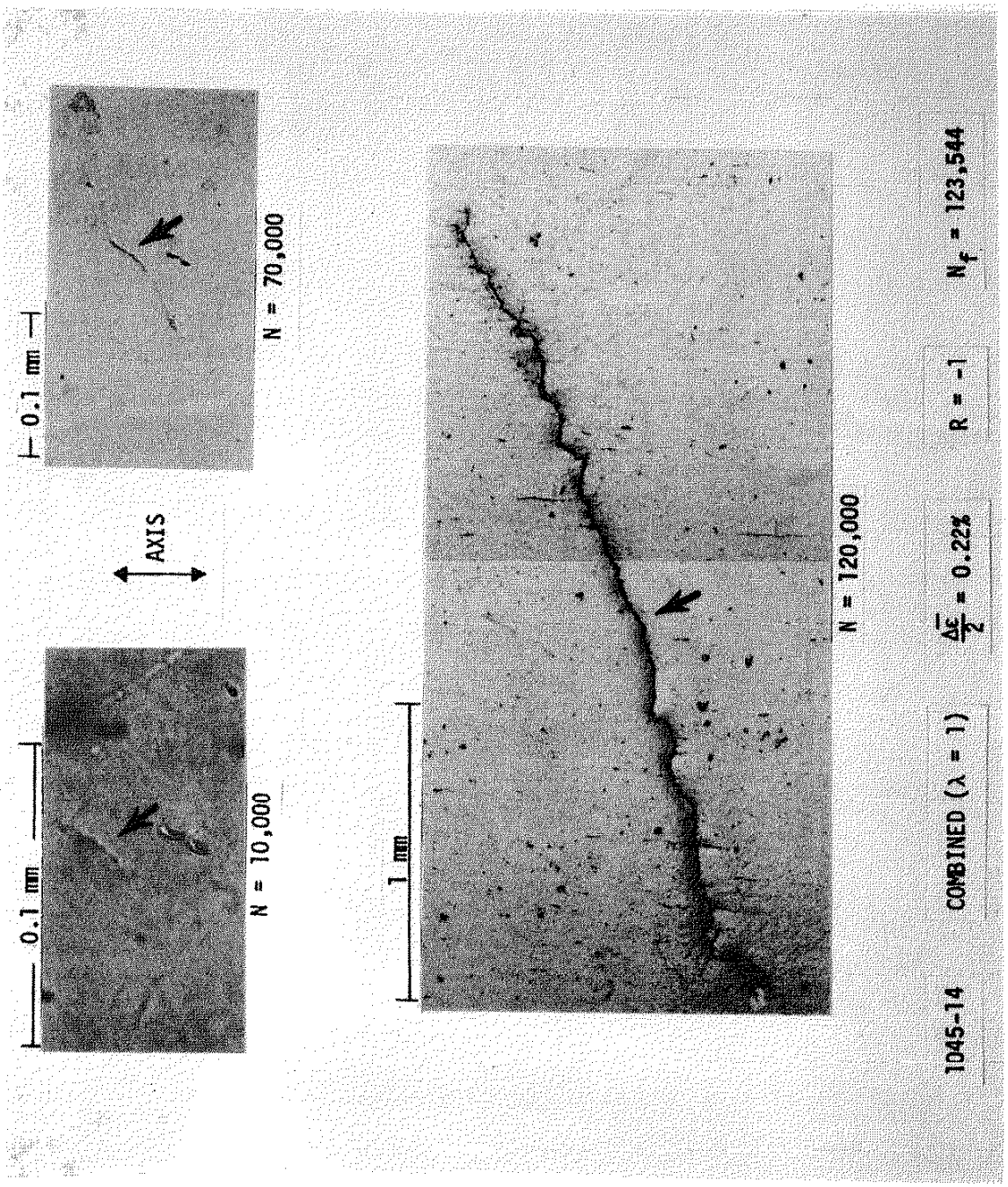

Figure 10 Type-S crack growth under constant loading, $\lambda = 1$.

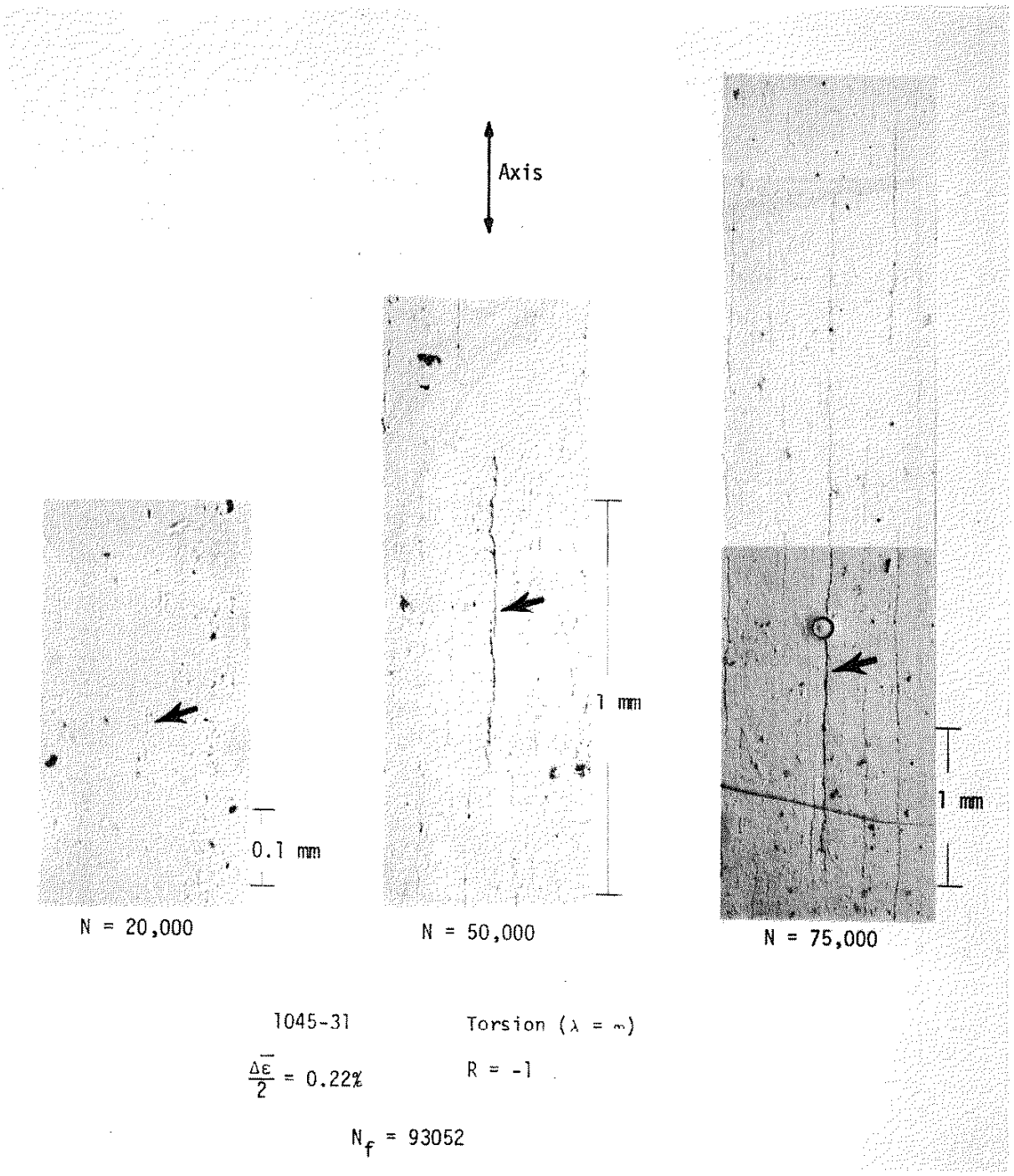

Figure 11 Type-S crack growth under constant loading, $\lambda = \infty$.

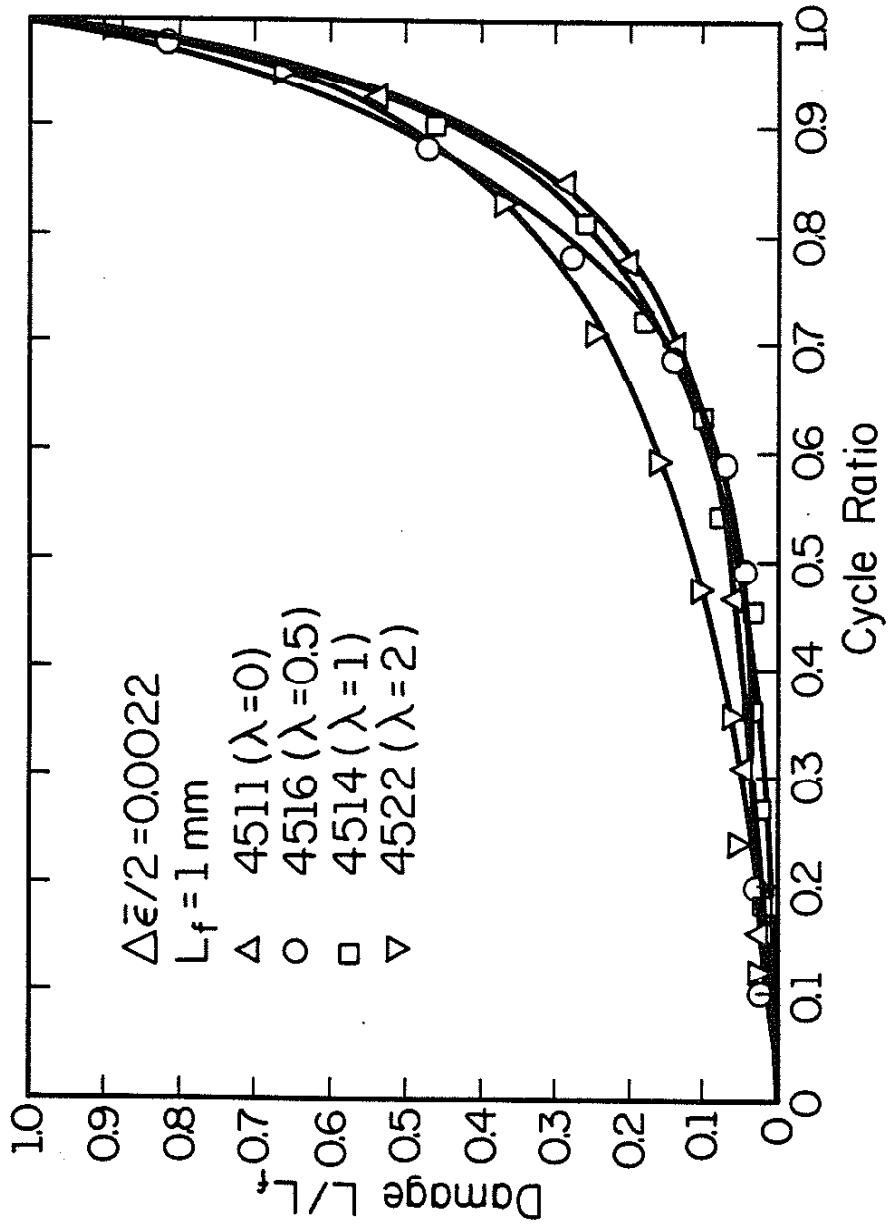

Figure 12 Damage curve for Type-S crack, λ = 0, 0.5, 1 and 2.

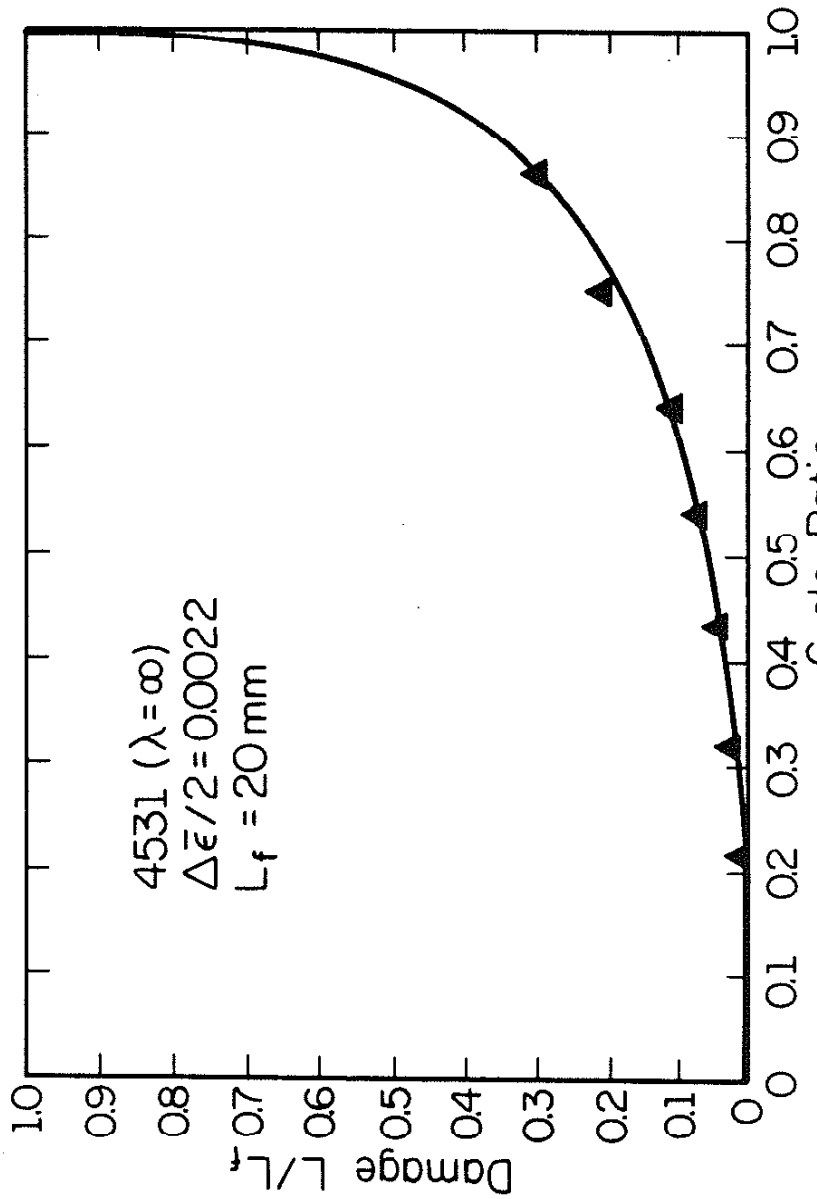

Figure 13 Damage curve for Type-S crack, $\lambda = \infty$.

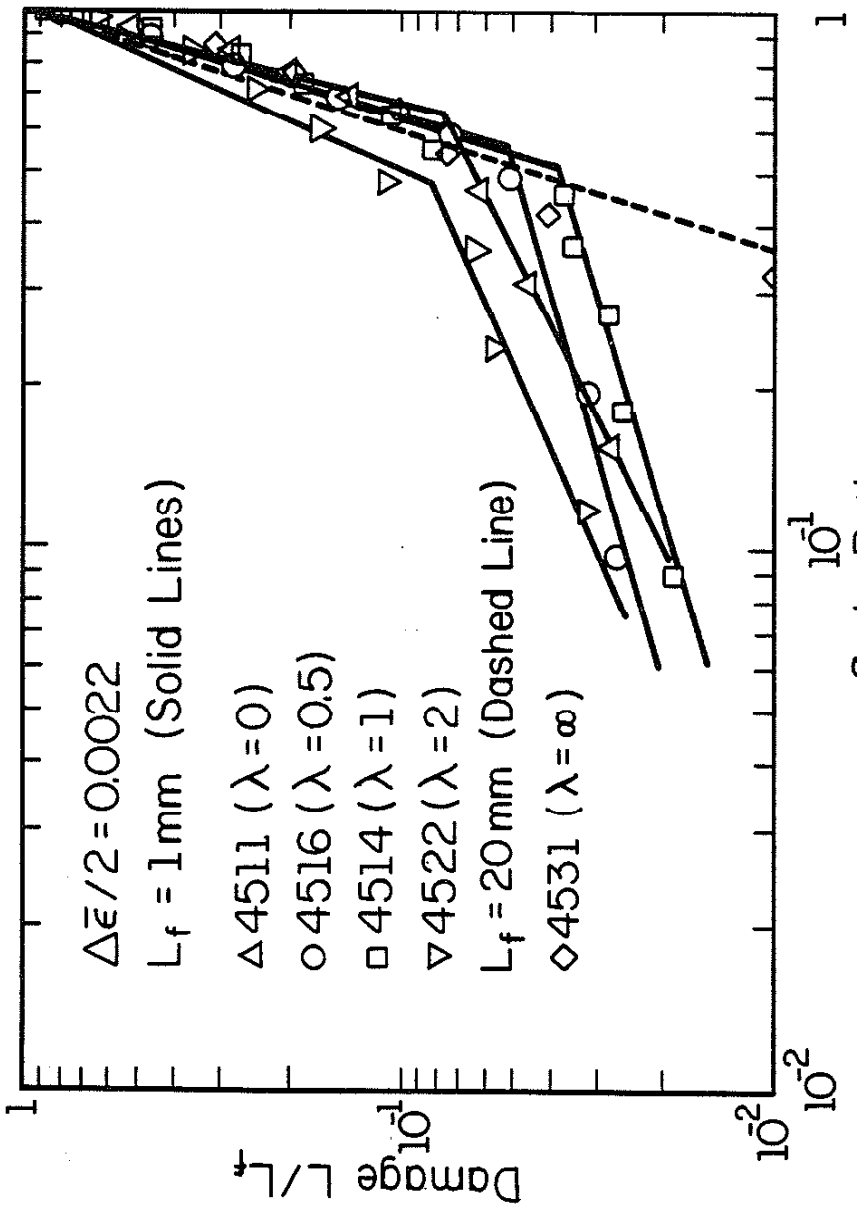

Figure 16 Damage curves for Type-S crack in log-log scale.

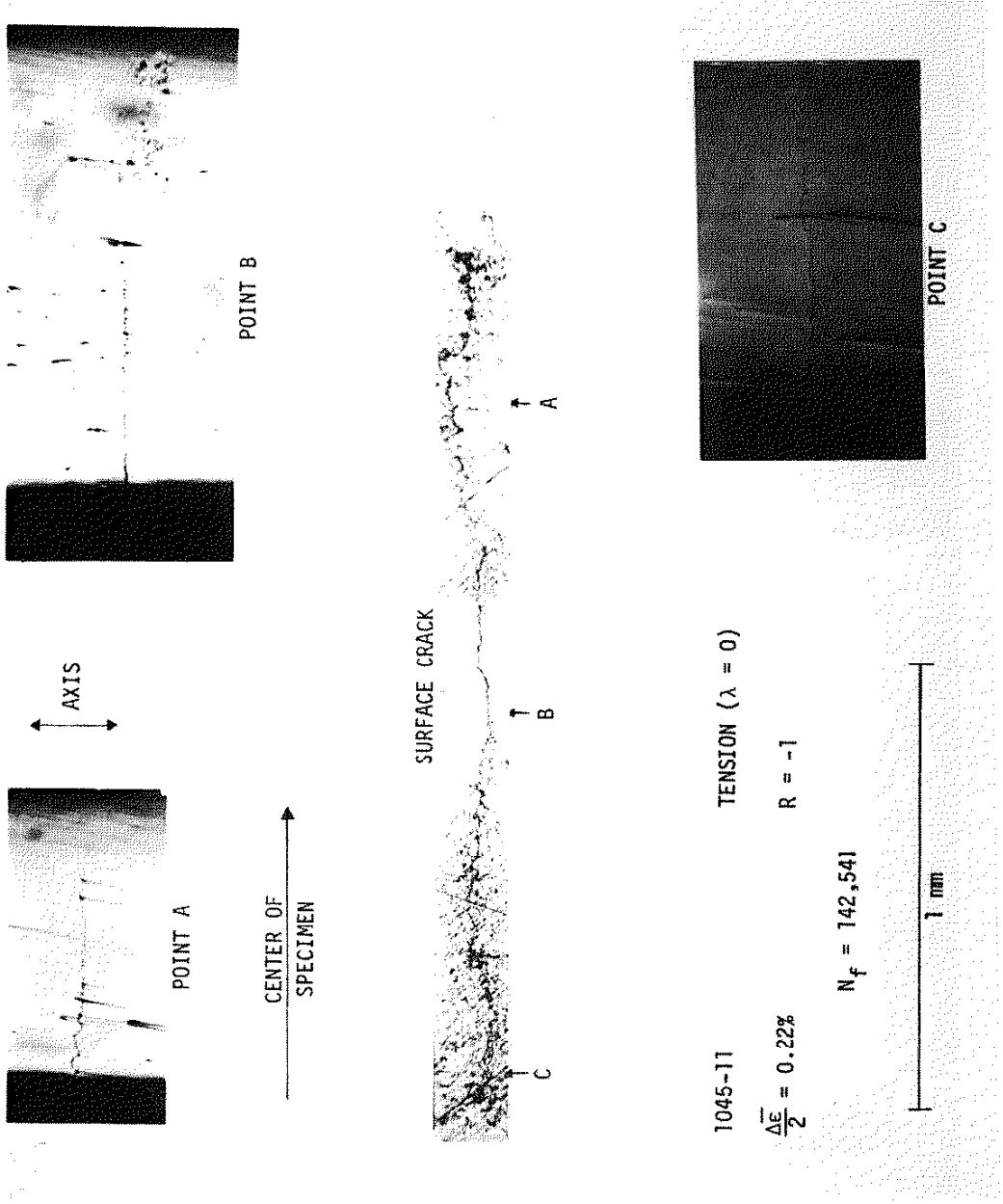

Figure 17 Type-S crack growth into surface, λ = 0.

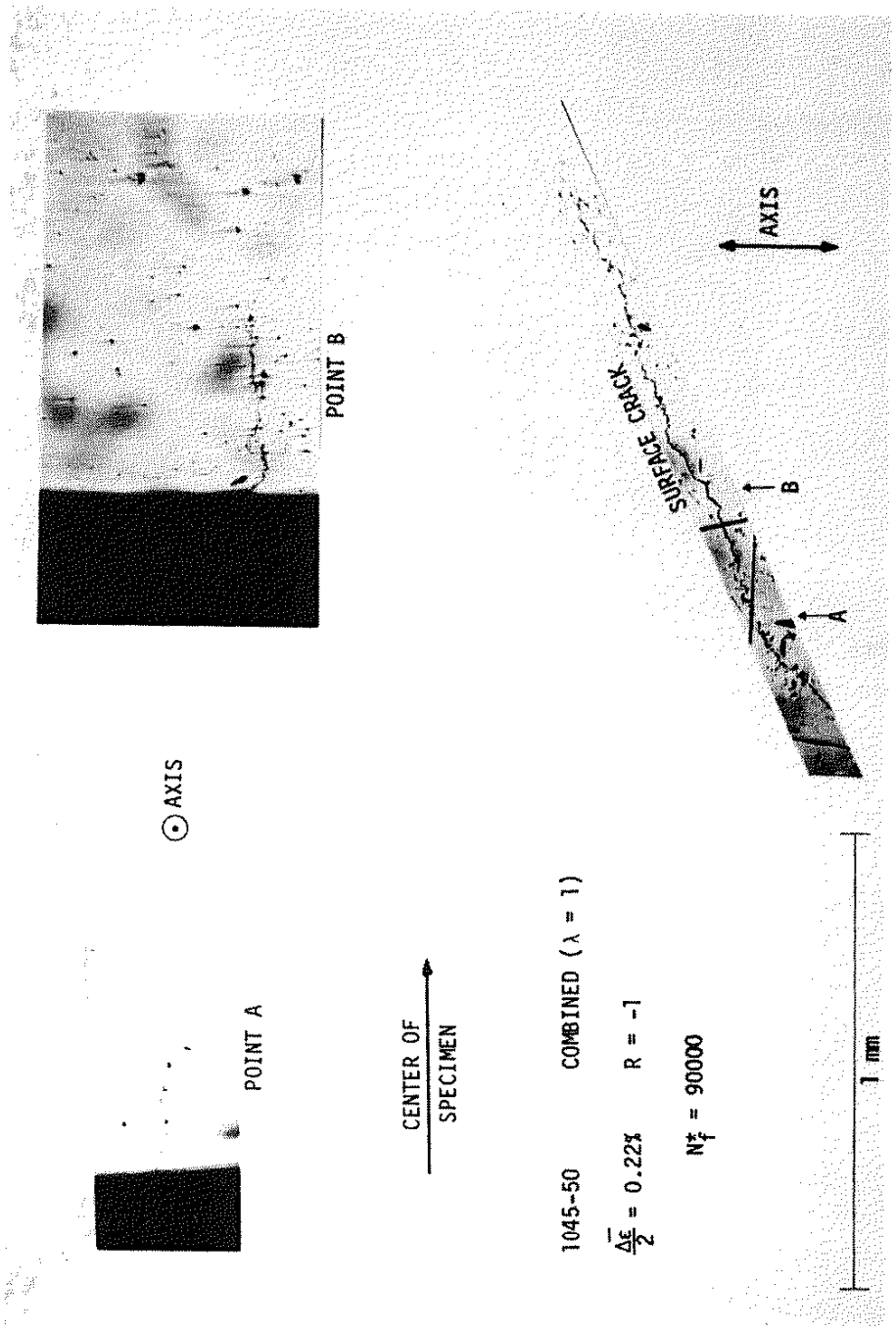

Figure 18 Type-S crack growth into surface, λ = 1.

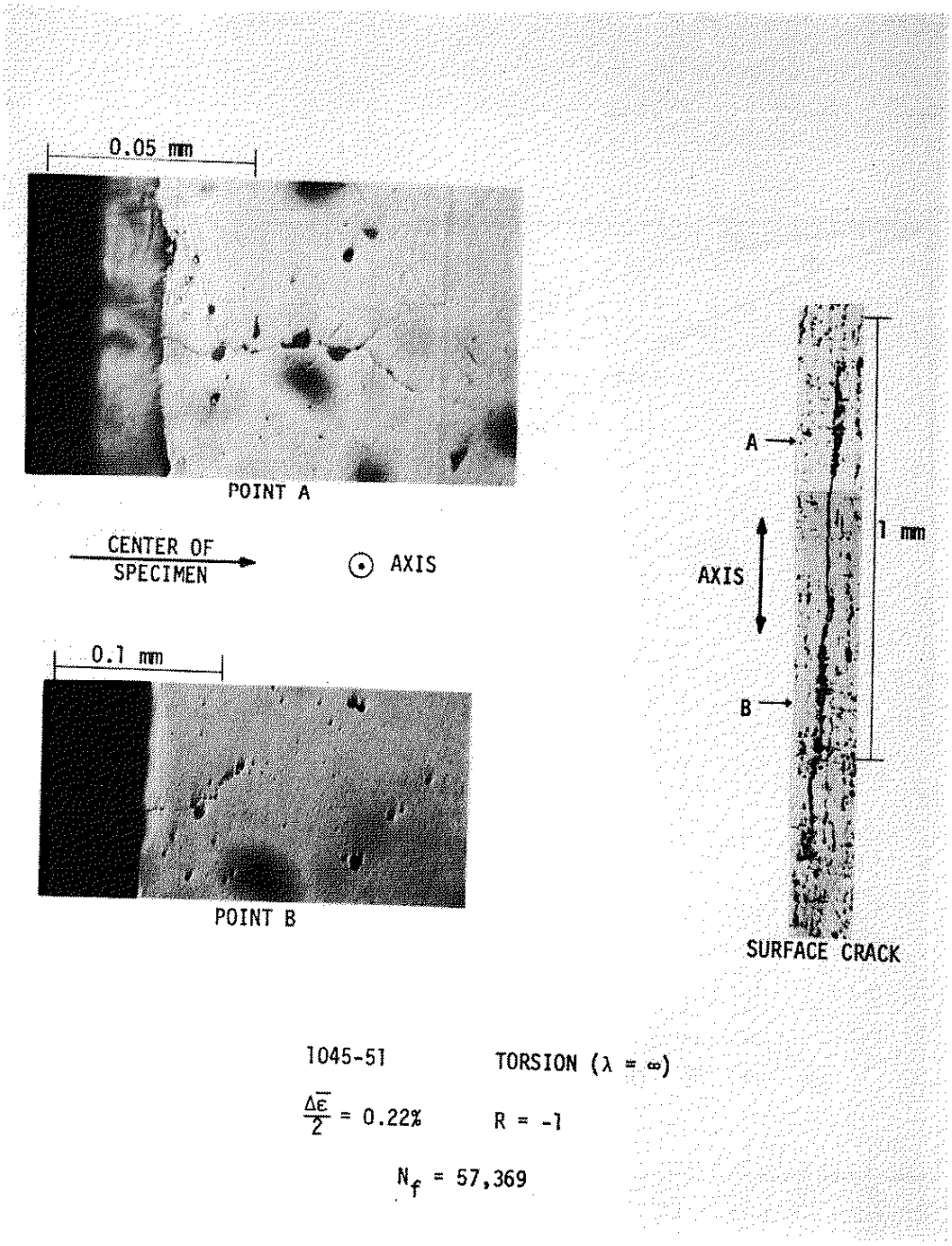

Figure 19 Type-S crack growth into surface, $\lambda = \infty$.

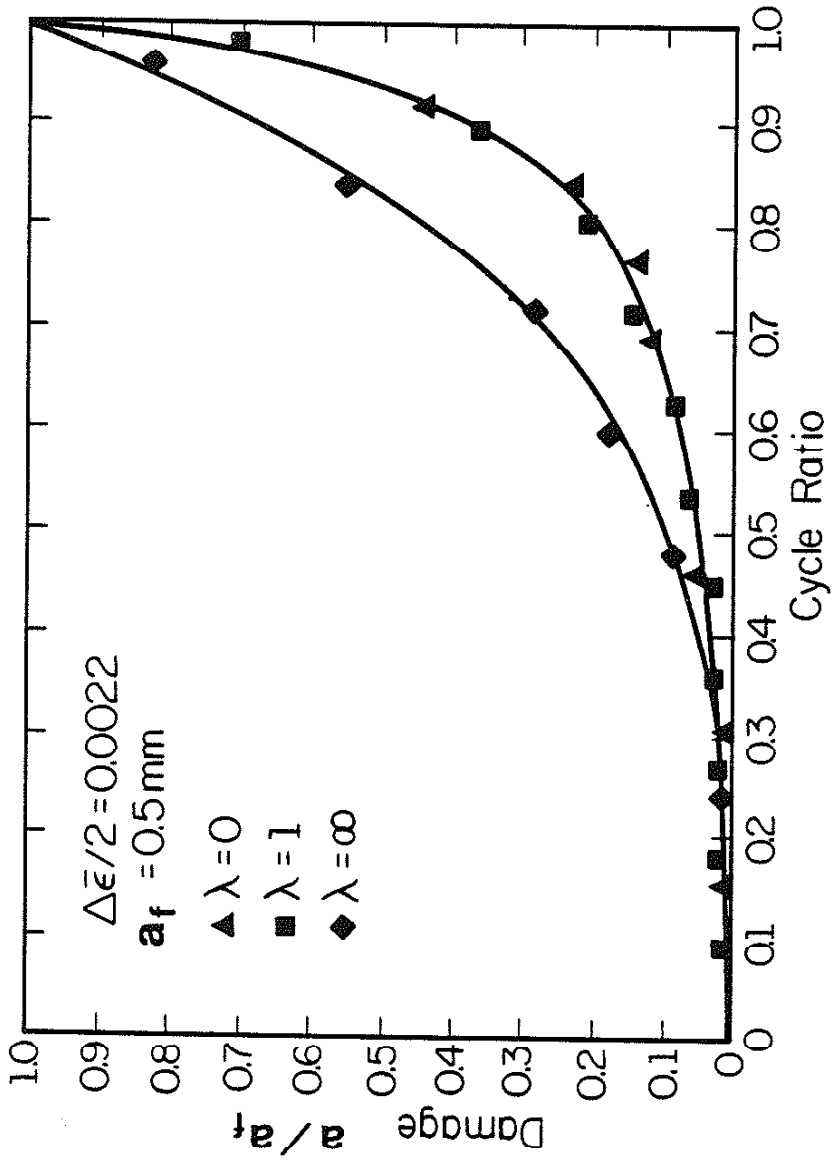

Figure 20 Damage curves for Type-S crack systems under different loading modes.

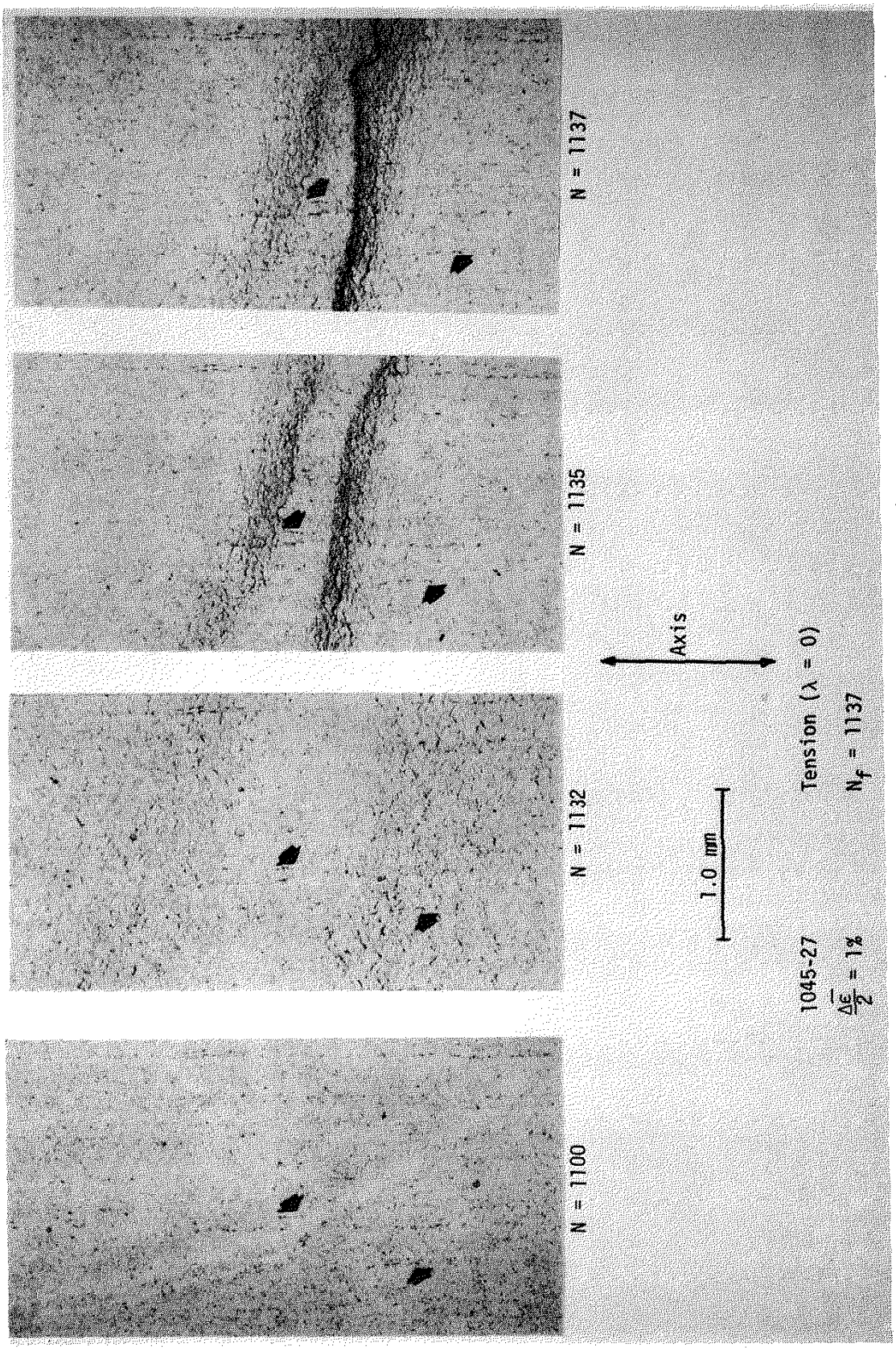

Figure 21 Failure process by Type-R crack system.

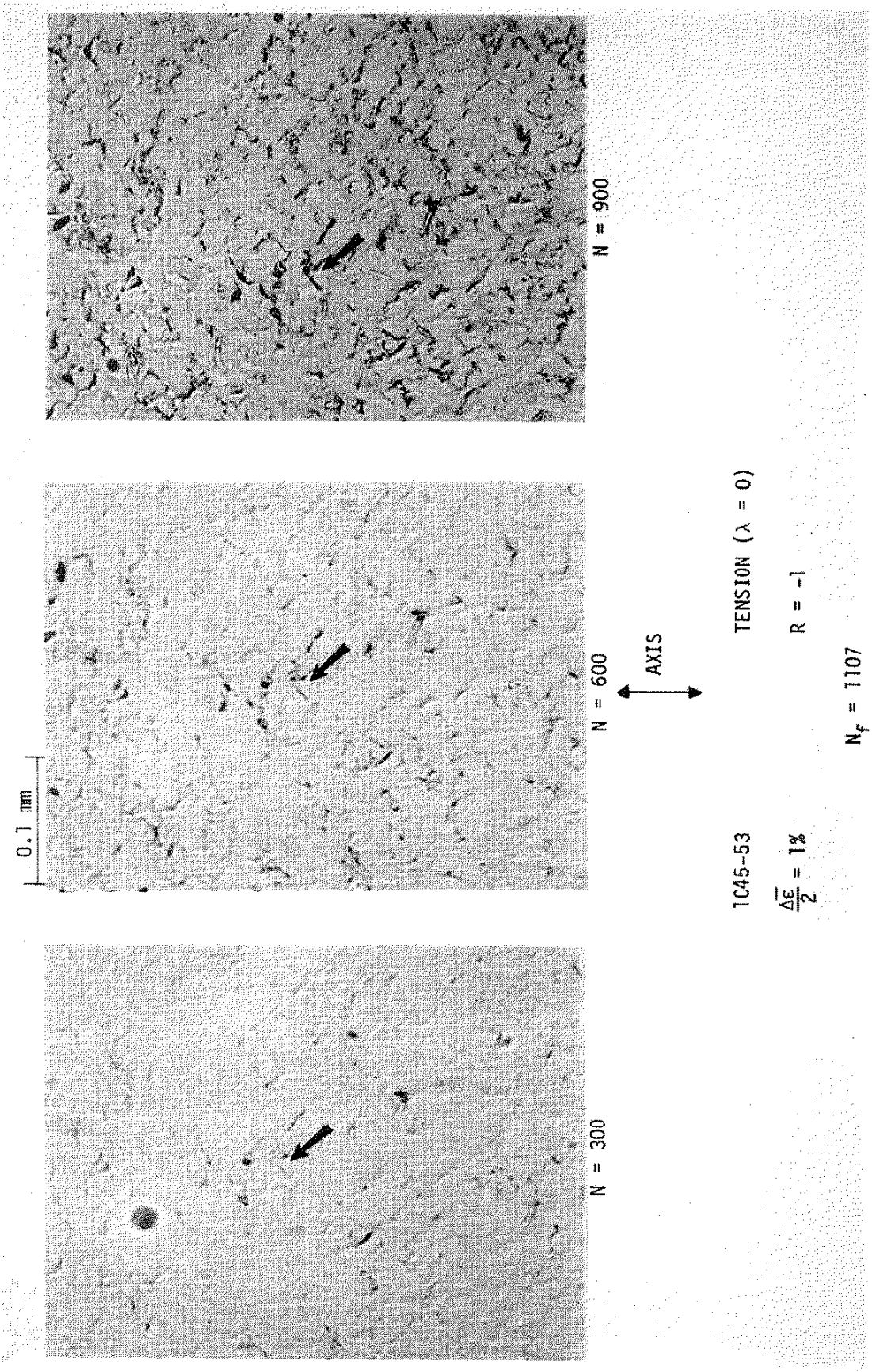

Figure 22 Type-R crack growth under constant loading, $\lambda = 0$.

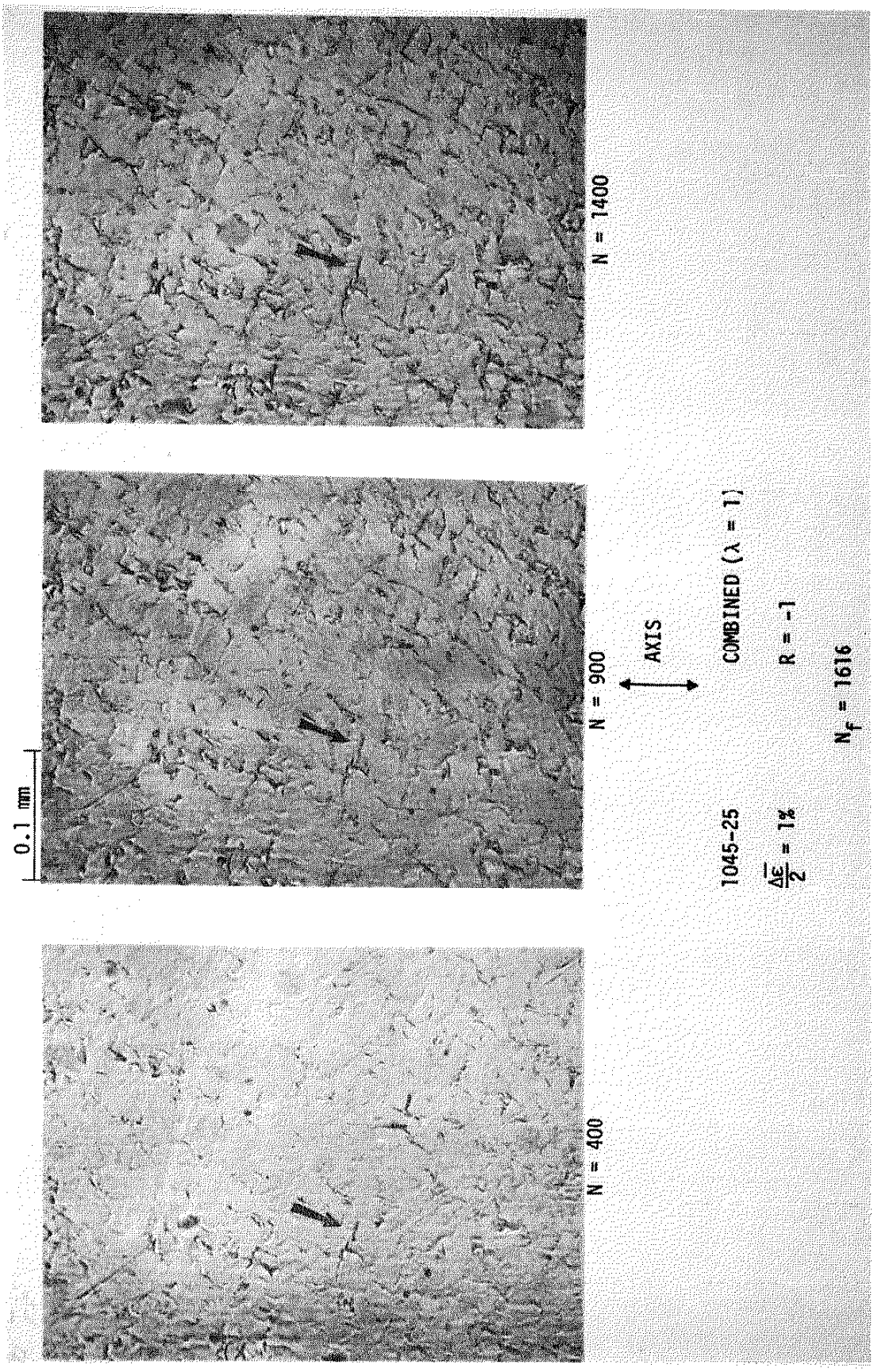

Figure 23 Type-R crack growth under constant loading, $\lambda = 1$.

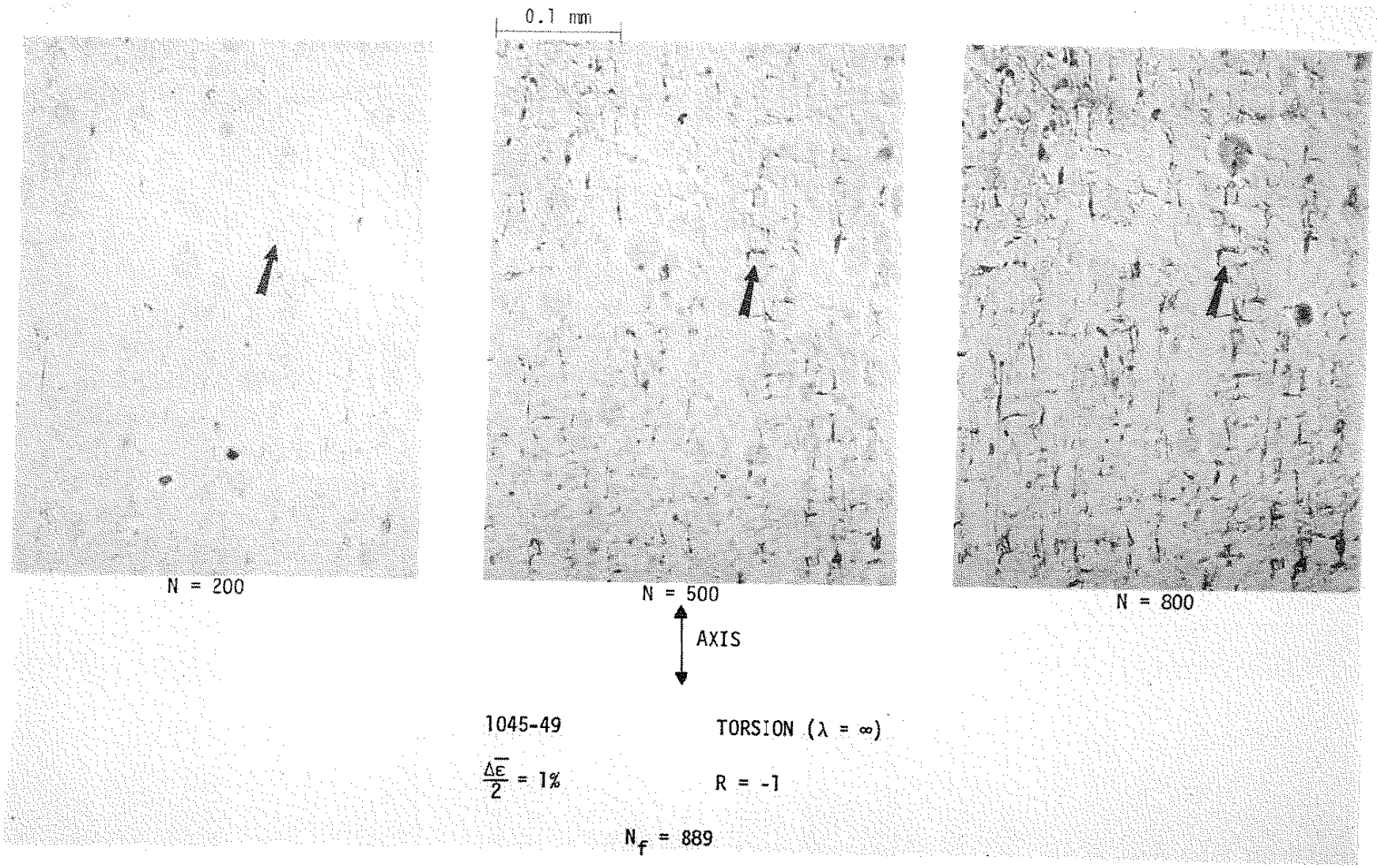

Figure 24 Type-R crack growth under constant loading, $\lambda = \infty$.

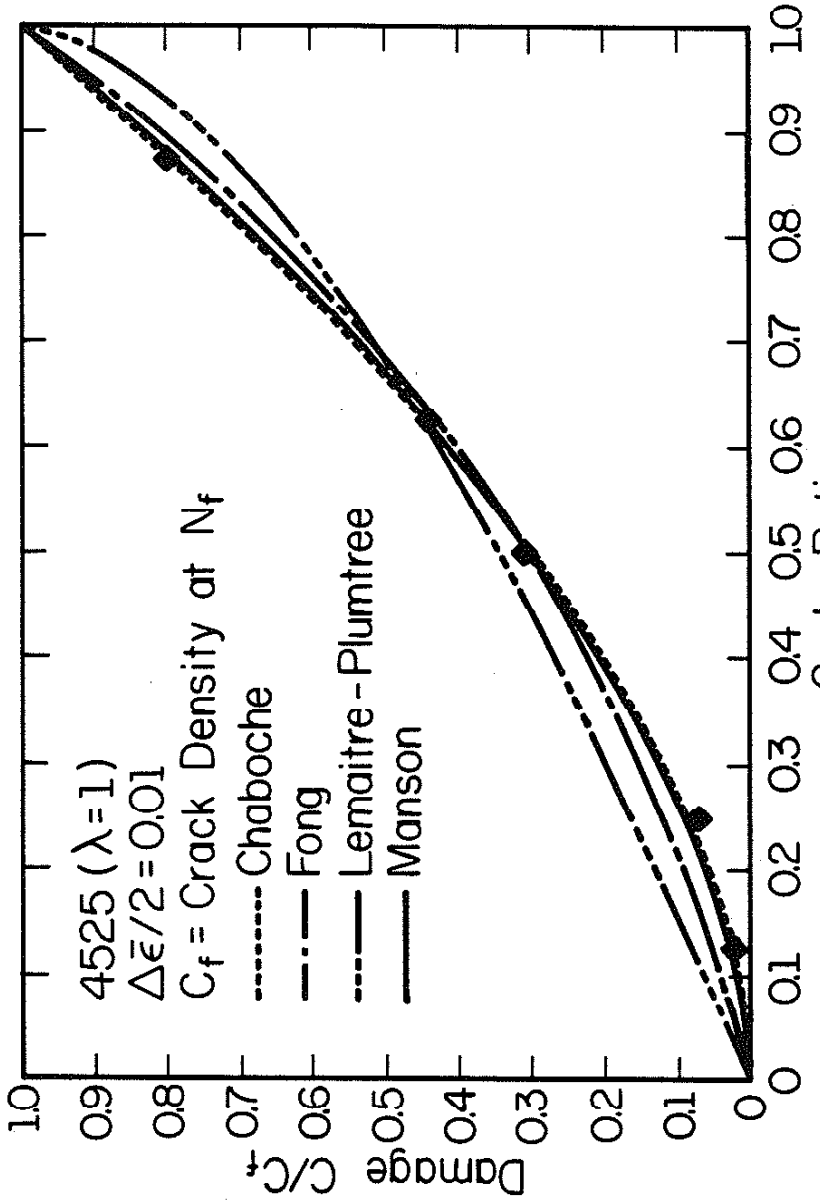

Figure 25 Comparison of damage models for Type-R crack system.

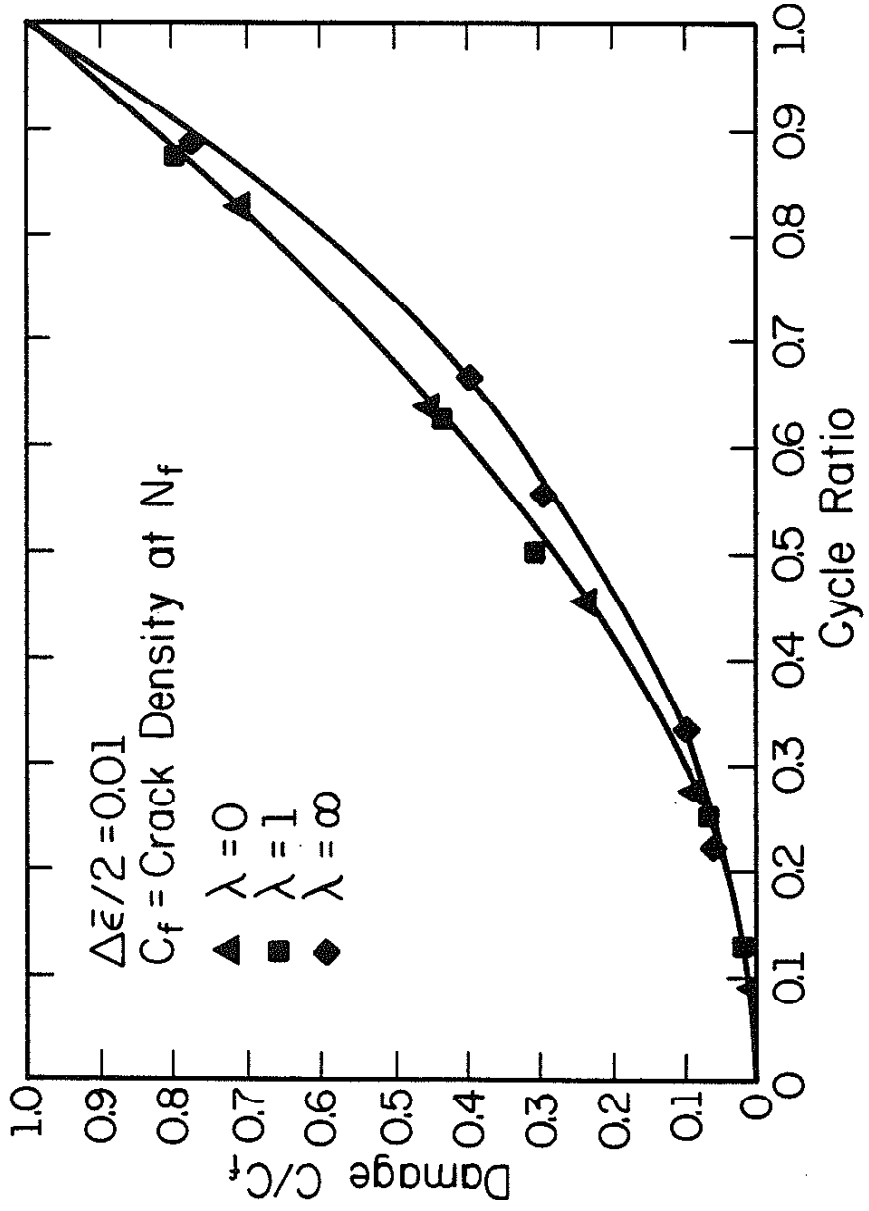

Figure 26 Damage curves for Type-R crack system under different loading modes.

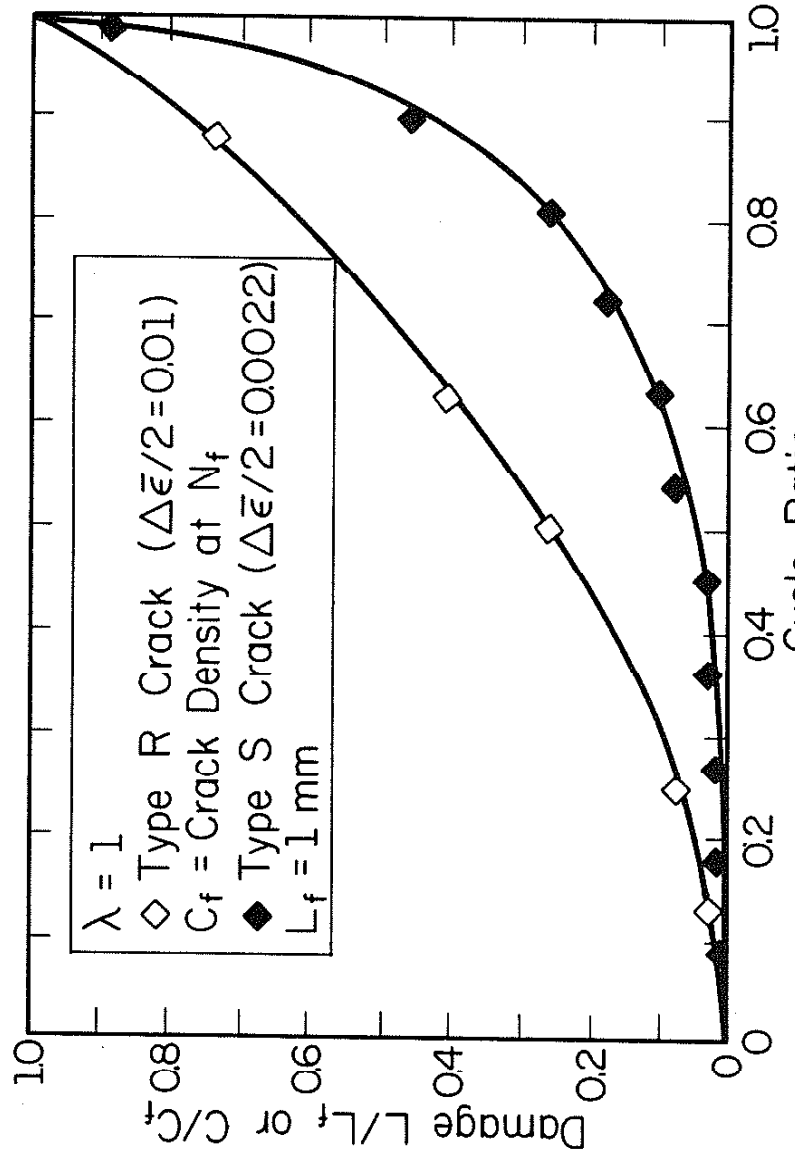

Figure 27 Comparison of damage curves under different crack systems, λ = 1.

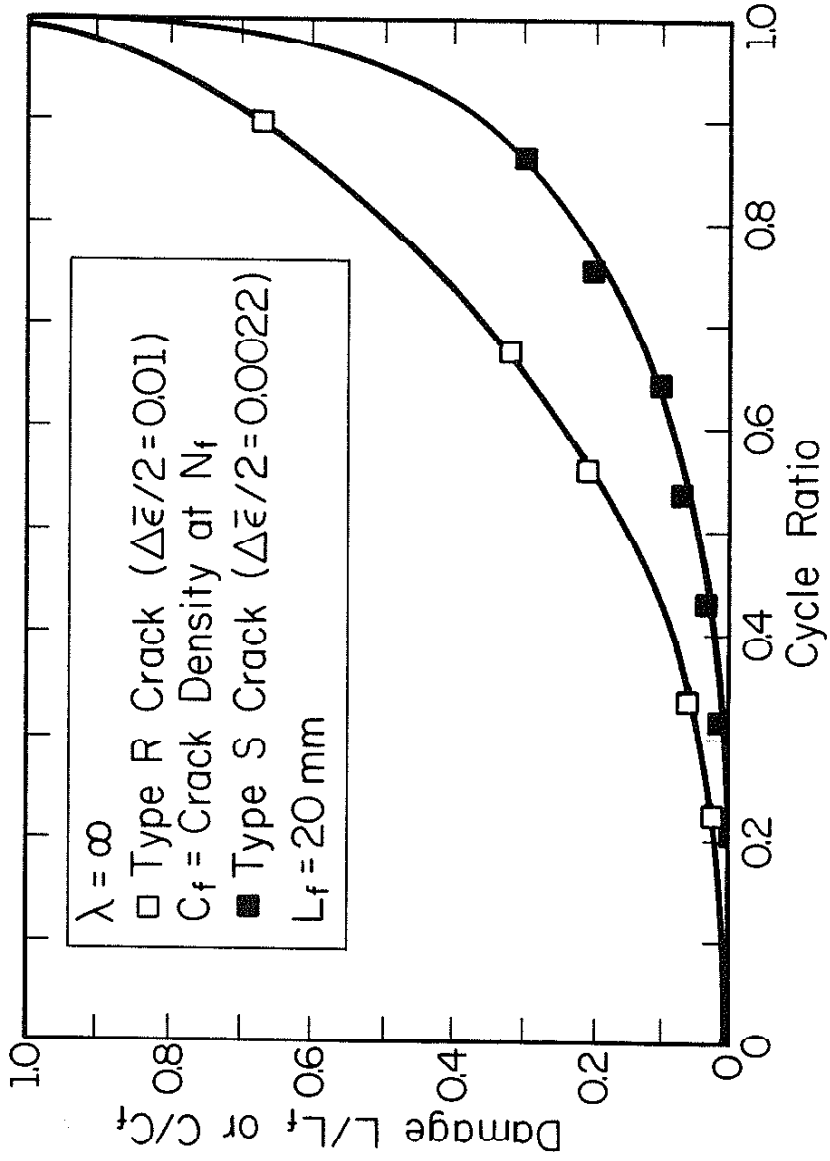

Figure 28 Comparison of damage curves under different crack systems, $\lambda = \infty$.

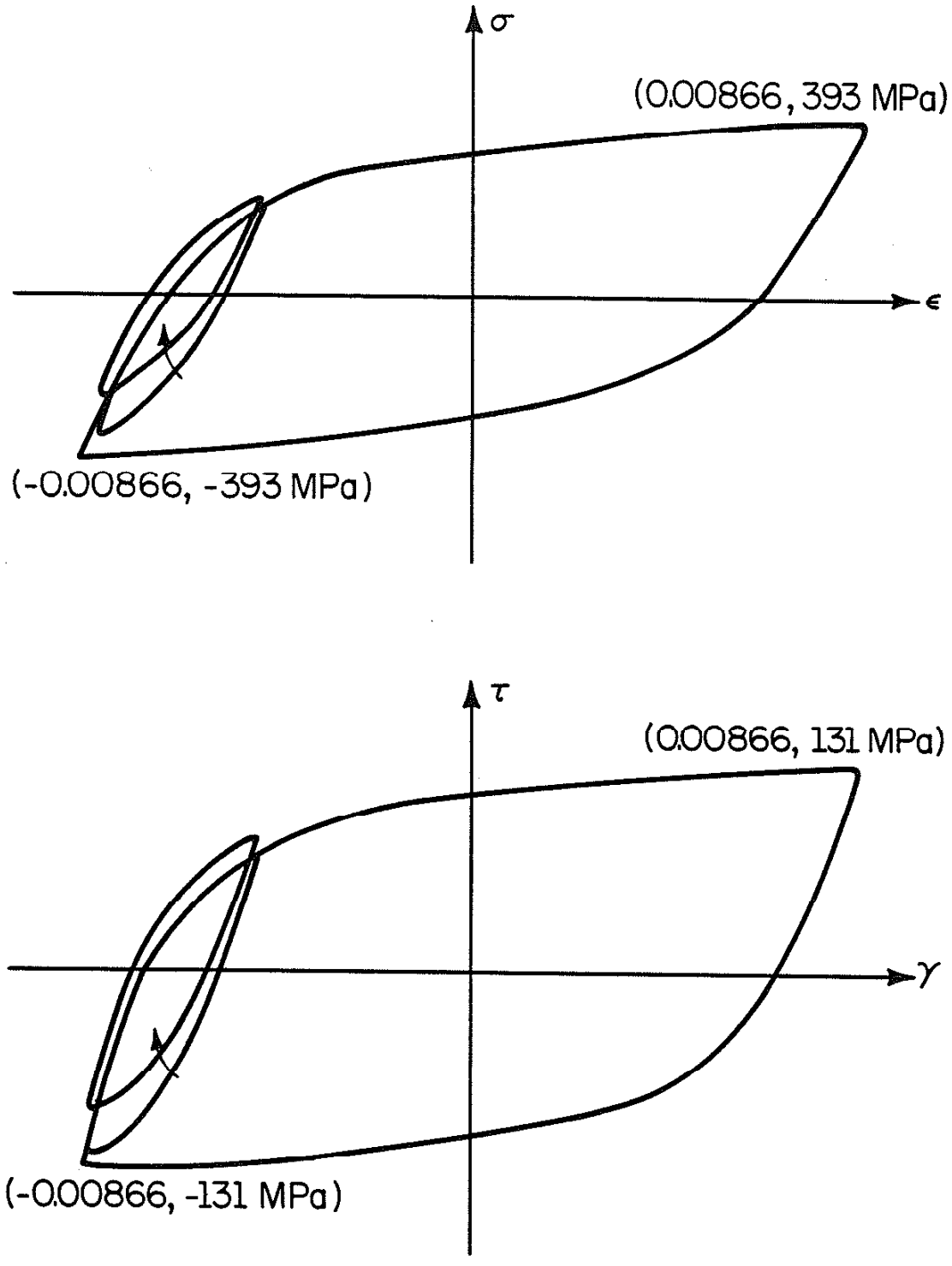

Figure 29 Hysteresis loops for variable loading, $\lambda = 1$.

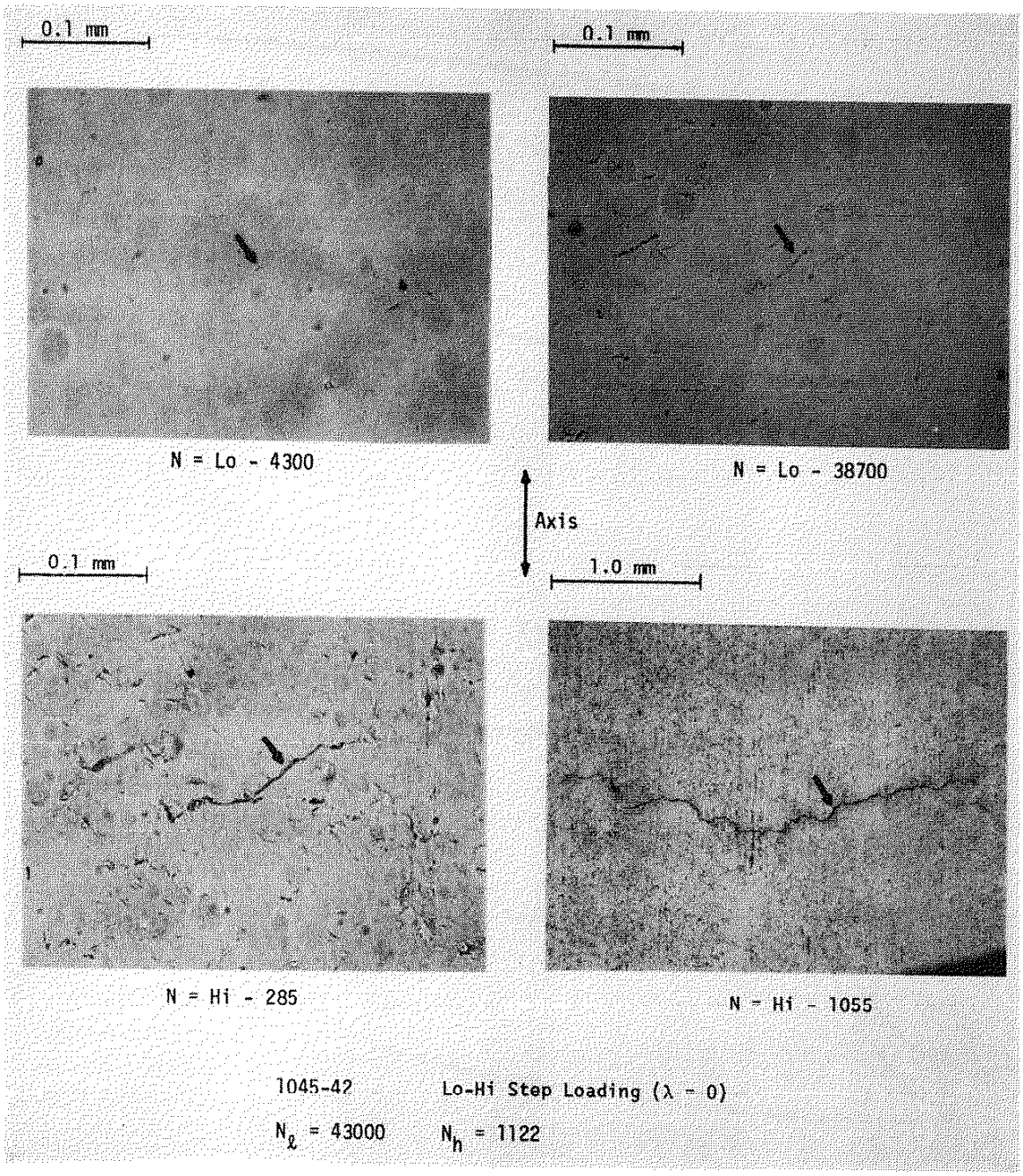

Figure 30 Type-S crack growth under step loading, $\lambda = 0$.

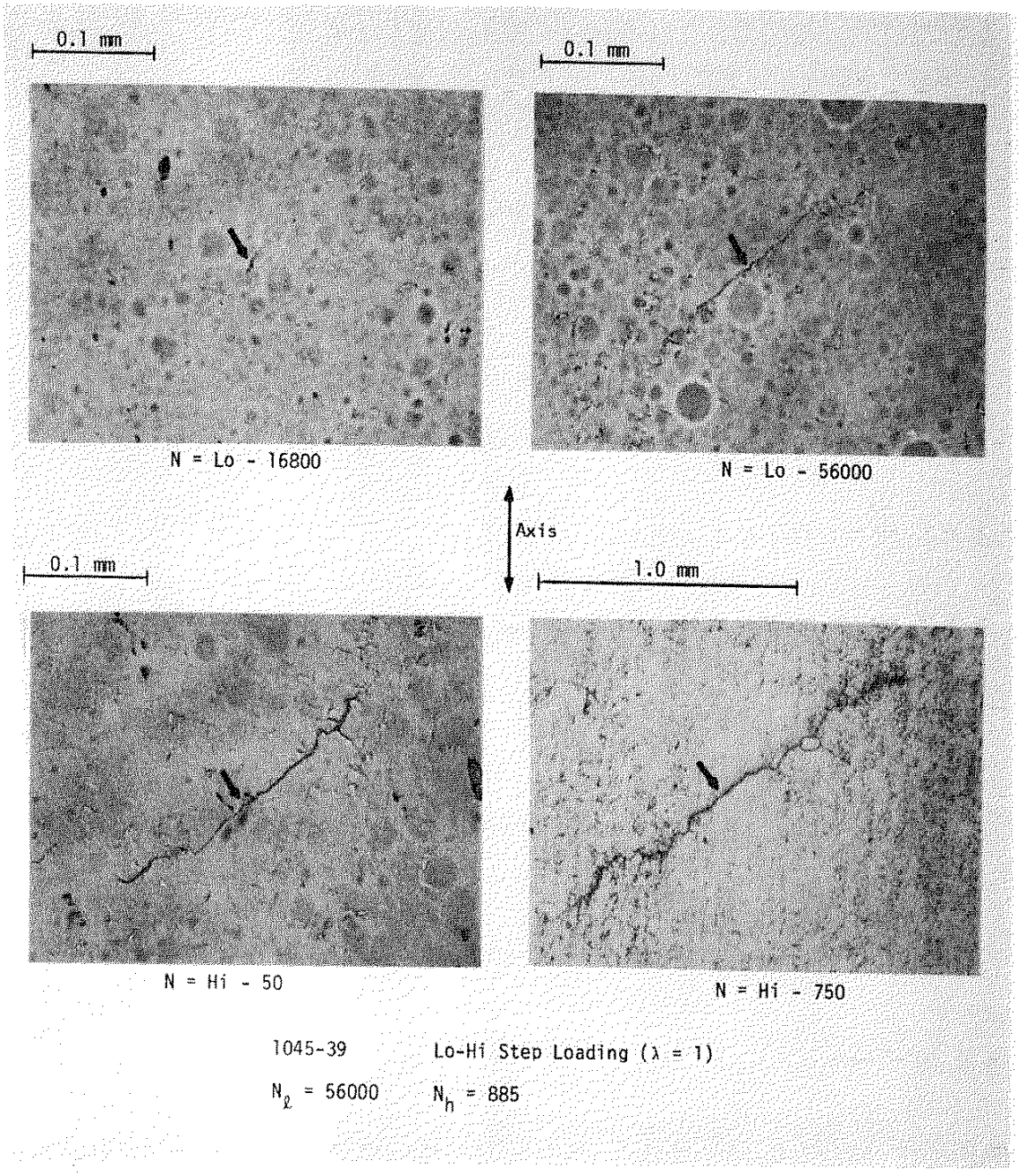

Figure 31 Type-S crack growth under step loading, $\lambda = 1$.

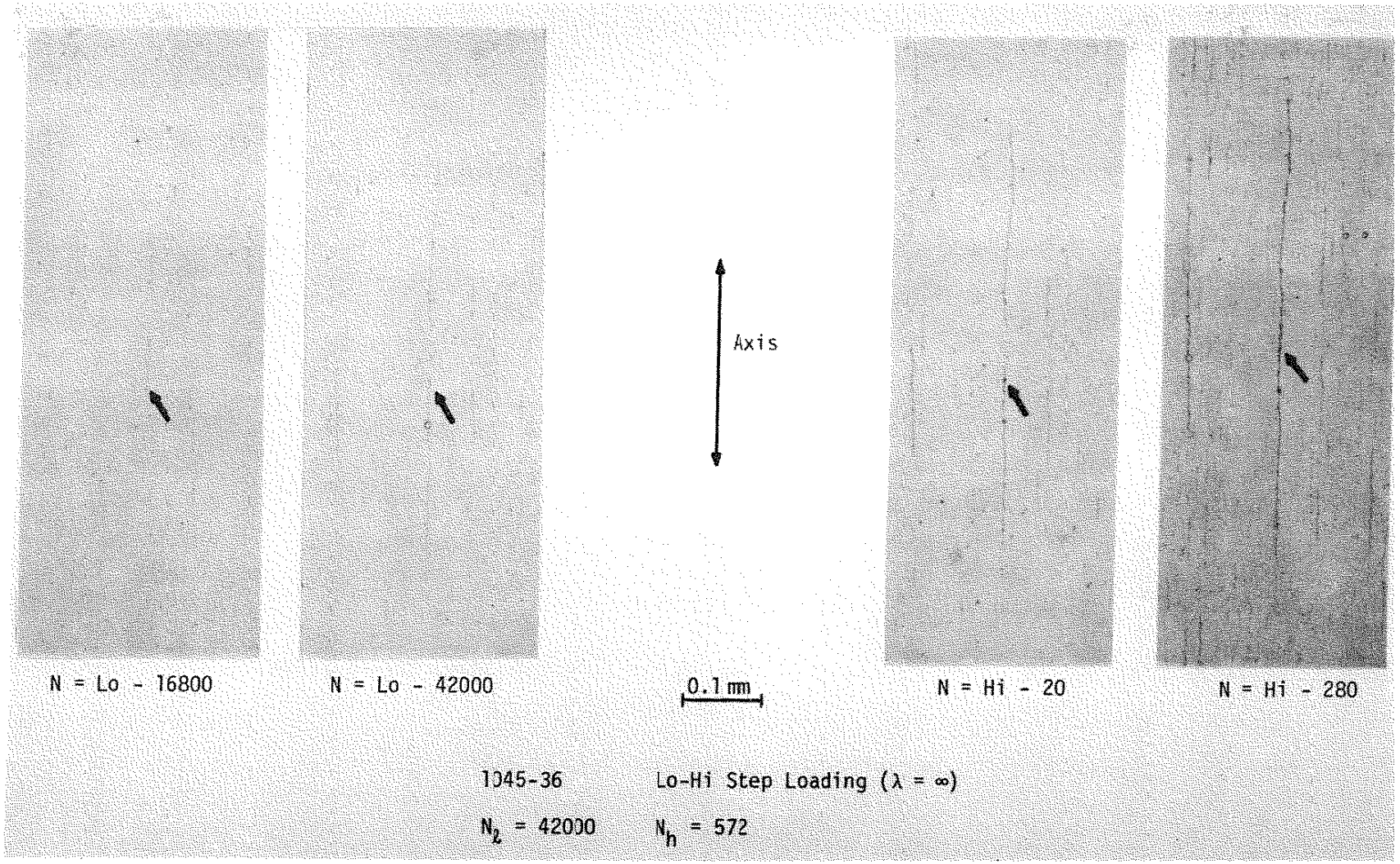

Figure 32 Type-S crack growth under step loading, $\lambda = \infty$.

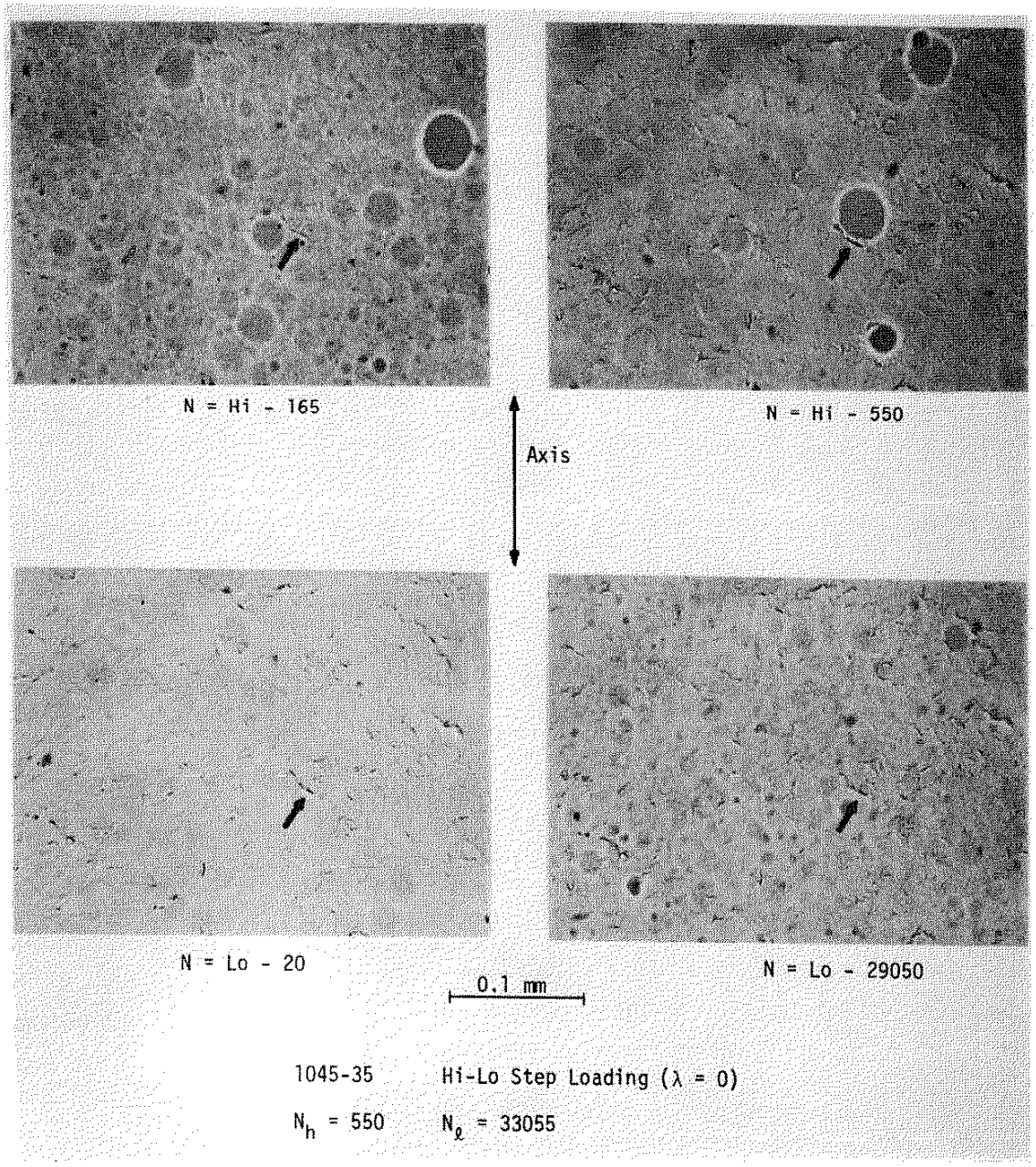

Figure 33 Type-R crack growth under step loading, $\lambda = 0$.

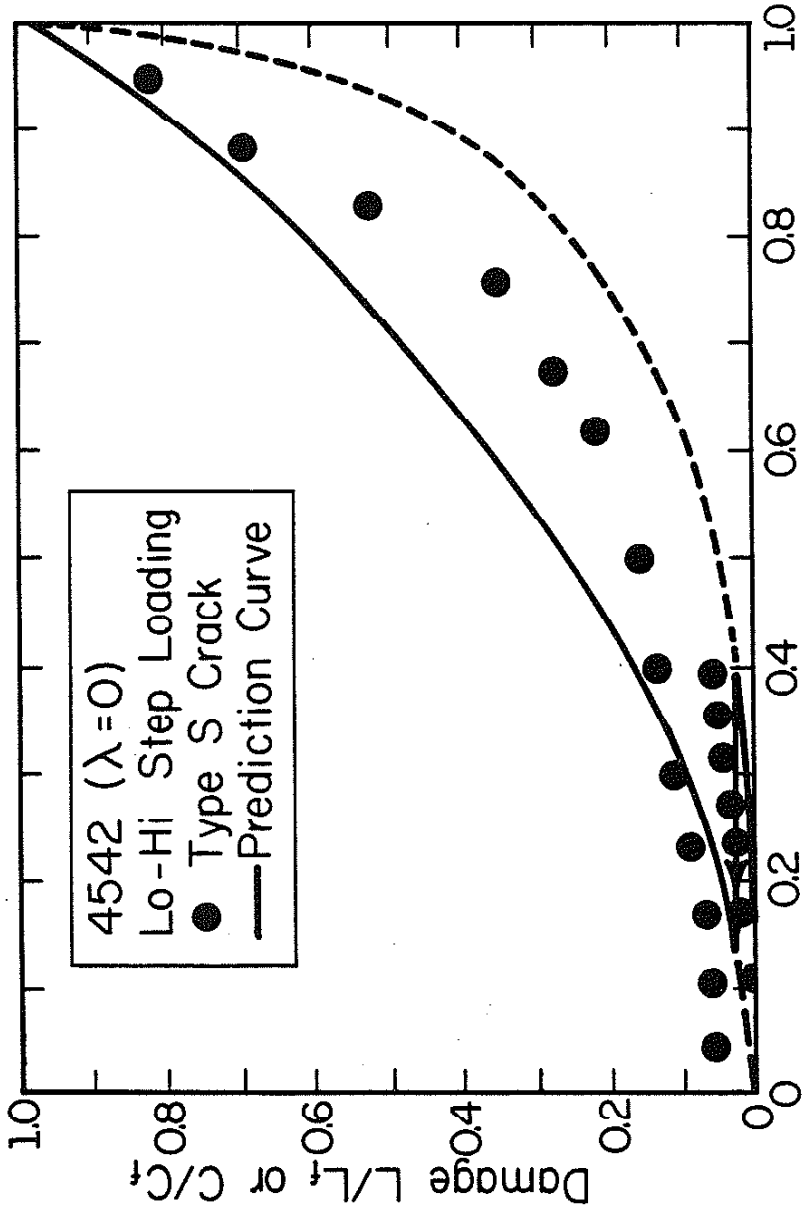

Figure 36 Actual damage development versus predicted damage development, $\lambda = 0$.

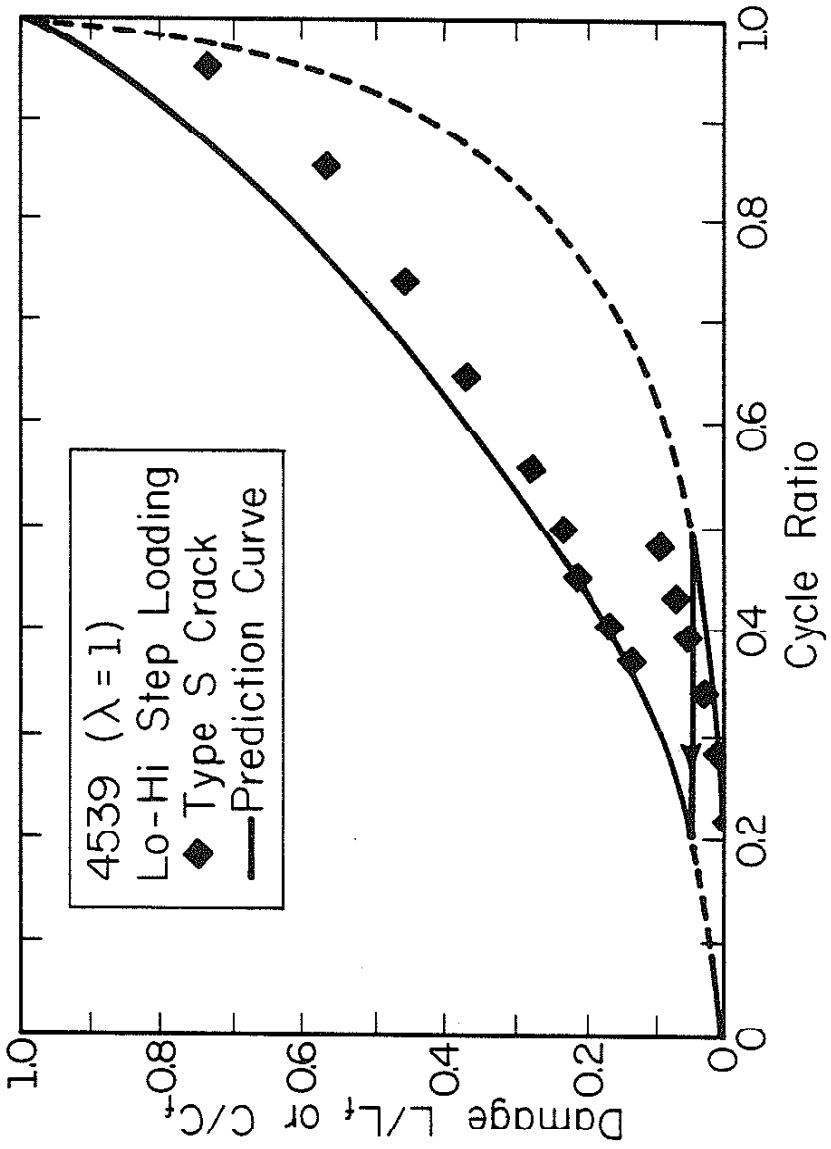

Figure 37 Actual damage development versus predicted damage development, $\lambda = 1$.

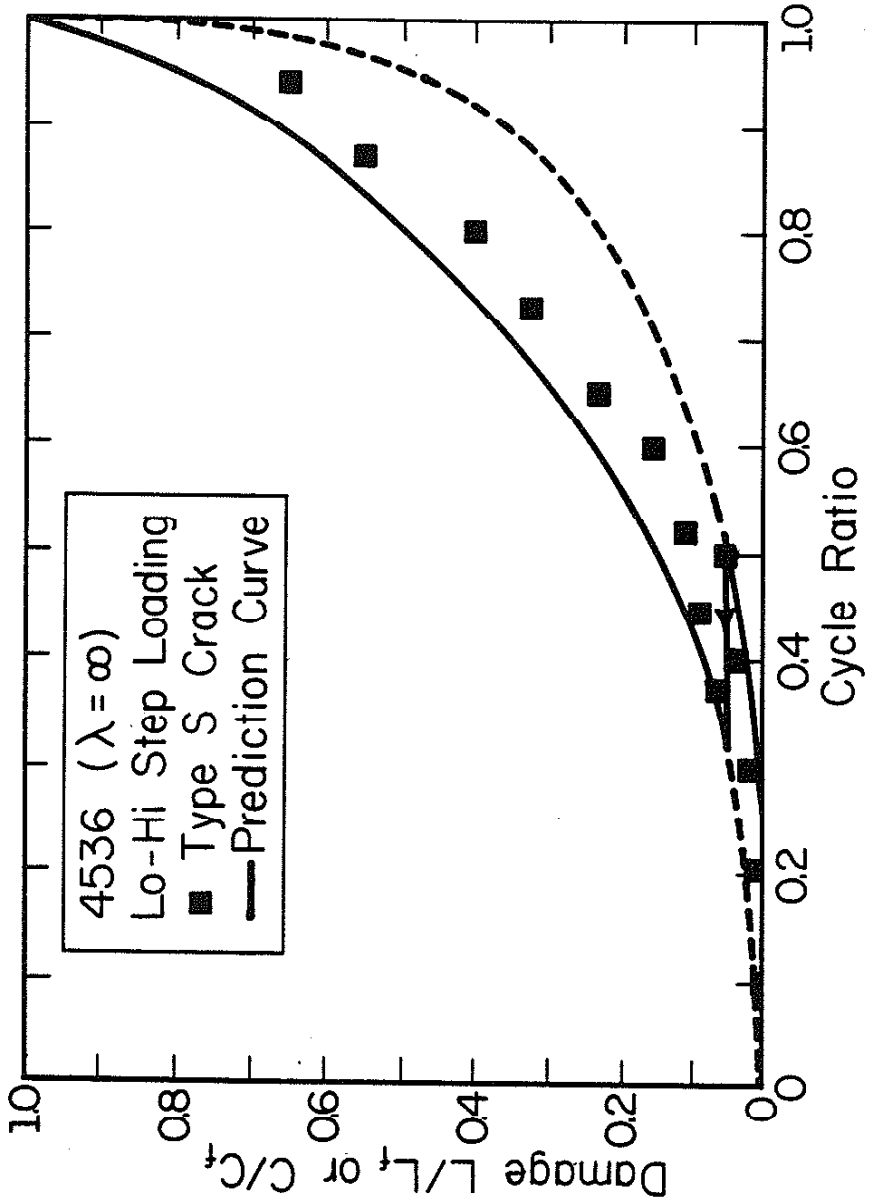

Figure 38 Actual damage development versus predicted damage development, $\lambda = \infty$.

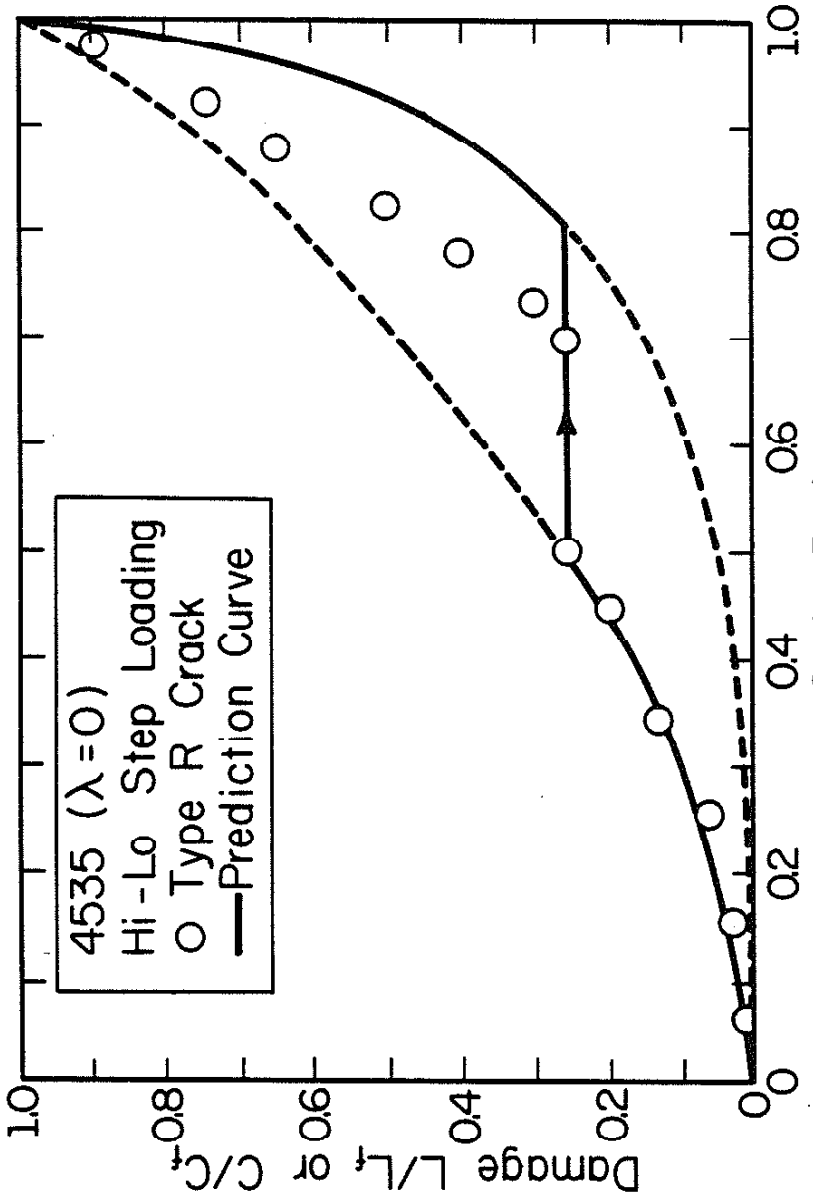

Figure 39 Actual damage development versus predicted damage development, $\lambda = 0$.

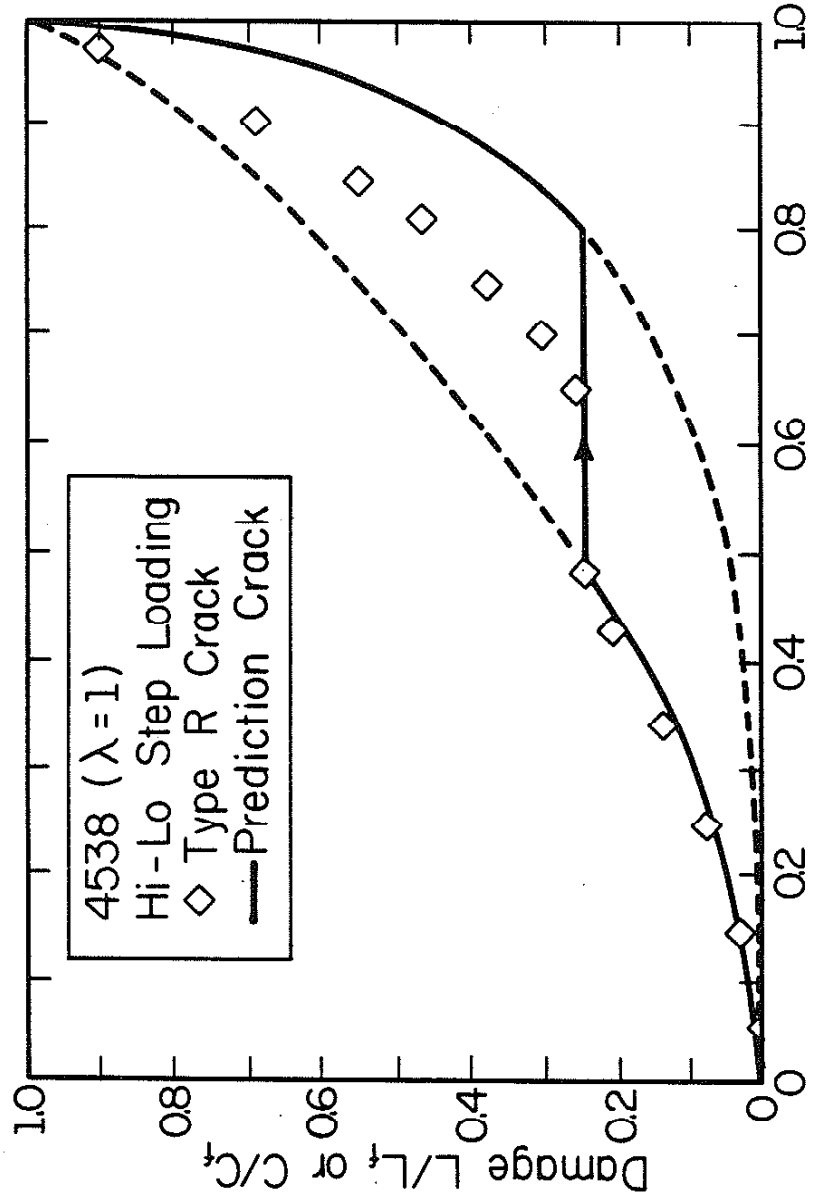

Figure 40 Actual damage development versus predicted damage development, $\lambda = 1$.

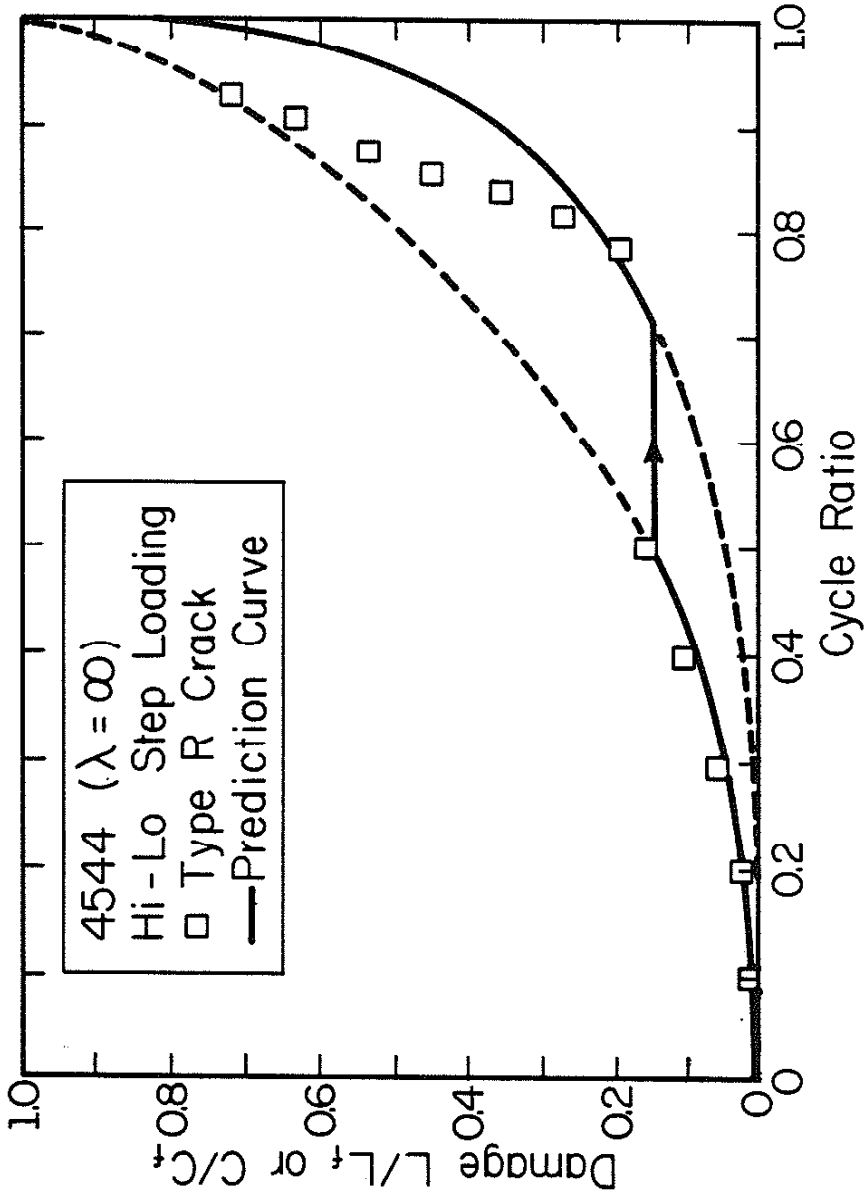

Figure 41 Actual damage development versus predicted damage development, $\lambda = \infty$.

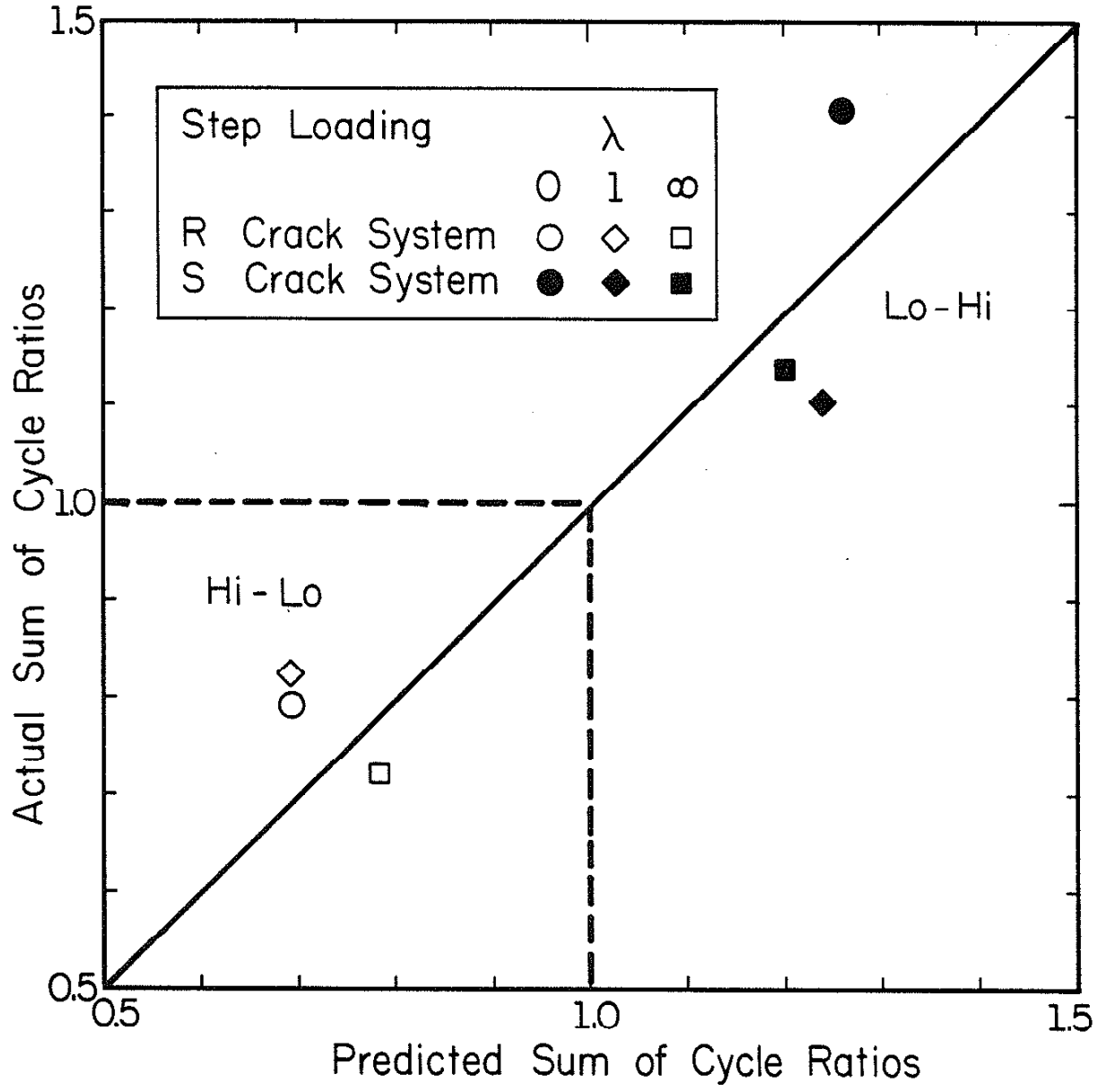

Figure 42 Actual lives versus predicted lives under step loading.

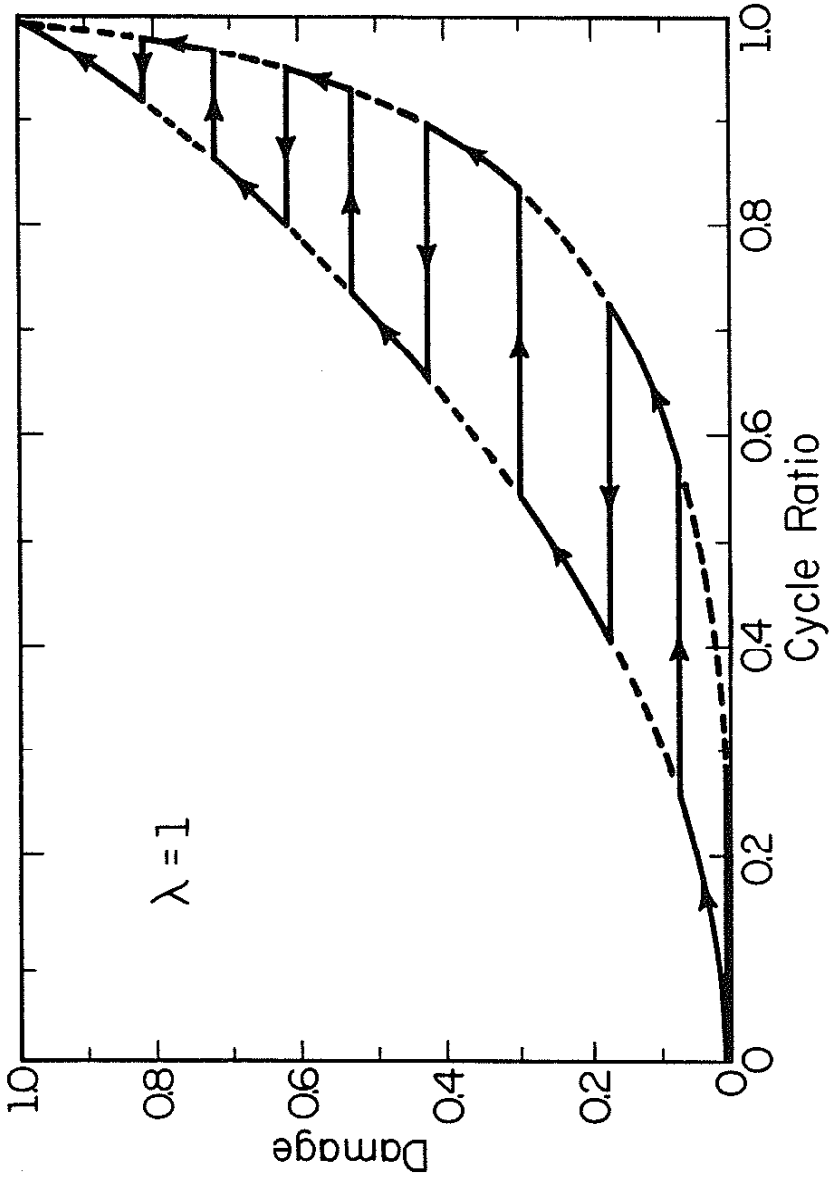

Figure 43 Simulation of block loading.

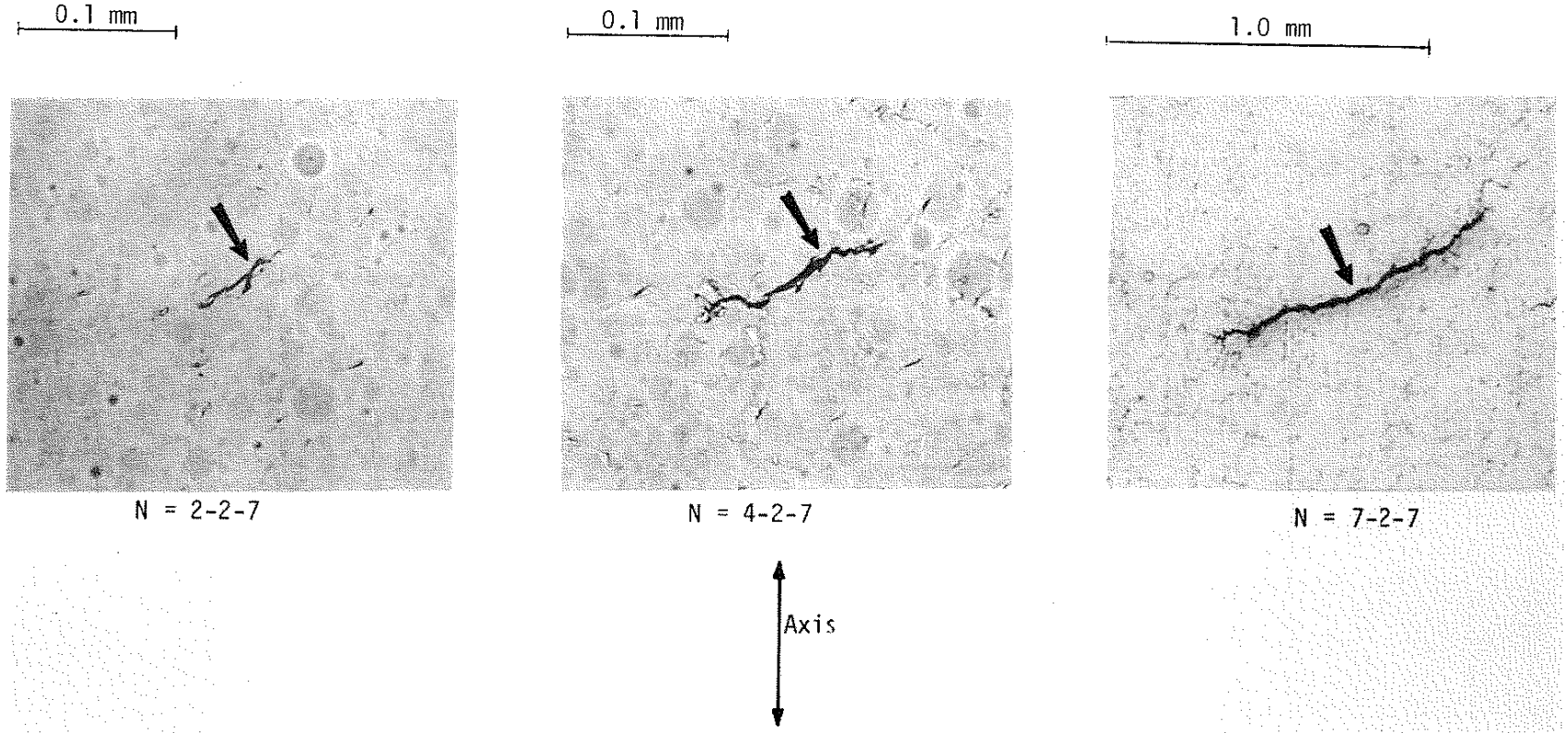

Figure 44 Type-S crack growth under block loading.

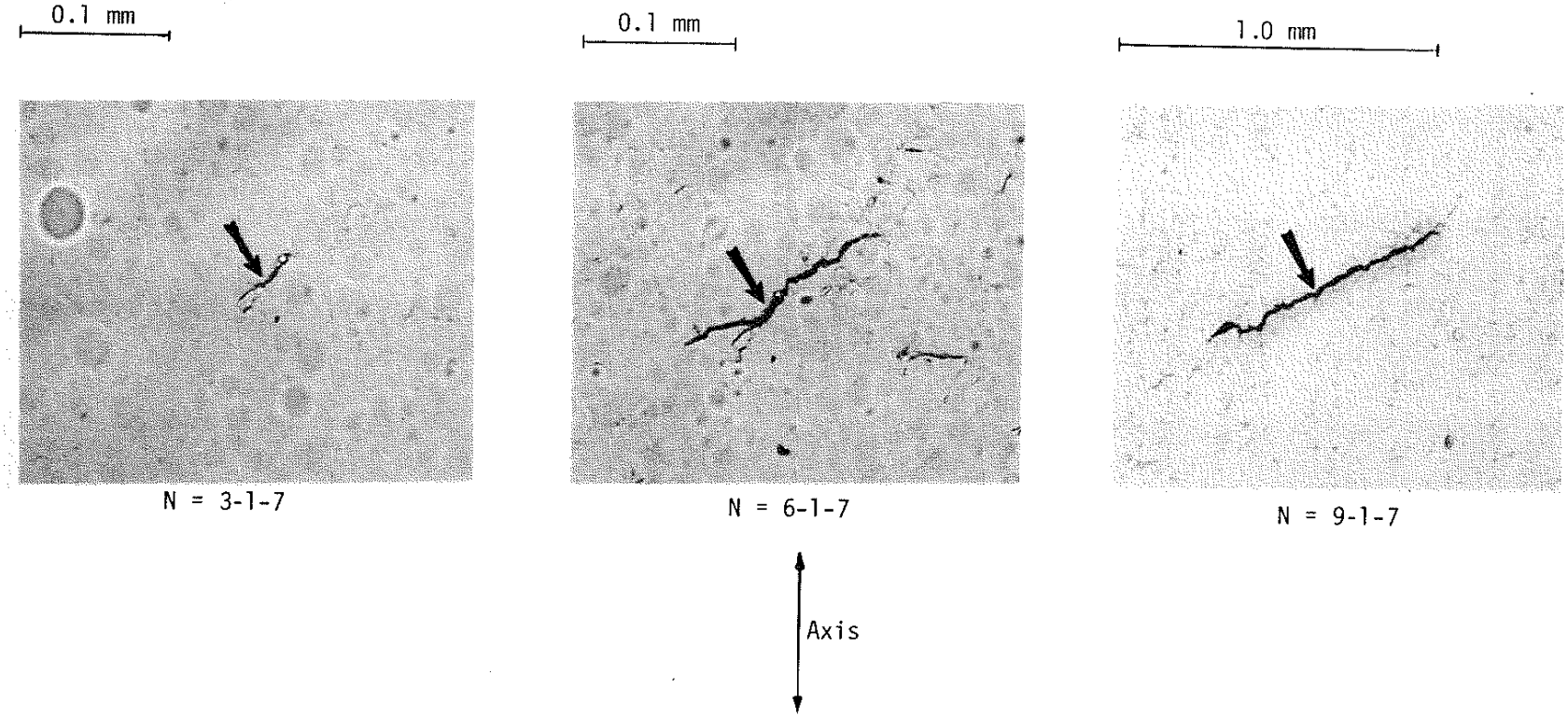

1045-62 Hi-Lo Block Loading (λ = 1)

Relative Cycle Ratio = 19

Failure Cycle Number = 9-2-10640

Figure 45 Type-S crack growth under block loading.

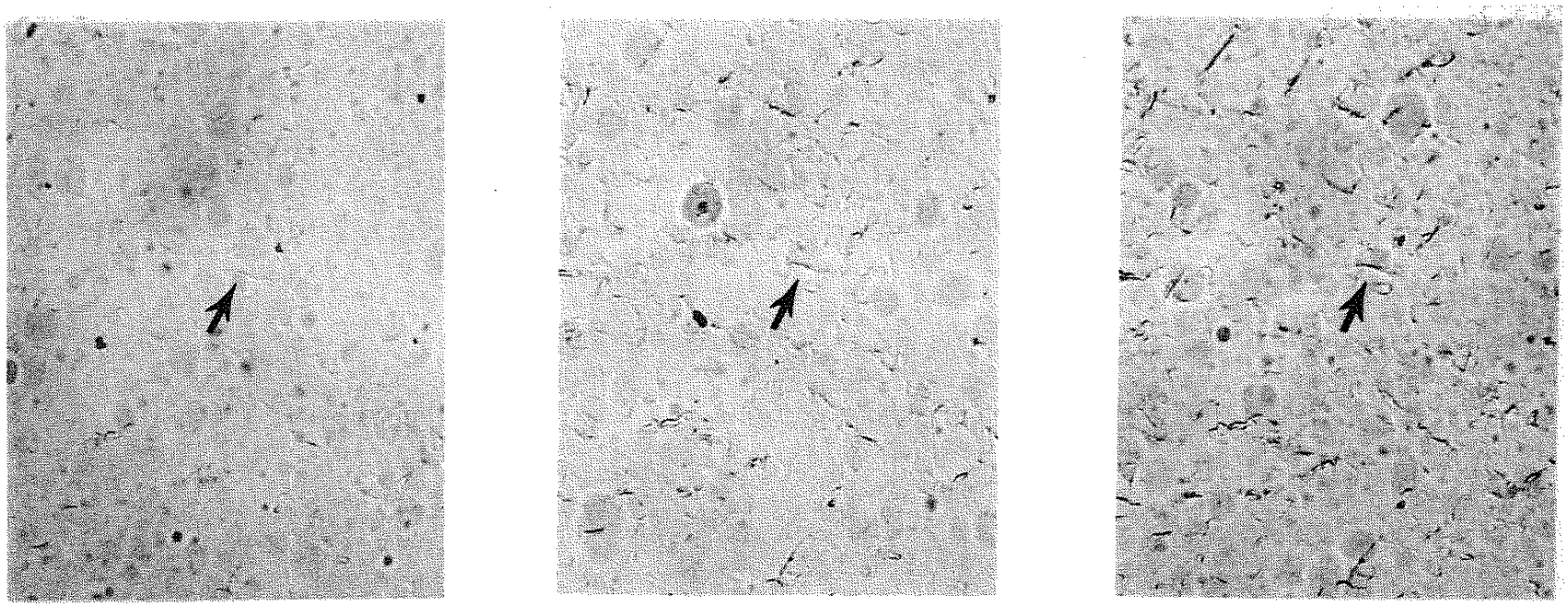

1045-64 Hi-Lo Block Loading (λ = 1)

Relative Cycle Ratio = 1

Failure Cycle Number = 7-2-5600

Figure 46 Type-R crack growth under block loading.

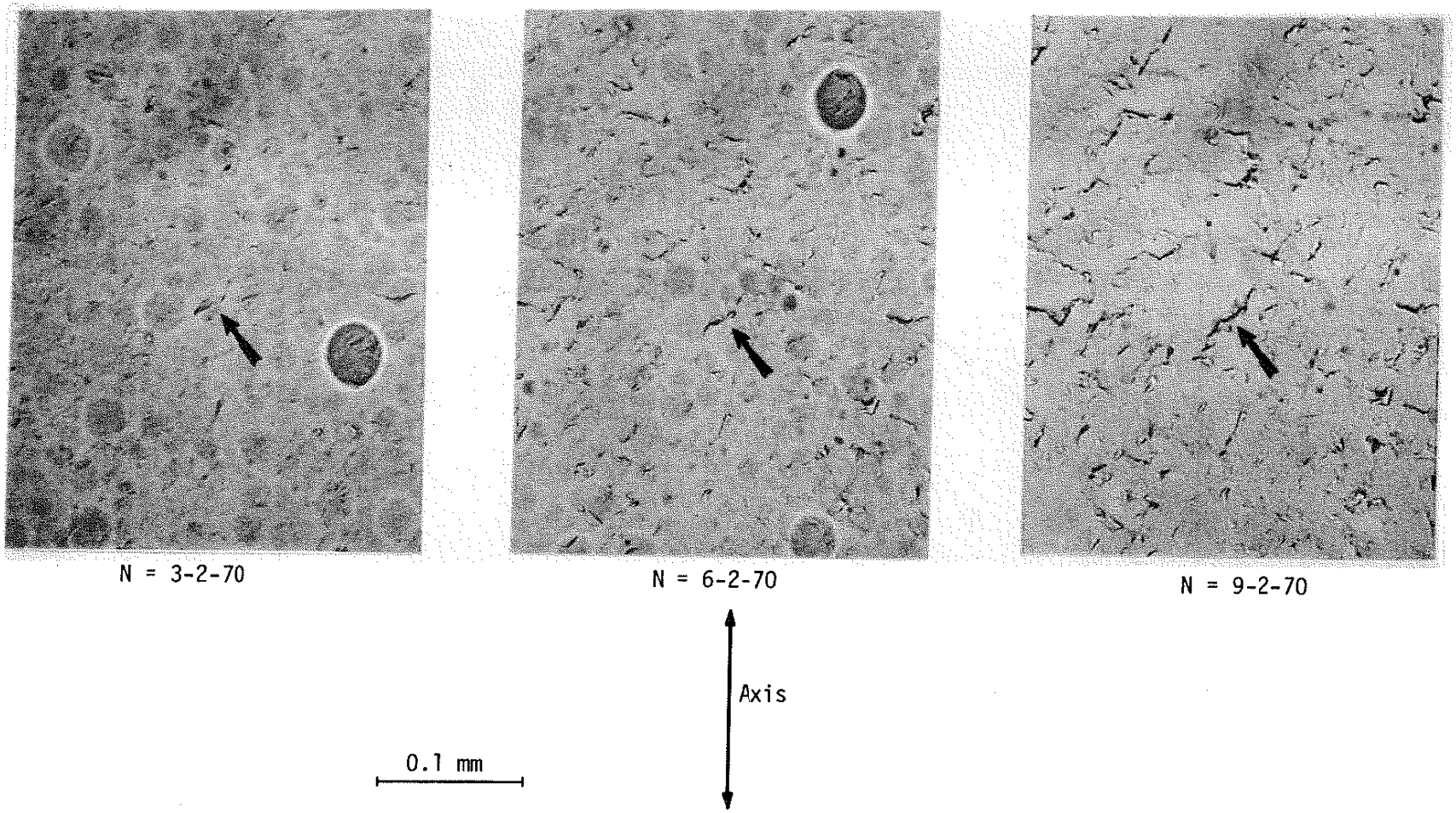

Figure 47 Type-R crack growth under block loading.

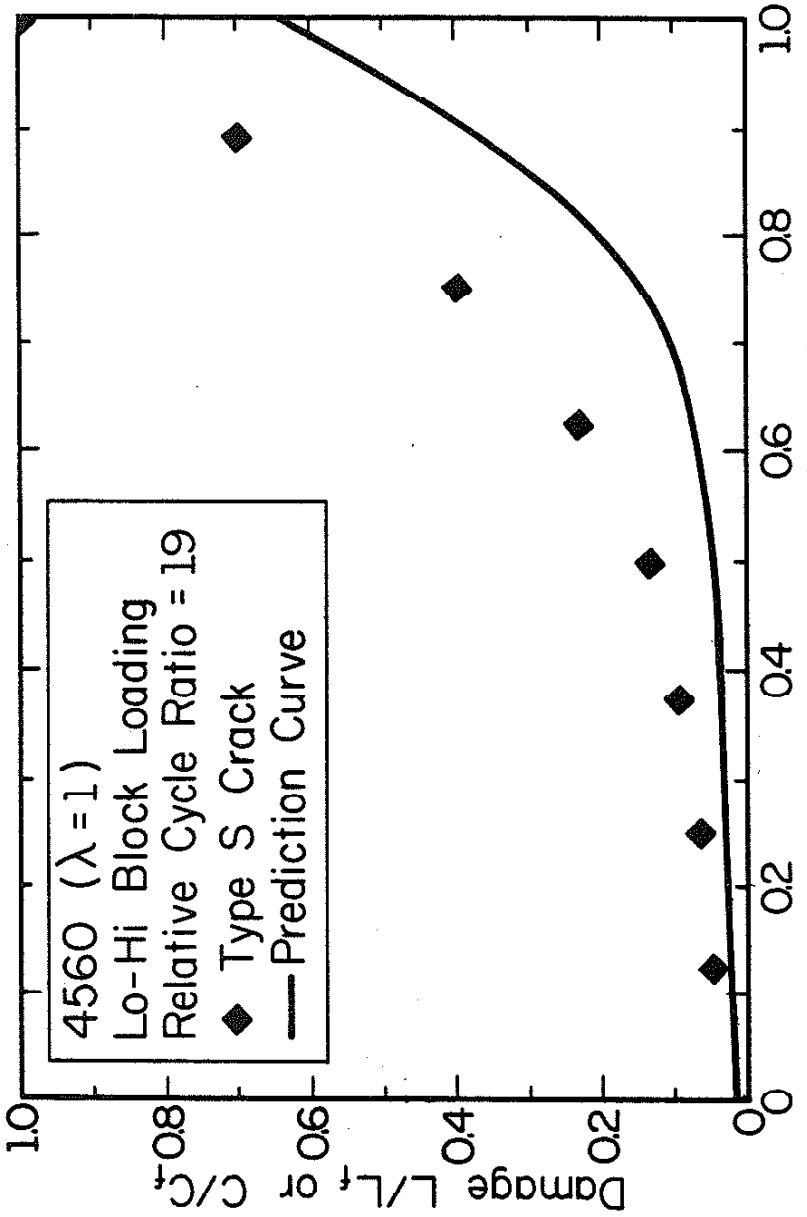

Figure 48 Actual damage curve versus predicted damage curve.

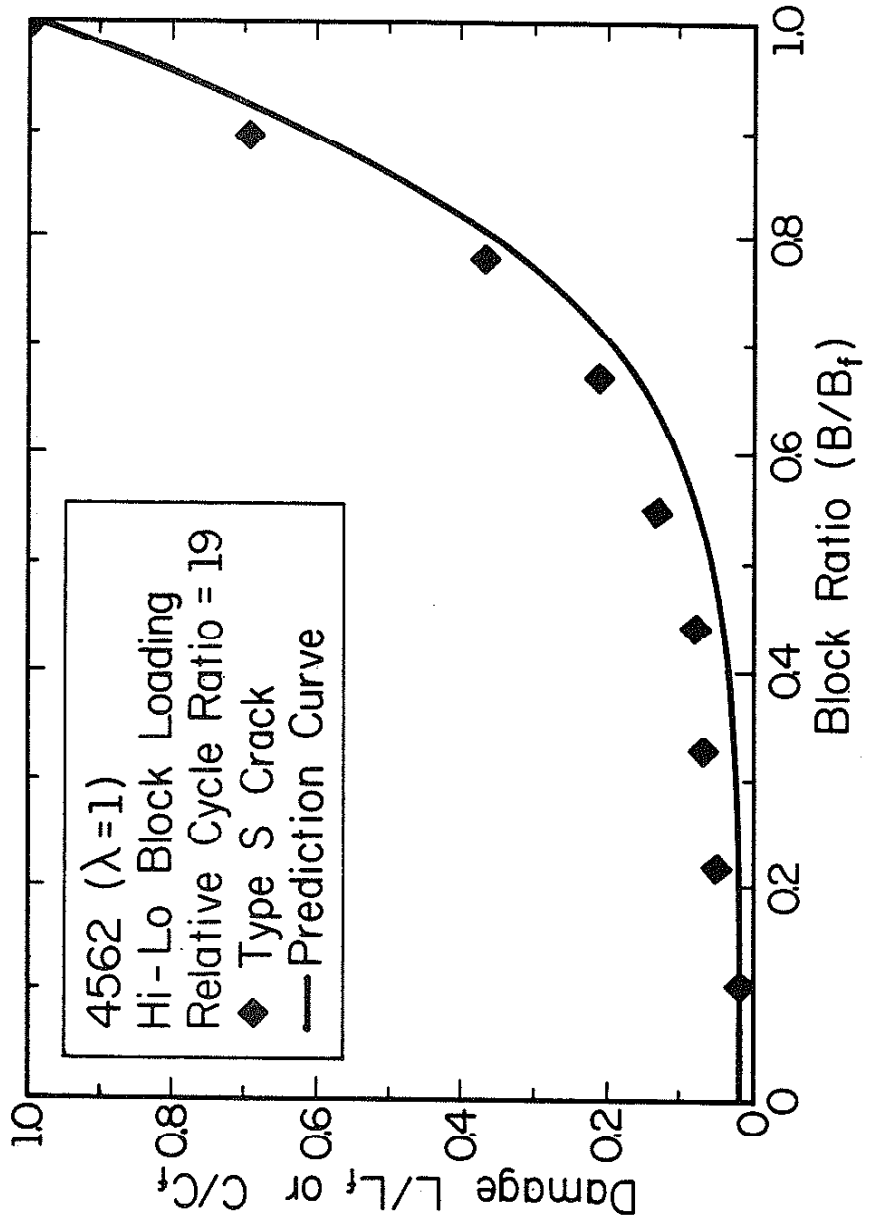

Figure 49 Actual damage curve versus predicted damage curve.

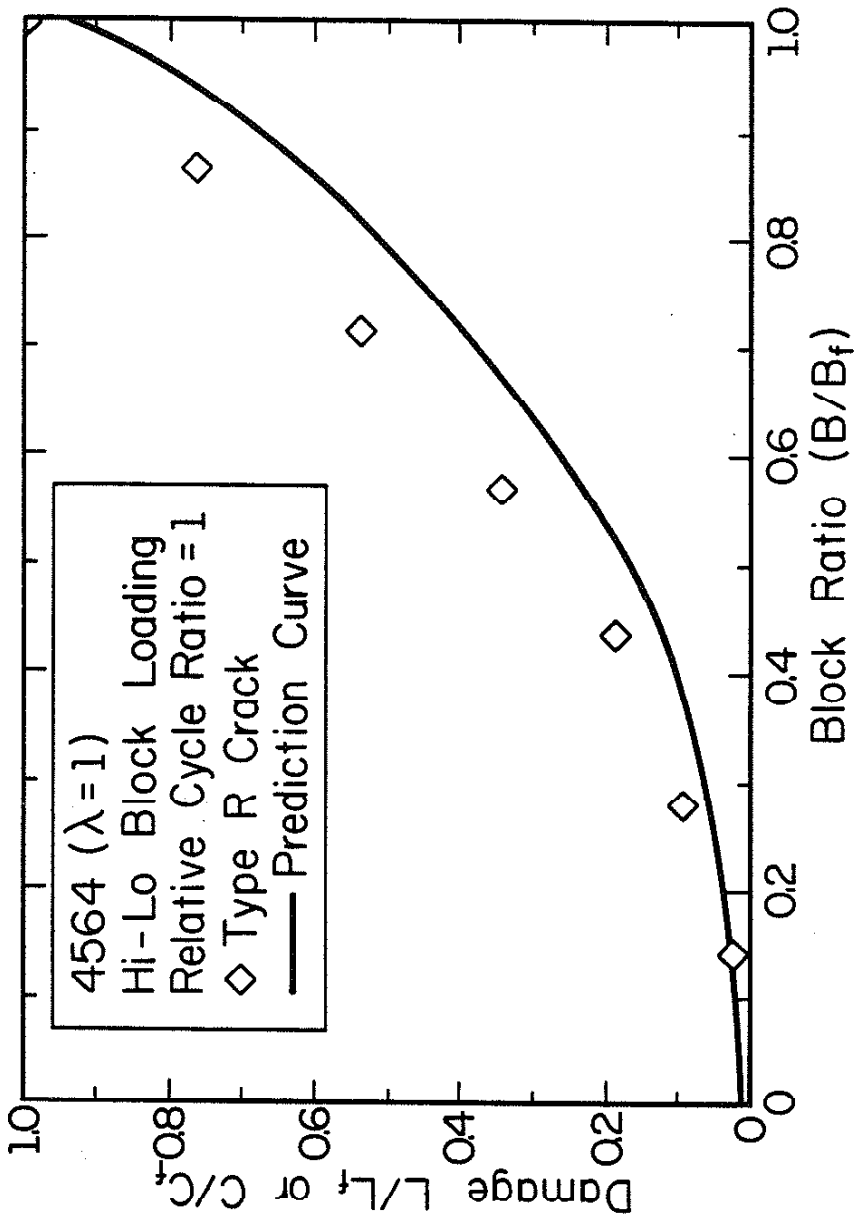

Figure 50 Actual damage curve versus predicted damage curve.

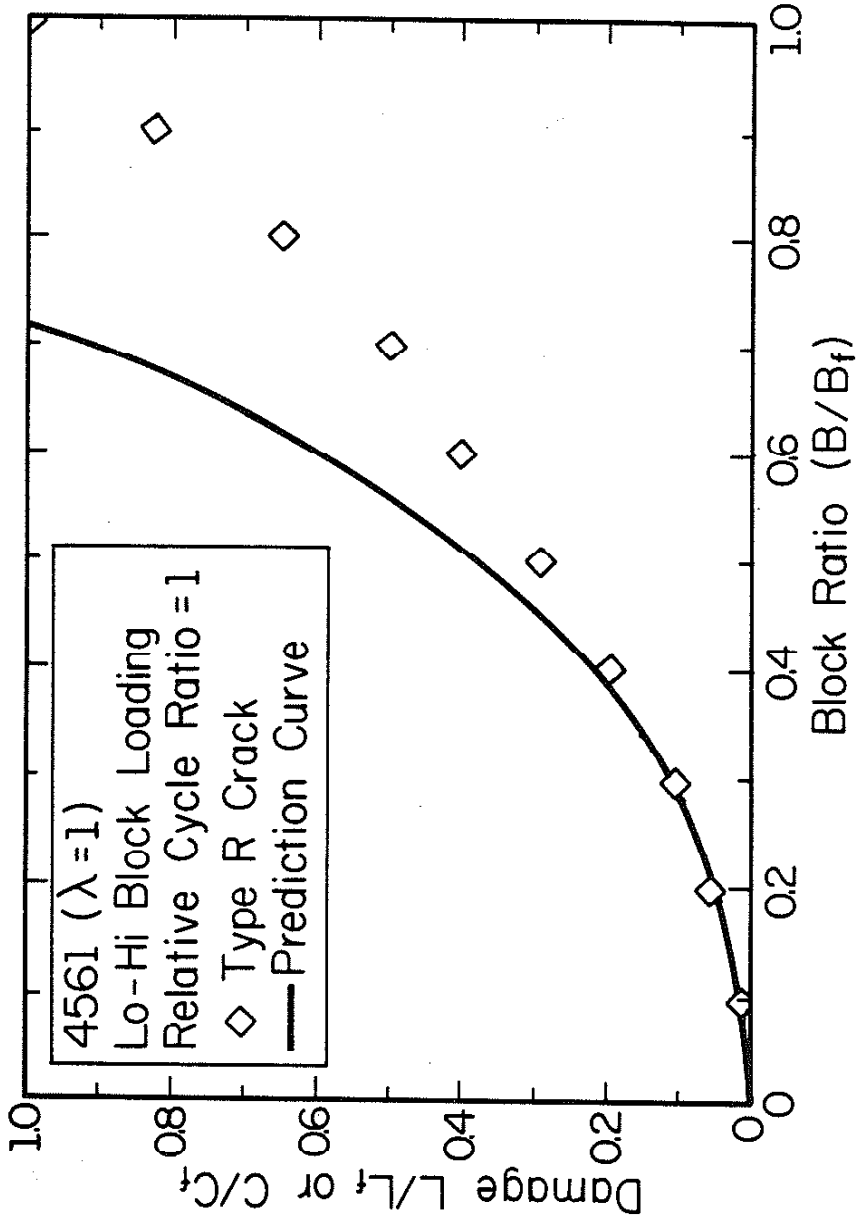

Figure 51 Actual damage curve versus predicted damage curve.

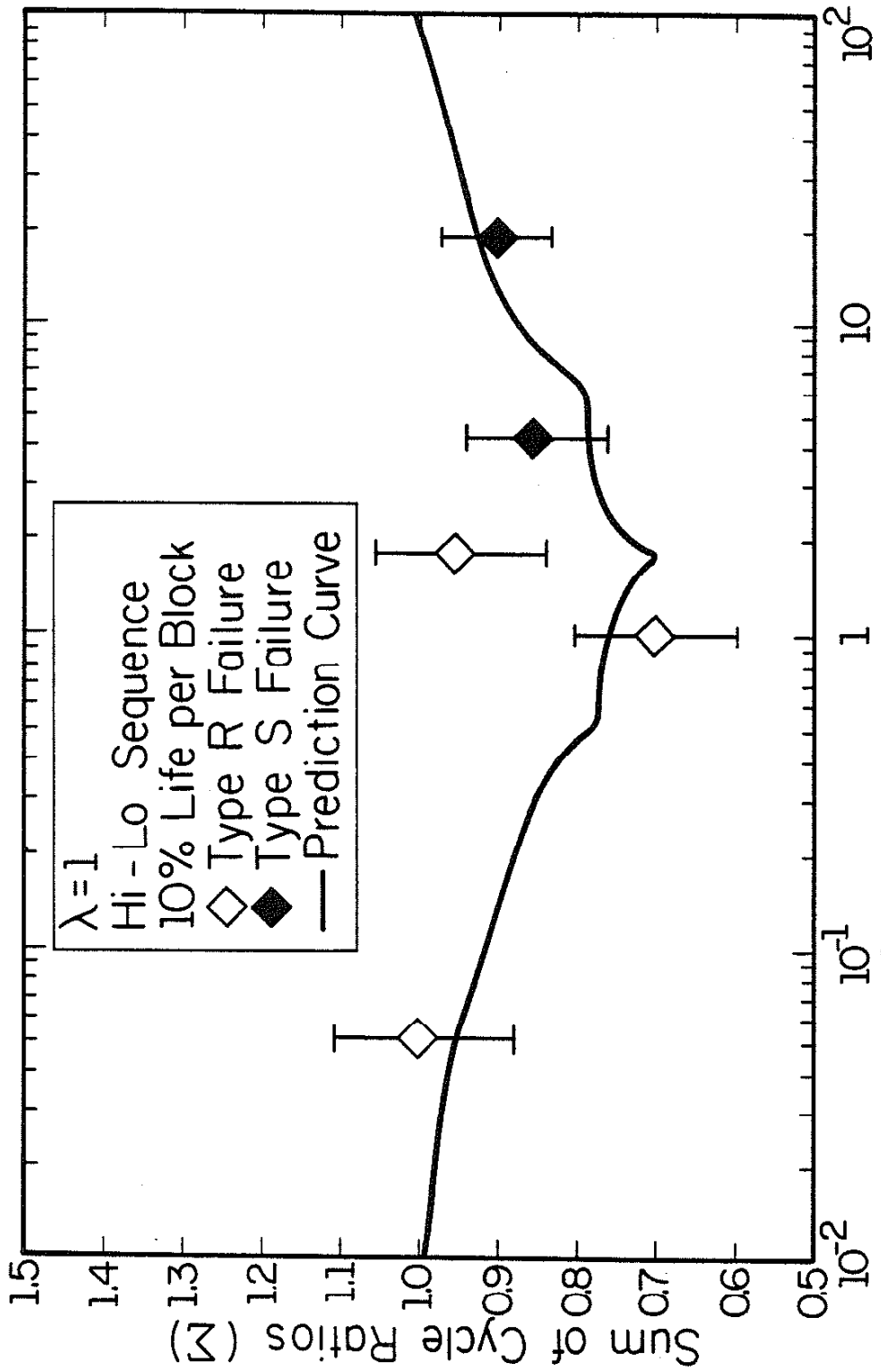

Figure 52 Actual lives versus predicted lives under block loading.

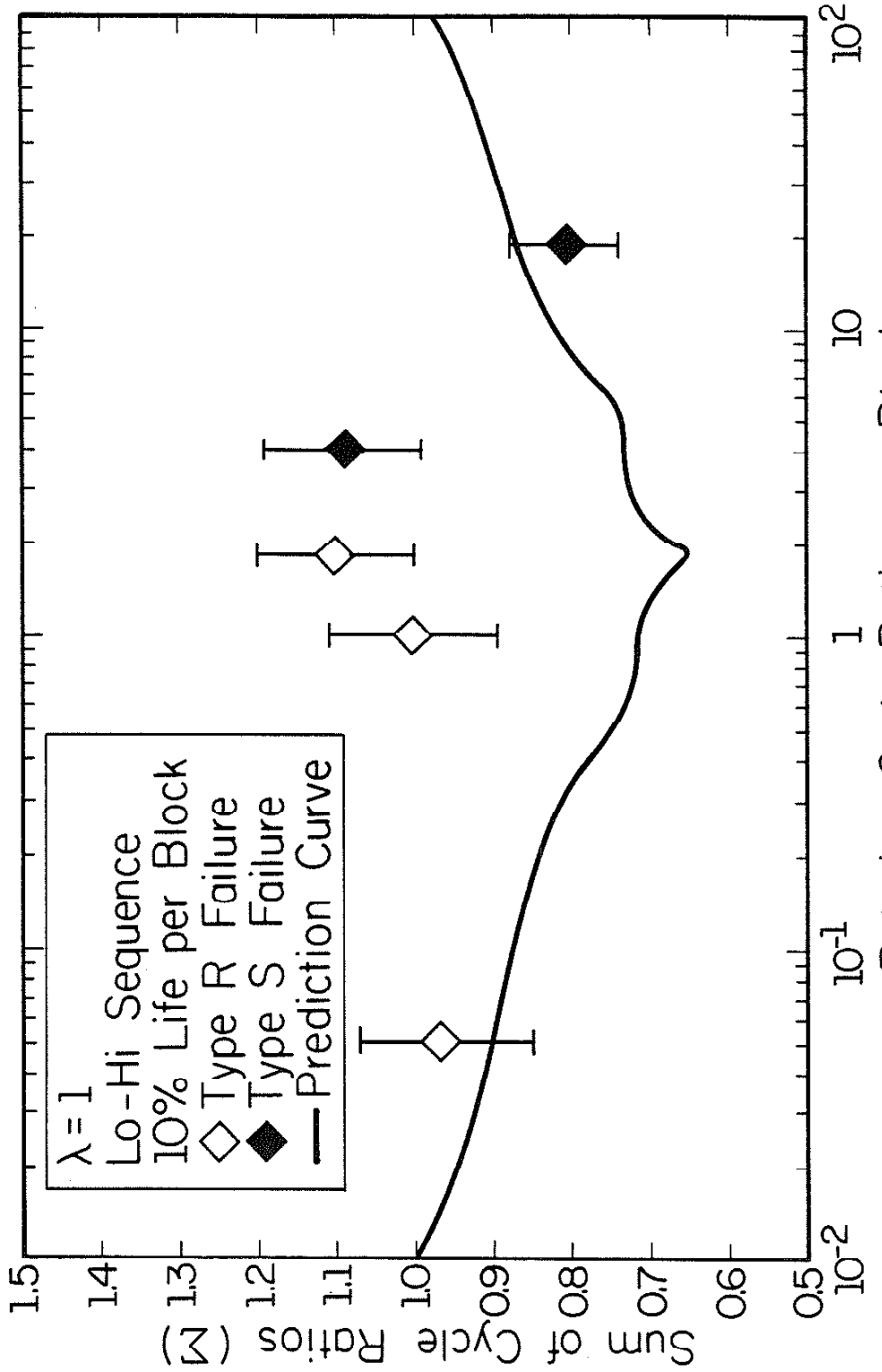

Figure 53 Actual lives versus predicted lives under block loading.

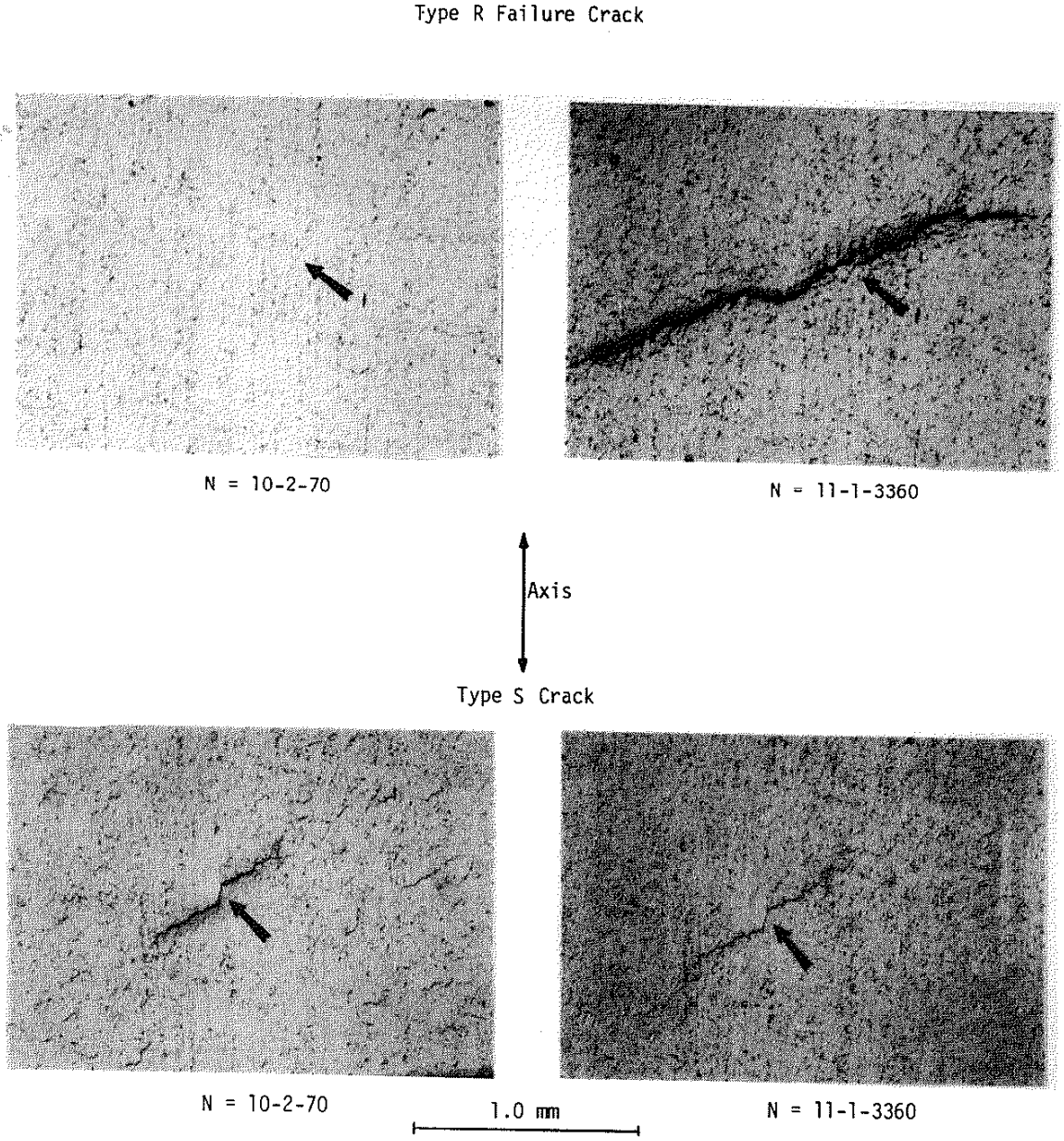

1045-61 Lo-Hi Block Loading (λ = 1)

Relative Cycle Ratio = 1

Failure Cycle Number = 11-1-3360

Figure 54 Different crack systems in a single specimen.

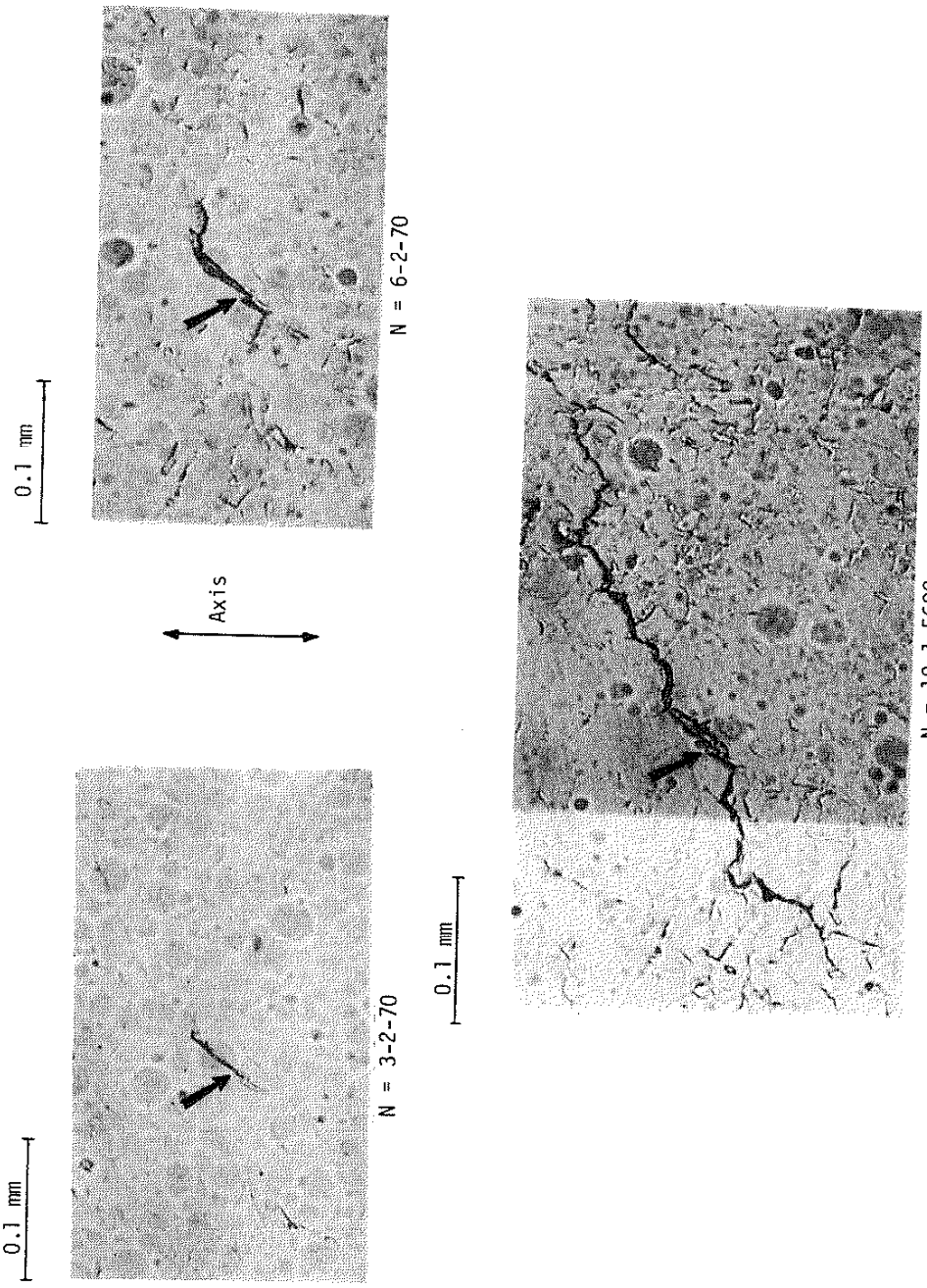

1045-61 Lo-Hi Block Loading (λ = 1)
Relative Cycle Ratio = 1
Failure Cycle Number = 11-1-3360

Figure 55 Type-S crack growth under block loading.

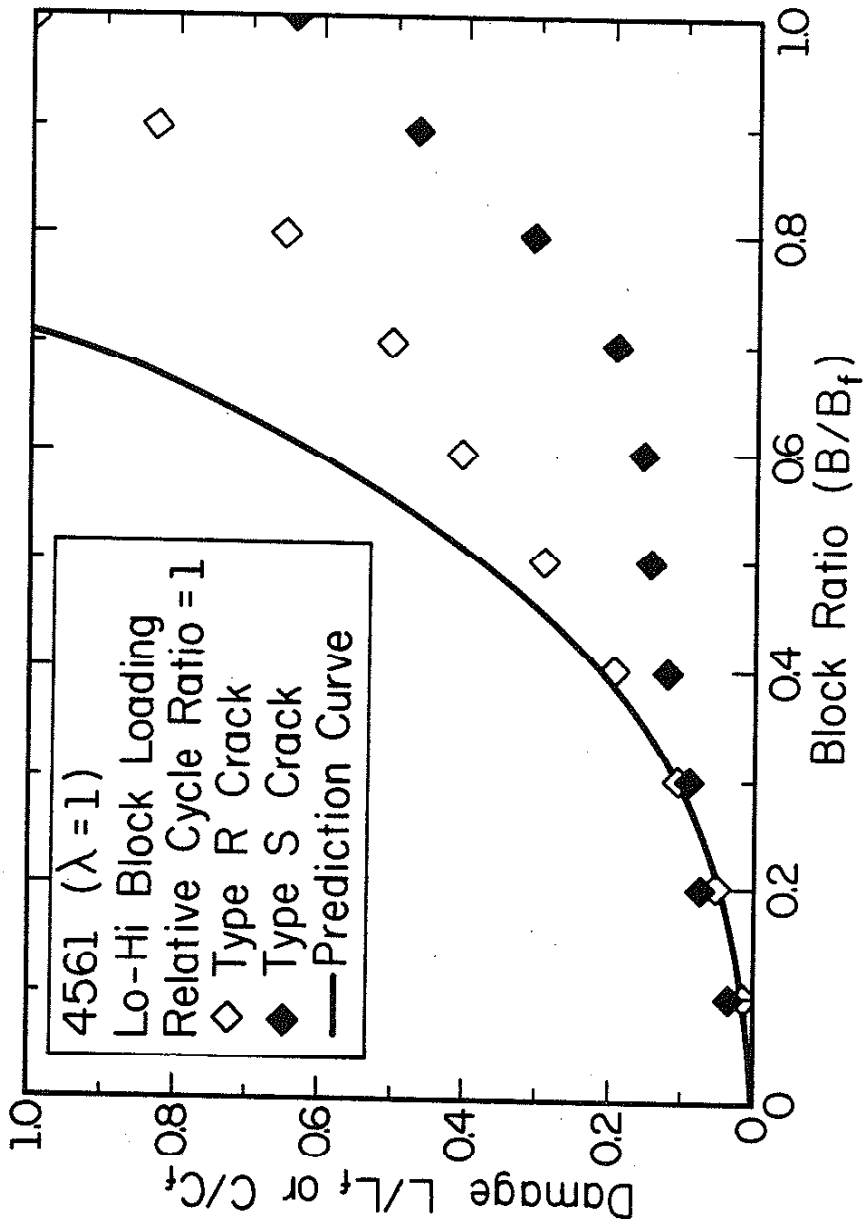

Figure 56 Comparison of damage development for different crack systems under block loading.

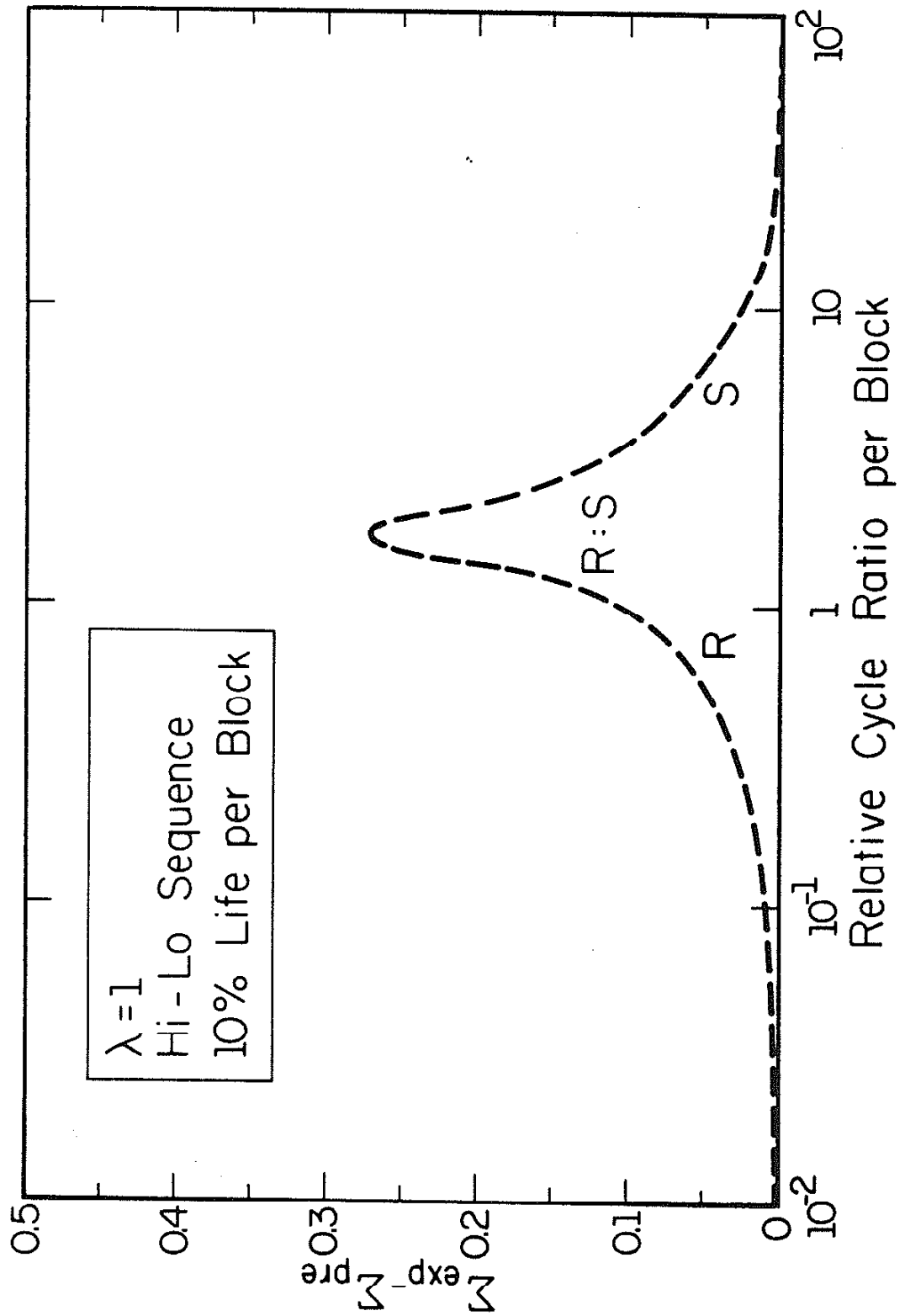

Figure 57 The curve of dual crack systems.

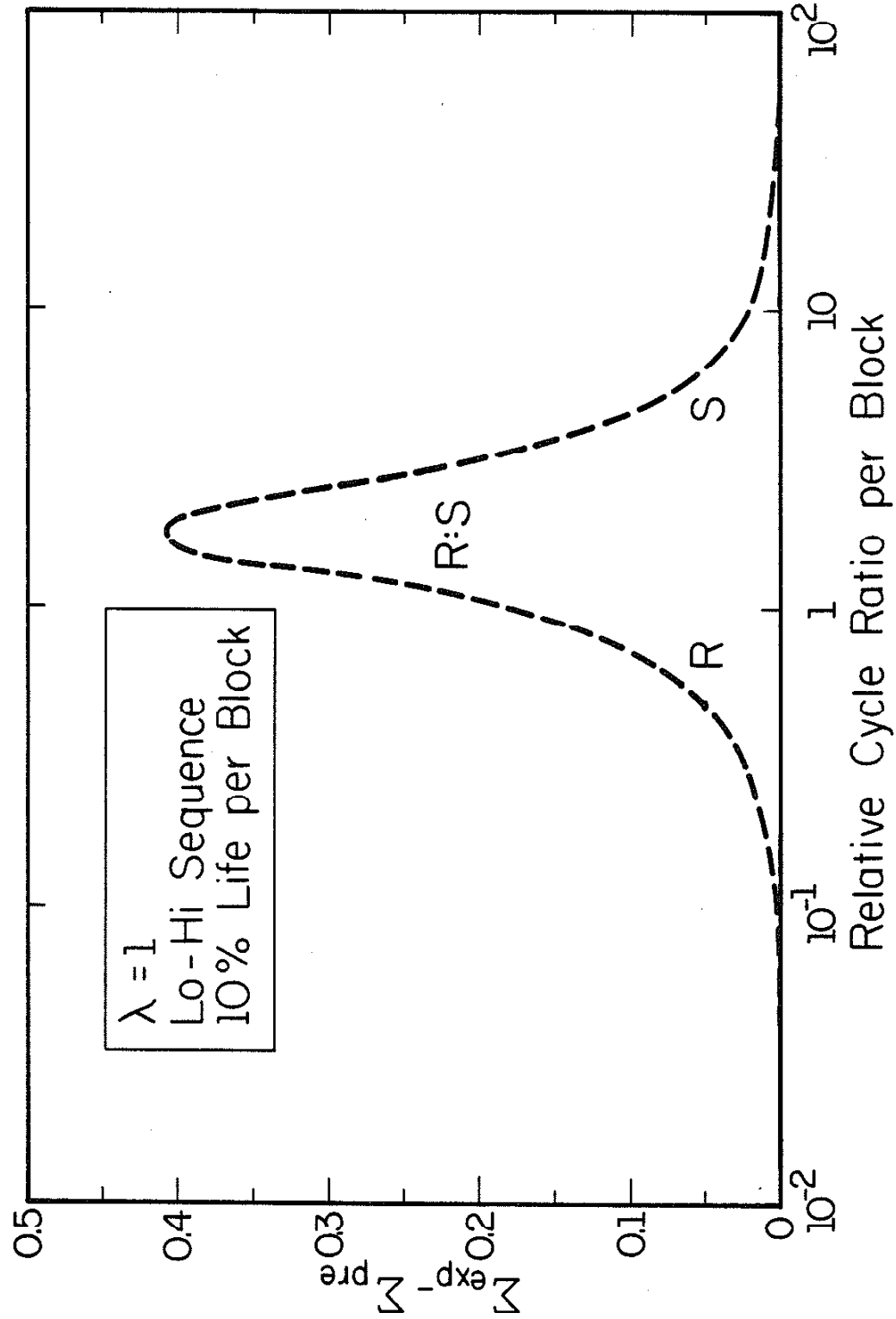

Figure 58 The curve of dual crack systems.

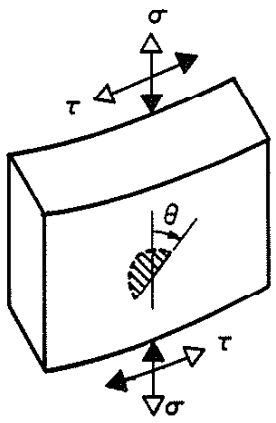

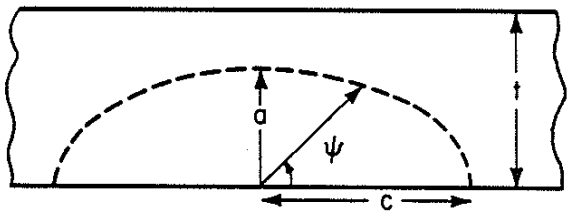

Figure 59 Part-through crack in a finite plate.

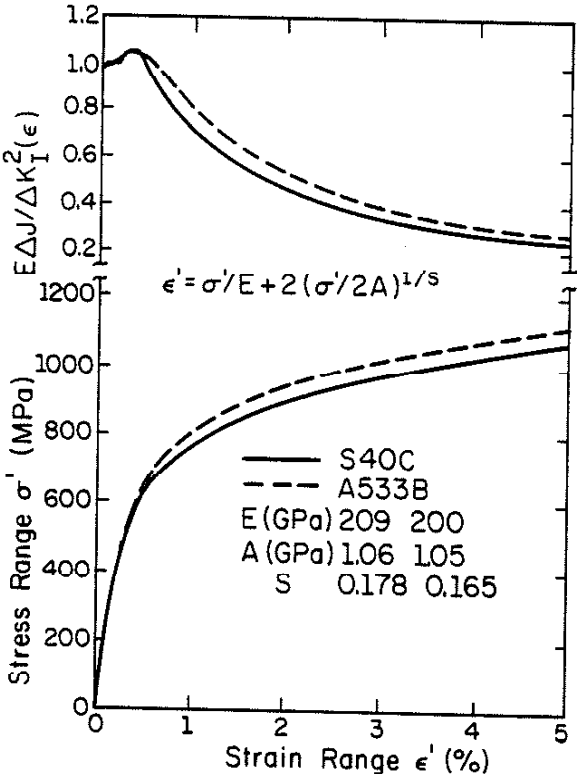

Figure 60 Variation of $E\Delta J/\Delta K_I^2(\varepsilon)$ with total strain range (upper curves) [59].

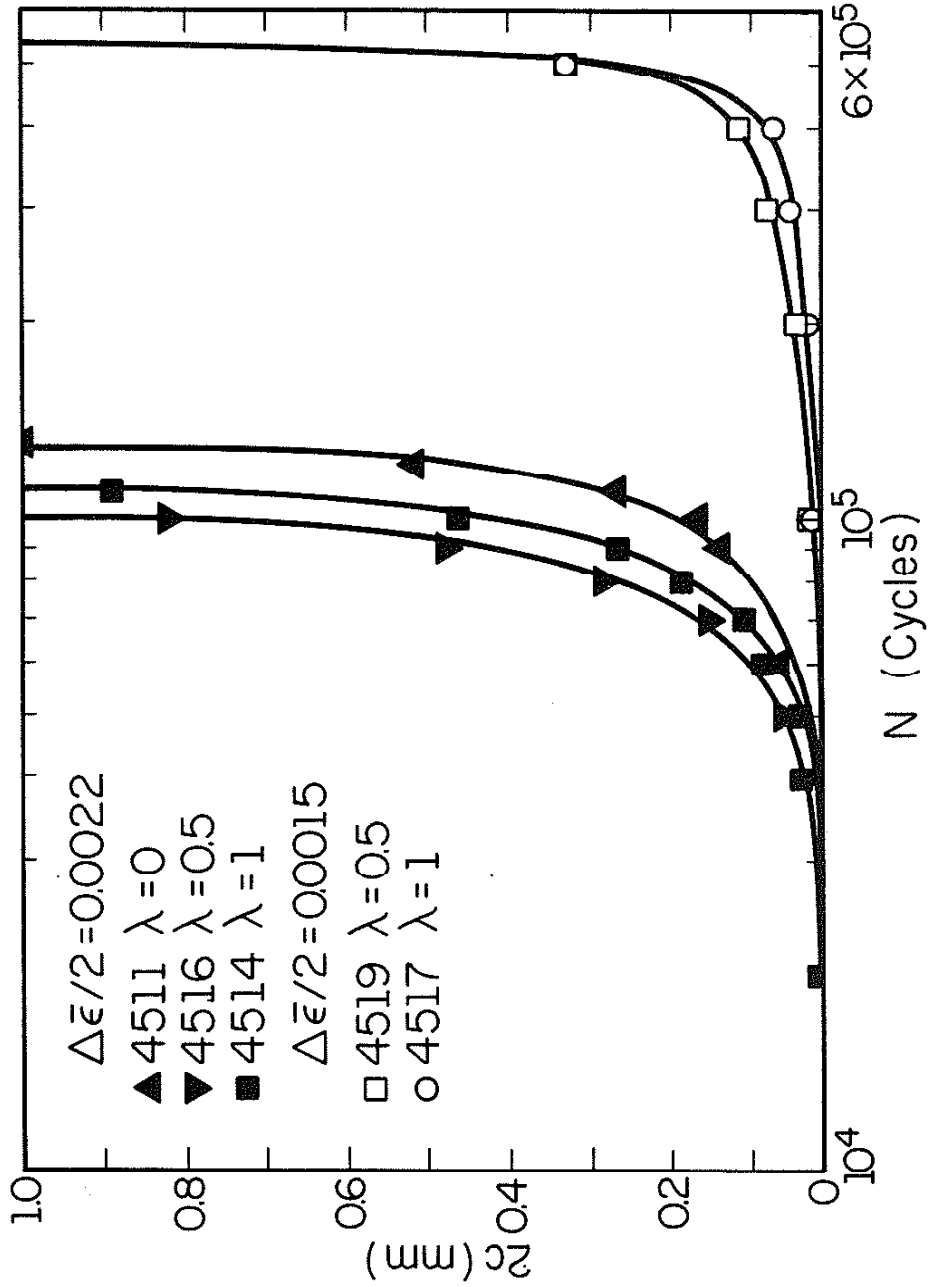

Figure 61 Type-S crack growth curve, λ = 0, 0.5 and 1.

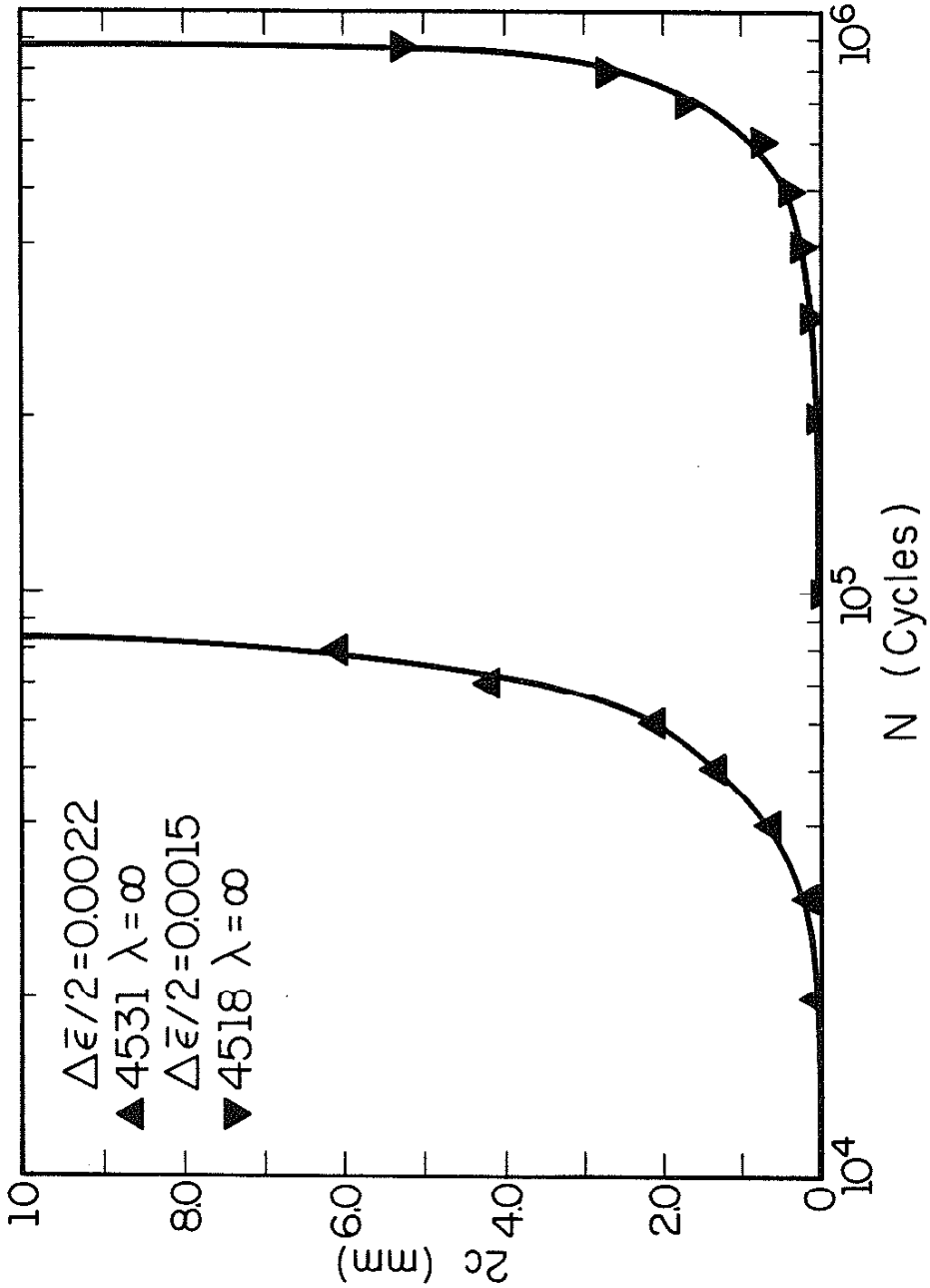

Figure 62 Type-S crack growth curve, λ = ∞.

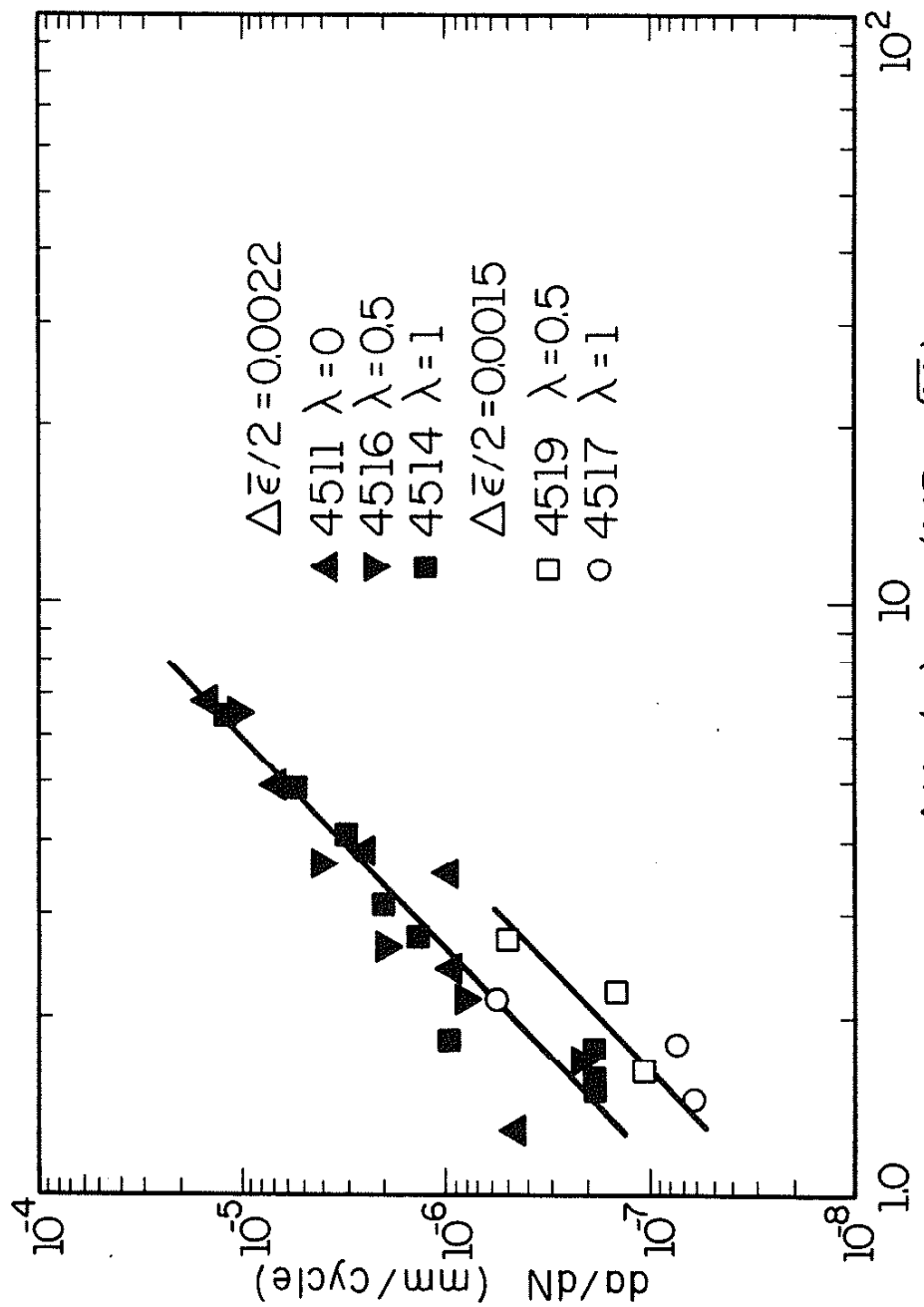

Figure 63 Crack depth growth rate versus equivalent stress intensity factor, $\lambda = 0$, 0.5 and 1.

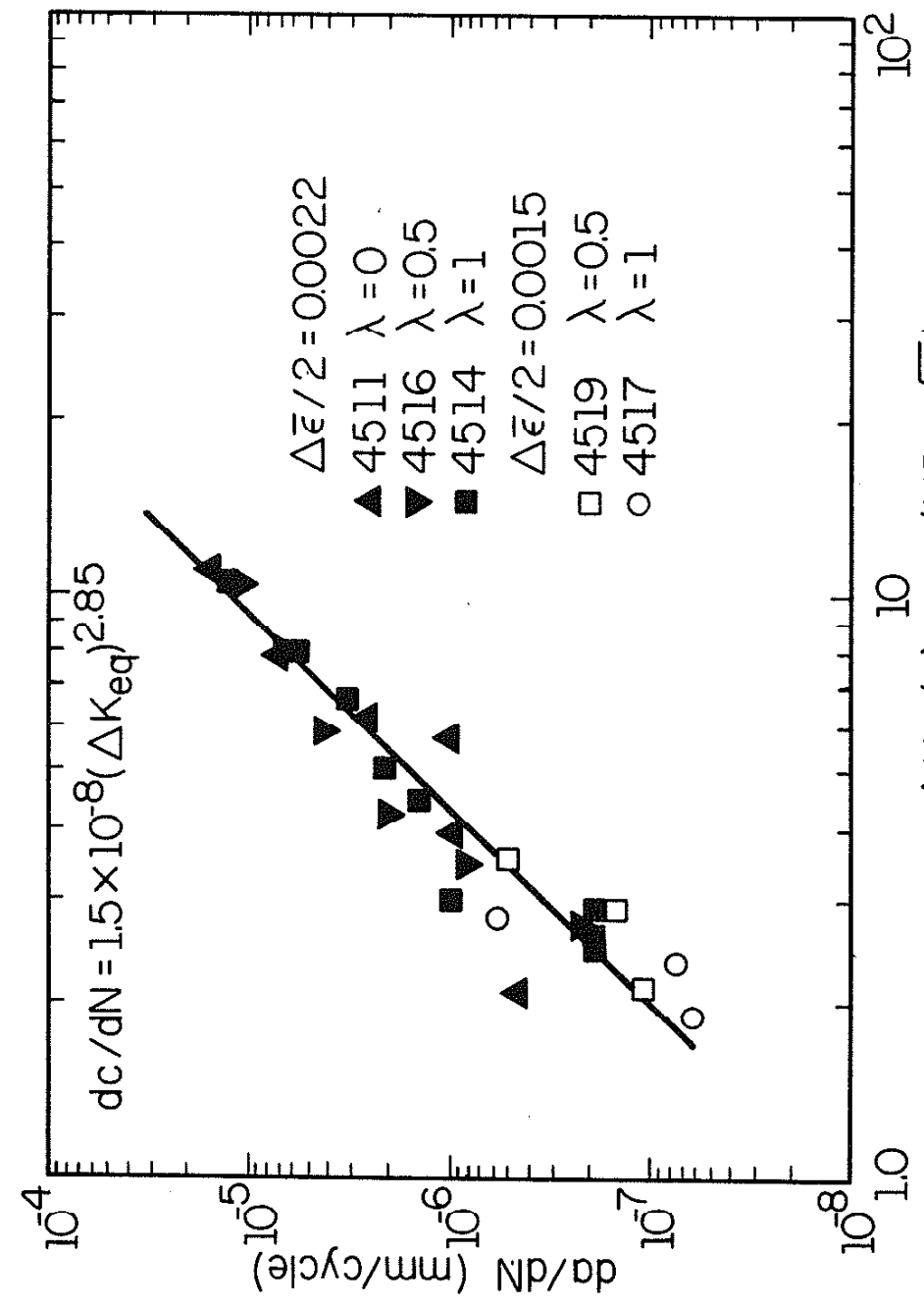

Figure 64 Crack depth growth rate versus equivalent strain intensity factor, λ = 0, 0.5 and 1.

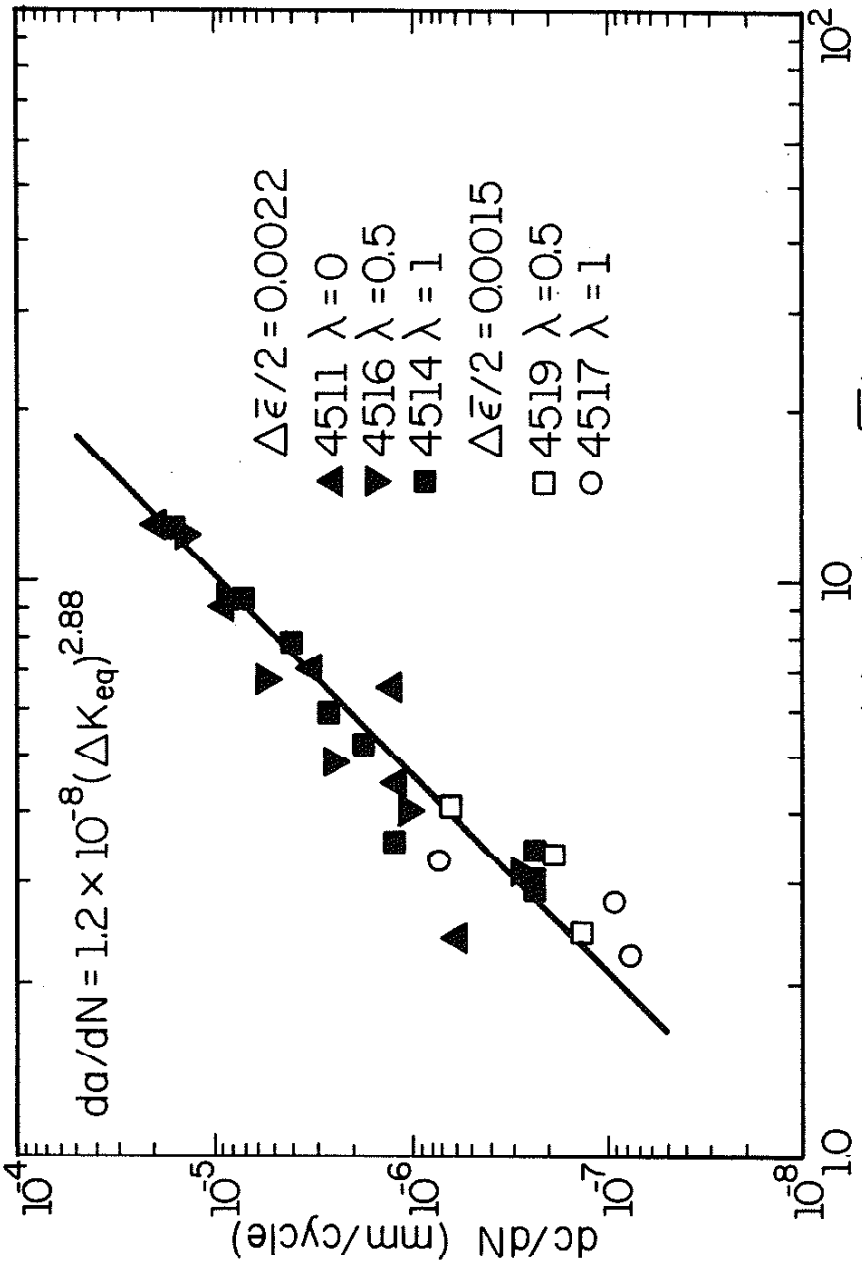

Figure 65 Surface crack growth rate versus equivalent strain intensity factor, λ = 0, 0.5 and 1.

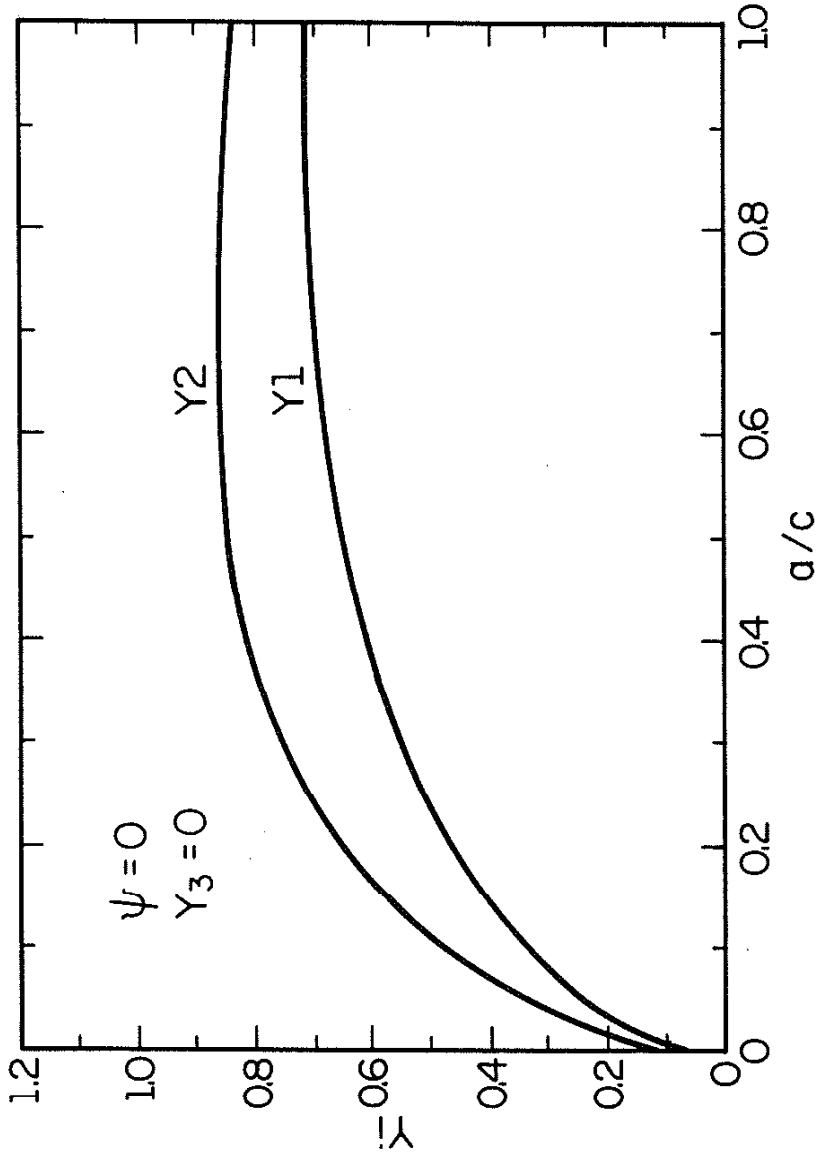

Figure 69 Geometry factor versus aspect ratio, $\psi = 0$.

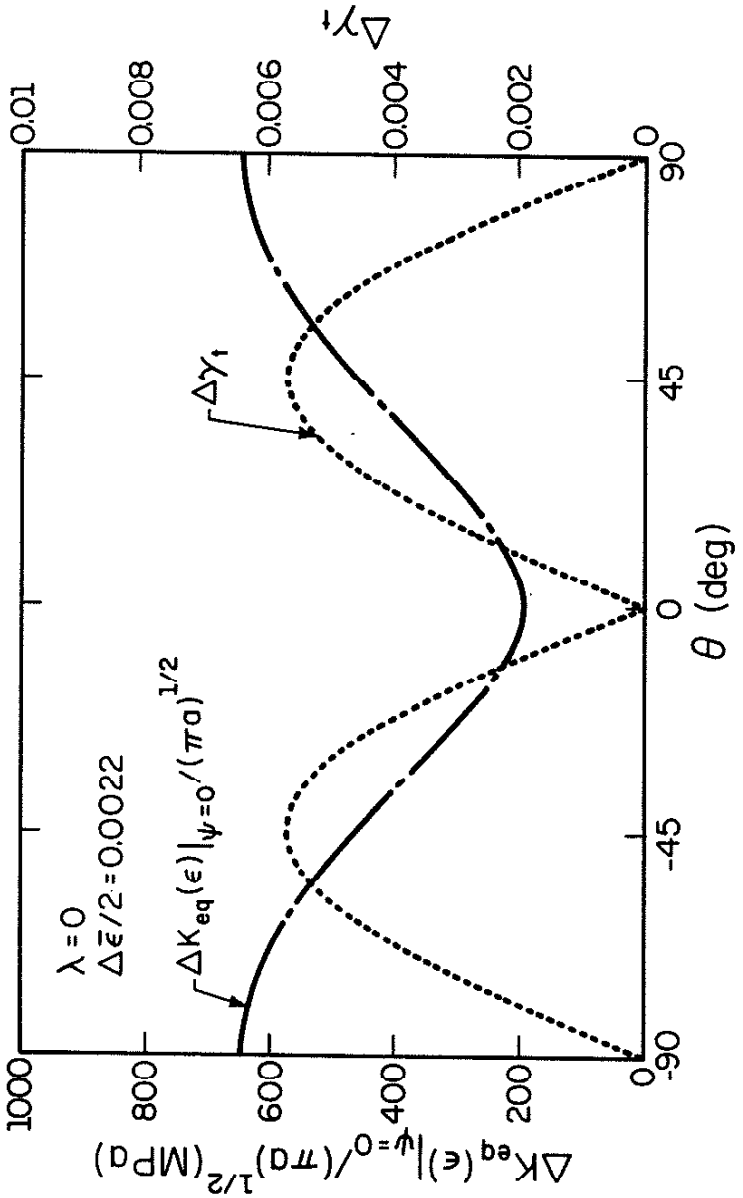

Figure 71 Comparison of normalized $\Delta K_{eq}(\epsilon)|\psi = 0$ and $\Delta\gamma_t$ with respect to crack direction, $\lambda = 0$.

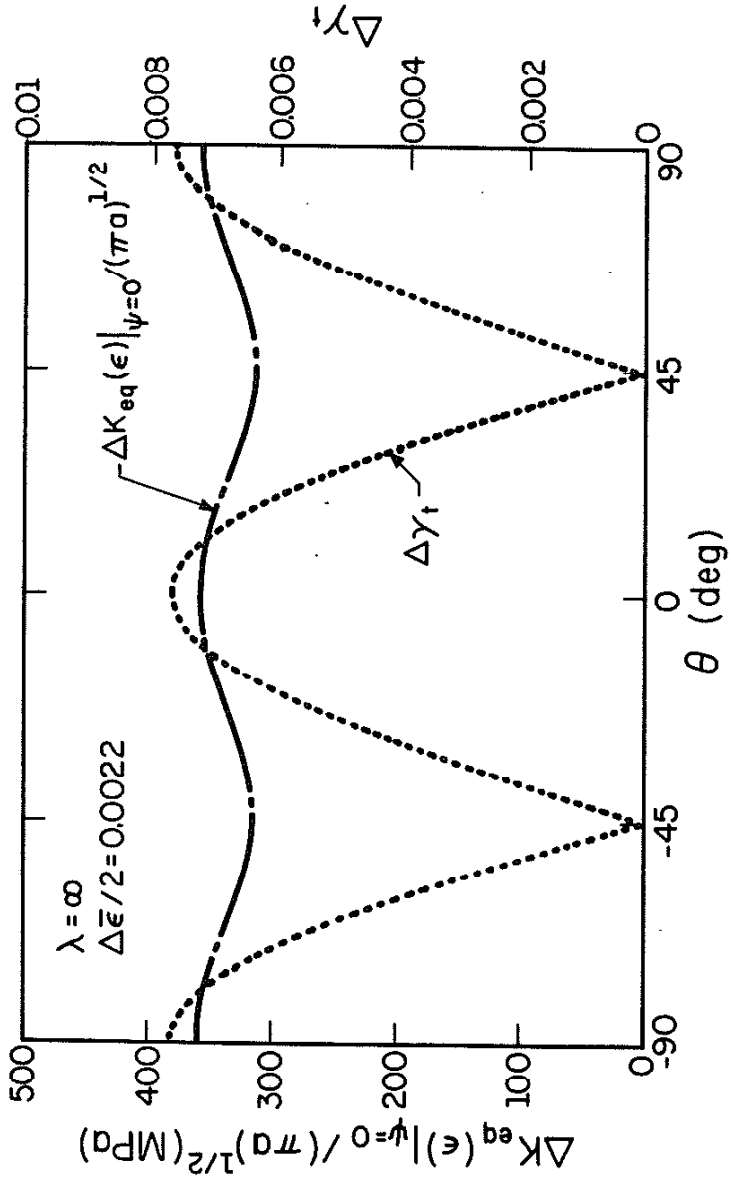

Figure 72 Comparison of normalized $\Delta K_{eq}(\epsilon)|\psi = 0$ and $\Delta\gamma_t$ with respect to crack direction, $\lambda = \infty$.

REFERENCES

1. Kaechele, L. (1963), "Review and Analysis of Cummulative Damage Theories," Rand Corp. Memo RM-3650-PR.

2. Grover, H. J. (1960), "An Observation Concerning the Cycle Ratio in Cummulative Damage," Symp. on Fatigue of Aircraft Structures, ASTM, STP 274, pp. 120-124.

3. Miller, K. J., and K. P. Zachariah (1977), "Cummulative Damage Laws for Fatigue Crack Initiation and Stage I Propagation," J. of Strain Analysis, 12 (4), pp. 262-270.

4. Richart, F. E., and Newmark, N. M. (1948), "An Hypothesis for the Determination of Cummulative Damage in Fatigue," Proc. ASTM, 48, pp 767-800.

5. Marco, S. M., and W. L. Starkey (1954), "A Concept of Fatigue Damage," Trans. American Soc. Mech. Eng., 76 (4), pp. 627-632.

6. Corten, H. T., and T. J. Dolan (1956), "Cummulative Fatigue Damage," Proc. Int. Conf. Fatigue of Metals, Inst. of Mech. Eng., pp. 235-246.

7. Freudenthal, A. M., and R. A. Heller (1956), "On Stress Interaction in Fatigue and a Cummulative Damage Rule," J. Aerospace Sci., 26 (7), pp. 431-442.

8. Wood, W. A. (1959), "Some Basic Studies in Fatigue of Metals," Conf. on Fracture, MIT Press.

9. Wood, W. A. (1962), "Metal Ftigue in Torsion at Large and Intermediate Amplitudes," J. Inst. Metals, 91, pp. 225-229.

10. Porter, J., and L. C. Levy (1960), J. Inst. Metals, 89, p. 86.

11. Benham, P. P., and H. Ford (1961), "Low Endurance Fatigue of a Mild Steel and an Aluminum Alloy," Mech. Eng. Sci., 3, pp. 119-132.

12. Freudenthal, A. M. (1968), "Some Remarks on Cummulative Damage in Fatigue Testing and Fatigue Design," J. Welding in the World, 6, pp 184-194.

13. Paris, P. C., and F. Erdogen (1963), "A Critical Analysis of Crack Propagation Laws," J. Basic Eng. Trans. ASME, 85, p. 528.

14. Elber, W. (1971), "The Significant of Ftigue Crack Closure," ASTM STP 486, p. 240.

15. See ASTM STP 486, 595, 671, 687, 714, 748 and 770.

16. Blatherwick, A. A., and N. D. Viste (1967), "Cummulative Damage Under Biaxial Fatigue Stress," Materials Research and Standards, 7 (8), pp. 331-336.

17. McDiarmid, D. L. (1974), "Cummulative Damage in Fatigue under Multiaxial Stress Conditions," Proc. Inst. Mech. Eng., 188 (40), pp 423-430.

18. Fash, J. W., D. F. Socie, and D. L. McDowell (1982), "Fatigue Life Estimates for a Simple Notched Component Under Biaxial Loading," Int. Symp. on Multiaxial Fatigue, San Francisco, CA.

19. Leese, G. E. (1982), "Low Cycle Torsional Fatigue of 1045 Steel in Shear Strain Control," FCP Report No. 43, University of Illinois.

20. Miner, M. A. (1945), "Cummulative Damage in Fatigue," J. Applied Mech., 12 (1), pp. A159-A164.

21. Rabotnov, Y. N. (1964), Creep Problem in Structural Members, North Holland Pub. Co., Amsterdam, London.

22. Chaboche, J. L. (1977), "A Differential Law of Non-linear Cummulative Fatigue Damage," Paris Institut Technique Du Batiment Et Des Travaus Publies, HS No. 39.

23. Lemaitre, J., and A. Plumtree (1979), "Application of Damage Concepts to Predict Creep-Fatigue Failures," Trans. Am. Soc. Mech. Eng., 101, pp. 284-288.

24. Kachanov, L. M. (1958), Izvest. Akad. Nauk, SSSR, OTN, No. 8, p. 25.

25. Manson, S. S., J. C. Freche, and C. R. Ensign (1967), "Application of a Double Linear Damage Rule to Cummulative Fatigue," ASTM STP 415, pp. 384-412.

26. Manson, S. S., and G. R. Halford (1981), "Practical Implementation of the DLDR and Damage Curve Approach for Treating Cummulative Fatigue Damage," Int. J. Fracture, 17 (2), pp. 169-192.

27. Fong, J. T. (1982), "What is Fatigue Damage?," ASTM STP 775, pp. 243-266.

28. Forsyth, P. J. E. (1961), "A Two-Stage Process of Fatigue Crack Growth," Proc. Crack propagation Symp., Cranfield, 1, pp. 76-94.

29. Socie, D. F., C. T. Hua, T. A. Beer, and L. E. Waill, "Observations of Small Cracks in Biaxial Fatigue," Second Int. Conf. on Fatigue, Birmingham, UK, 1984.

30. Miller, K. J., and M. F. E. Ibrahim (1981), "Damage Accumulation During Initiation and Short Crack Growth Regimes," Fatigue of Eng. Materials and Structures, 4 (3), pp. 263-277.

31. Miller, K. J. (1976), "Multiaxial Fatigue," Int. Conf. on Fatigue Testing and Design, 1, London, pp. 13.1-13.17.

32. ASTM STP 687 (1978), "Part-through Crack Fatigue Life Prediction," J. B. Chang, ed.

33. Schijve, J. (1972), "The Accumulation of Fatigue Damage in Aircraft Materials and Structures," AGARDograph No. 157.

34. Kunio, T., K. Iwamoto, K. Kanazawa (1969), "Behavior of Low Cycle Fatigue at Elevated Temperatures," Fracture, Chapman and Hall, Inc., pp. 655-666.

35. Riemann, W. H., and W. A. Wood (1965), Columbia University, Tech. Report NONR (91), No. 11.

36. Frost, N. E., K. L. Marsh, and L. P. Pook (1974), "Metal Fatigue," Oxford University Press, Section 6.2.

37. Jacoby, G. H., (1968), Proc. of the 3rd Conf. on Dimensioning, Budapest, p. 81.

38. Iida, K., and M. Kawaha (1975), "Changes in Fatigue Crack Shape During Growth," Naut Report 9011, Tokyo University.

39. Sommer, E., L. Hodulak, H. Kordisch (1977), J. of Pressure Vessel Technology, ASME, pp. 106-111.

40. Beer, T. A. (1982), "Crack Shapes During Biaxial Fatigue," Masters Thesis, Dept. of Mech. and Ind. Eng., University of Illinois.

41. Erdogen, F., and G. C. Sih (1963), "On the Crack Extension in Plates under Plane Loading and Transverse Shear," J. Basic Eng., 85, pp. 519-527.

42. Sih, G. C. (1974), "Strain Energy Density Factor Applied to Mixed Mode Crack Problems," Int. J. Fracture, 10, pp. 493-507.

43. Tanaka, K. (1974), "Fatigue Crack Propagation from a Crack Inclined to the Cyclic Tensile Axis," Eng. Frac. Mech., 10, pp. 305-322.

44. Weertman, J. (1966), "Rate of Growth of Fatigue Cracks Calculated from the Theory of Infinitesimal Dislocations Distributed on a Plane," Int. J. Frac. Mech., 2, pp. 460-467.

45. Lardner, R. W. (1968), "A Dislocation Model for Fatigue Crack Growth in Metals," Phil. Mag., 17, pp. 71-82.

46. Miller, K. J. (1977), "Fatigue Under Complex Stress," J. of Metal Sci., pp. 432-438.

47. Pearson, S. (1972), "Initiation of Fatigue Cracks in Commercial Aluminum Alloys and the Subsequent Progapation of Very Short Cracks," RAE Tech. Rep. 72236.

48. Irwin, G. R. (1960), "Fracture Mechanics," Proc. First Symp. Naval Struc. Mech., pp. 557-594, Pergamn Press.

49. McCarver, J. F., and R. O. Ritchie (1982), "Fatigue Crack Propagation Thresholds for Long and Short Cracks in Rene' 95 Nickel-Base Superalloy,: Master Science Eng., 55, pp. 63-67.

50. Morris, W. L., M. R. Jones, and O. Buck (1982), "A Simple Model of Stress Intensity Range Threshold and Crack Closure Stress," Eng. Frac. Mech., 14.

51. Irwin, G. R. (1962), "The Crack Extension Force for a Part-through Crack in a Plate, J. Appl. Mech., Trans. ASME, pp. 651-654.

52. Green, A. E., and I. N. Sneddon (1950), "The Stress Distribution in the Neighborhood of a Flat Elliptical Cracks in an Elastic Solid," Proc. Cambridge Phil. Soc., 46, pp.159-164.

53. Kassir, M. K., G. C. Sih (1966), "Three-Dimensional Stress Distribution Around an Elliptical Crack under Arbitrary Loadings," J. of Appl. Mech., September, pp. 601-611.

54. Dowling, N. E. (1982), "Growth of Short Cracks in an Alloy Steel," Sci. Paper, 82-1D7-STINE-P1, Westinghouse Res. Lab..

55. Dowling, N. E. (1978), "Crack Growth During Low Cyclic Fatigue of Smooth Axial Secimens," ASTM STP 637, pp. 97-121.

56. El Haddad, M. H., N. E. Dowling, T. H. Topper, and K. N. Smith (1980), "J. Integral Applications for Short Fatigue Cracks at Notches," Int. J. Frac., 16, pp. 15-30.

57. El Haddad, M. H., K. N. Smith, and T. H. Topper (1979), "A Strain Based Intensity Factor Solution for Short Fatigue Cracks Initiating from Notches, " ASTM STP 677, pp. 274-289.

58. Kitagawa, H. S., S. Takahashi, C. M. Suh, and S. Miyashita (1979), "Quantitative Analysis of Fatigue Process--Microcracks and Slip Lines Under Cyclic Strains," ASTM STP 675, pp. 420-449.

59. Imai, Y., and T. Matake (1983), "Surface Crack Growth During Push-Pull Fatigue of Smooth Specimens," Jan. Soc. Material Sci., 32, pp. 1157-1161.

60. Irving, P. E. (1983), "Microcracks Growth and Torsional Fatigue,"GKN Report No. 1635, UK.

61. Pearson, S. (1975), "Initiation of Fatigue Cracks in Commercial Aluminum Alloys and the Subsequent Propagation of Very Short Cracks," Eng. Frac. Mech., 7, pp. 235-247.

62. Nelson, D. V., and S. Tipton, Dept. of Mech. Eng., Stanford University, private communication.

63. Palaniswamy, K. (1972), "Crack Propagation Under General In-plane Loading," Ph.D. Thesis, California Institute of Technology.

64. Nuismer, R. J. (1975), "An Energy Release Rate Criterion for Mixed Mode Fracture," Int. J. Fracture, 11, pp. 245-250.

APPENDICES

APPENDIX A TABLES OF CRACK GROWTH DATA

APPENDIX B LISTS OF COMPUTER PROGRAM

* The results of crack density are the average values of three samples.
** All cracks represent failure unless otherwise noted.
*** The notation for cycle number of block loading. For example, 8-2-7: 8 is the number of blocks, 2 is the second level, and 7 is the number of cycles for this level.

Table A.1 Crack Growth Data

Specimen ID: 4511
Loading Parameters: Constant Loading, $\lambda = 0$
Crack System: Type-S
Failure Cycles: 142541

Cycles	Surface Crack Length (mm)
20000	0.0188
40000	0.019
60000	0.066
90000	0.141
100000	0.166
110000	0.27
120000	0.52
130000	1.06
140000	3.2
142541	7.0

Table A.2 Crack Growth Data

Specimen ID: 4516
Loading Parameters: Constant Loading, $\lambda = 0.5$
Crack System: Type-S
Failure Cycles: 115462

Cycles	Surface Crack Length (mm)
10000	0.027
20000	0.032
50000	0.052
60000	0.0765
70000	0.148
80000	0.283
90000	0.475
100000	0.82
110000	2.12
115462	12.0

Table A.3 Crack Growth Data

Specimen ID: 4528
Loading Parameters: Constant Loading, $\lambda = 0.5$
Crack System: Type-S
Failure Cycles: ---

Cycles	Surface Crack Length (mm)
20000	0.032
30000	0.048
40000	0.144
50000	0.20
60000	0.384
70000	0.768
80000	3.136

Table A.4 Crack Growth Data

Specimen ID: 4519
Loading Parameters: Constant Loading, $\lambda = 0.5$
Crack System: Type-S
Failure Cycles: 611780

Cycles	Surface Crack Length (mm)
100000	0.025
200000	0.042
300000	0.078
400000	0.116
500000	0.33
600000	2.6
611780	10.0

Table A.5 Crack Growth Data

Specimen ID: 4514
Loading Parameters: Constant Loading, $\lambda = 1$
Crack System: Type-S
Failure Cycles: 123543

Cycles	Surface Crack Length (mm)
10000	0.0188
20000	0.026
30000	0.0282
40000	0.0353
50000	0.0376
60000	0.0835
70000	0.10
80000	0.186
90000	0.266
100000	0.463
110000	0.89
120000	2.95
123543	14.0

Table A.6 Crack Growth Data

Specimen ID: 4550
Loading Parameters: Constant Loading, $\lambda = 1$
Crack System: Type-S
Failure Cycles: ---

Cycles	Surface Crack Length (mm)
20000	0.032
30000	0.048
40000	0.058
50000	0.080
60000	0.21
70000	0.32
80000	0.45
85000	0.77
87500	1.04
90000	1.24

Table A.7 Crack Growth Data

Specimen ID: 4517
Loading Parameters: Constant Loading, $\lambda = 1$
Crack Specimen: Type-S
Failure Cycles: 595612

Cycles	Surface Crack Length (mm)
100000	0.019
200000	0.0325
300000	0.05
400000	0.07
500000	0.337
595612	8.0

Table A.8 Crack Growth Data

Specimen ID: 4522
Loading Parameter: Constant Loading, $\lambda = 2$
Crack System: Type-S
Failure Cycles: 98778

Cycles	Surface Crack Length (mm)
10000	0.024
20000	0.04
30000	0.047
40000	0.061
50000	0.17[†]
60000	0.255
70000	0.374
80000	0.67
90000	1.4
98778	7.0

[†]Coalesced with other crack

Table A.9 Crack Growth Data

Specimen ID: 4548
Loading Parameters: Constant Loading, $\lambda = 2$
Crack System: Type-S
Failure Cycles: ---

Cycles	Surface Crack Length (mm)
10000	0.028
20000	0.044
30000	0.053
40000	0.06
50000	0.176[†]
60000	0.192
70000	0.224
80000	0.768
85000	1.92
87500	3.65

[†]Coalesced with other crack

Table A.10 Crack Growth Data

Specimen ID: 4531
Loading Parameters: Constant Loading, $\lambda = \infty$
Crack System: Type-S
Failure Cycles: 93052

Cycles	Surface Crack Length (mm)
20000	0.12
30000	0.2
40000	0.68
50000	1.35
60000	2.1
70000	4.2
80000	6.1
90000	11.0
93052	20.0

Table A.11 Crack Growth Data

Specimen ID: 4518
Loading Parameters: Constant Loading, $\lambda = \infty$
Crack System: Type-S
Failure Cycles: 1010210

Cycles	Surface Crack Length (mm)
100000	0.47
200000	0.68
300000	0.8
400000	0.94
500000	1.12
600000	1.42
700000	1.51
800000	1.71
900000	2.12
1000000	5.0
1010210	14.0

Table A.14 Crack Growth Data

Specimen ID: 4549
Loading Parameters: Constant Loading, $\lambda = \infty$
Crack System: Type-R
Failure Cycles: 889

Cycles	Crack Density* (# of cracks per 0.15 mm^2)
200	5
300	15
500	29
600	40
800	82
889	105

Table A.15 Crack Growth Data

Specimen ID: 4542
Loading Parameters: Step Loading, λ = 0, Lo-Hi Sequence
Crack System: Type-S
Failure Cycles: Hi-1122

Cycles	Surface Crack Length (mm)
Lo-4300	0.031
12900	0.05
17200	0.057
25800	0.059
34400	0.07
43000	0.09
Hi-80	0.109
230	0.153
500	0.195
670	0.313
835	0.813
1000	1.08
1122	7.0

Table A.16 Crack Growth Data

Specimen ID: 4539
Loading Parameters: Step Loading, $\lambda = 1$, Lo-Hi Sequence
Crack System: Type-S
Failure Cycles: Hi-885

Cycles	Surface Crack Length (mm)
Lo-5600	0.016
11200	0.023
22400	0.048
33600	0.075
44800	0.123
56000	0.218
Hi-100	0.281
200	0.421
300	0.555
400	0.641
500	0.781
750	1.62
885	10.0

Table A.17 Crack Growth Data

Specimen ID: 4536
Loading Parameters: Step Loading, $\lambda = \infty$, Lo-Hi Sequence
Crack System: Type-S
Failure Cycles: Hi-572

Cycles	Surface Crack Length (mm)
Lo-4200	0.213
12600	0.42
21000	0.52
29400	0.79
33600	0.88
42000	1.15
Hi-100	1.34
220	1.97
340	3.25
460	5.5[†]
572	20.0

[†]Coalesced with other crack

Table A.18 Crack Growth Data

Specimen ID: 4535
Loading Parameters: Step Loading, $\lambda = 0$, Hi-Lo Sequence
Crack System: Type-R
Failure Cycles: Lo-33055

Cycles	Crack Density* (# of cracks per 0.15 mm^2)
Hi-50	4
110	8
220	18
275	23
385	34
440	37
550	45
Lo-1075	50
4300	59
7525	68
11825	78
13975	82
20450	90
33055	102

Table A.19 Crack Growth Data

Specimen ID: 4538
Loading Parameters: Step Loading, $\lambda = 1$, Hi-Lo Sequence
Crack System: Type-R
Failure Cycles: Lo-39690

Cycles	Crack Density* (# of cracks per 0.15 mm^2)
Hi-75	9
210	27
350	57
420	66
500	78
630	87
700	96
Lo-4200	115
7000	118
11200	120
16800	125
25200	131
30800	133
39690	138

Table A.20 Crack Growth Data

Specimen ID: 4544
Loading Parameters: Step Loading, $\lambda = \infty$, Hi-Lo Sequence
Crack System: Type-R
Failure Cycles: Lo-18641

Cycles	Crack Density* (# of cracks per 0.15 mm^2)
Hi-50	4
180	21
270	46
360	54
450	59
Lo-2000	77
4000	81
7000	90
11000	95
18641	97

Table A.21 Crack Growth Data

Specimen ID: 4560
Loading Parameters: Block Loading, $\lambda = 1$, Lo-Hi Sequence
Crack System: Type-S
Failure Cycles: 8-2-7

Cycles	Surface Crack Length (mm)
1-1-10640	0.043
2-1-10640	0.061
3-1-10640	0.070
4-1-10640	0.125
5-1-10640	0.224
6-1-10640	0.384
7-1-10640	0.872
8-1-10640	4.7
8-2-7	6.0

Table A.22 Crack Growth Data

Specimen ID: 4562
Loading Parameters: Block Loading, $\lambda = 1$, Hi-Lo Sequence
Crack System: Type-S
Failure Cycles: 9-2-10640

Cycles	Surface Crack Length (mm)
1-2-10640	0.016
2-2-10640	0.048
3-2-10640	0.064
4-2-10640	0.070
5-2-10640	0.128
6-2-10640	0.208
7-2-10640	0.368
8-2-10640	1.02
9-2-10640	3.84

Table A.23 Crack Growth Data

Specimen ID: 4564
Loading Parameters: Block Loading, $\lambda = 1$, Hi-Lo Sequence
Crack System: Type-R
Failure Cycles: 7-2-5600

Cycles	Crack Density* (# of cracks per 0.15 mm^2)
1-2-5600	22
2-2-5600	36
3-2-5600	48
4-2-5600	70
5-2-5600	92
6-2-5600	120
7-2-5600	134

Table A.24 Crack Growth Data

Specimen ID: 4561
Loading Parameters: Block Loading, $\lambda = 1$, Lo-Hi Sequence
Crack System: Type-R
Failure Cycles: 11-1-3360

Cycles	Crack Density* (# of cracks per 0.15 mm^2)
1-2-70	3
2-2-70	19
3-2-70	24
4-2-70	38
5-2-70	43
6-2-70	47
7-2-70	50
8-2-70	56
9-2-70	71
10-2-70	76

Table A.25 Crack Growth Data

Specimen ID: 4561
Loading Parameters: Block Loading, $\lambda = 1$, Lo-Hi Sequence
Crack System: Type-S (not failure crack)
Failure Cycles: 11-1-3360

Cycles	Surface Crack Length (mm)
1-2-70	0.033
2-2-70	0.082
3-2-70	0.098
4-2-70	0.116
5-2-70	0.139
6-2-70	0.147
7-2-70	0.188
8-2-70	0.306
9-2-70	0.47
10-2-70	0.66

Table A.26 Crack Growth Data

Specimen ID: 4561
Loading Parameters: Block Loading, $\lambda = 1$, Lo-Hi Sequence
Crack System: Type-S (not failure crack)
Failure Cycles: 11-1-3360

Cycles	Surface Crack Length (mm)
2-2-70	0.020
3-1-5600	0.041
3-2-70	0.061
4-2-70	0.069
5-2-70	0.082
7-2-70	0.137
8-2-70	0.233
9-2-70	0.36
10-2-70	0.53

Table A.27 Crack Growth Data

Specimen ID: 4567
Loading Parameters: Block Loading, $\lambda = 1$, Hi-Lo Sequence
Crack System: Type-R
Failure Cycles: 10-2-968

Cycles	Crack Density* (# of cracks per 0.15 mm^2)
1-2-7280	4
2-2-7280	15
3-2-7280	19
4-2-7280	25
5-2-7280	39
6-2-7280	56
7-2-7280	58
8-2-7280	64
9-2-7280	72
10-2-968	85

Table A.28 Crack Growth Data

Specimen ID: 4567
Loading Parameters: Block Loading, λ = 1, Hi-Lo Sequence
Crack System: Type-S (not failure crack)
Failure Cycles: 10-2-968

Cycles	Surface Crack Length (mm)
2-2-7280	0.032
3-1-49	0.056
4-2-7280	0.074
5-1-49	0.109
5-2-7280	0.125
6-1-48	0.135
6-2-7280	0.16
7-2-7280	0.288
8-1-49	0.336
8-2-7280	0.48
9-1-49	0.61
9-2-7280	0.25
10-2-968	1.5

B.1 The Calculation of Weighted Crack Density

```
10 DIM N(50),R(50),S(50),S1(50)
20 N(0)=0 R(0)=0
30 PRINT "SPEC.I.D.&SAMPLE I.D.(####-##)"|INPUT I$
100 PRINT "PAIRS OF DATA POINTS"|INPUT J
200 FOR I=1 TO J
300 PRINT "CYCLES;N("I") AND NO.OF CRACKS;R("I")"|INPUT N(I),R(I)
500 NEXT I
600 FOR I=1 TO J
650 S1(I)=0
700 FOR K=0 TO I-1
800 S(K)=(N(I)-N(K))/N(J)*(R(K+1)-R(K))
900 S1(I)=S1(I)+S(K)
1000 NEXT K
1100 NEXT I
1120 PRINT I$
1200 FOR I=1 TO J
1250 PRINT
1300 S1(I)=S1(I)/S1(J)
1400 N(I)=N(I)/N(J)
1500 PRINT I,N(I),S1(I)
1550 NEXT I
1700 STOP
```

B.2 The Simulation of Block Loading

```
100 X=0 F=0 B=0
200 PRINT "CONSTANT FOR HI DAMAGE CURVE"|INPUT E1
300 PRINT "CONSTANTS FOR LO DAMAGE CURVE(A,B,C)"|INPUT A1,B1,C1
350 PRINT "CYCLE RATION FOR LO INITIATION PHASE"|INPUT X9
400 PRINT "DAMAGE DUE TO INITIATION PHASE"|INPUT D9
500 PRINT "INCREMENTAL CYCLE RATIO FOR HI SUBBLOCK"|INPUT X1
600 PRINT "INCREMENTAL CYCLE RATIO FOR LO SUBBLOCK"|INPUTX2
700 PRINT "FAILURE CYCLES FOR HI LOADING"|INPUT N1
800 PRINT "FAILURE CYCLES FOR LO LOADING"|INPUT N2
900 PRINT "WHICH LEVEL APPLIED FIRST(HI...1;LO...2)"|INPUT N
920 PRINT "N=1...HI LOADING;N=2...LO LOADING"
930 PRINT "INCR.CYCLE RATIO FOR HI=",X1
940 PRINT "INCR.CYCLE RATIO FOR LO=",X2
950 PRINT "N","BLOCK #","RATIO ACC.","DAMAGE ACC."
1000 ON N GO TO 1800,1100
1100 GOSUB 20000|IF F=1 THEN STOP
1200 IF X>X9 THEN GO TO 1400
1300 D=A1*X↑B1|GO TO 1500
1400 D=X↑C1
1500 GOSUB 10000
1600 N=1
1700 X=D↑(1/E1)
1800 GOSUB 20000/|IF F=1 THEN STOP
1900 D=X↑E1
2000 GOSUB 10000
2100 N=2
2200 IF D>D9 THEN 2400
2300 X=(D/A1)↑(1/B1)|GO TO 2500
2400 X=D↑(1/C1)
2500 GOSUB 20000|IF F=1 THEN STOP
2600 GO TO 1200
10000 B=B+.5
10200 PRINT N,B,X,D
10300 RETURN
20000 ON N GO TO 20100,20200
20100 R=X1|X=X+R|GO TO 20300
20200 R=X2|X=X+R
20300 IF X<1 THEN GO TO 21000
20400 X5=1-X+R
20500 ON N GO TO 20600,20700
20600 N8=N1*X5|GO TO 20000
20700 NB=N2*X5
20800 PRINT "N","CYCLE REM.","RATIO REM.","DAMAGE REM."
20900 PRINT N,N8,X5,1-D|F=1
21000 RETURN
```